Development and Analysis of a Solar-Based Integrated System with a CO_2 Rankine Power Cycle

By

Abdullah AlZahrani

A Thesis Submitted in Partial Fulfillment

Of the Requirements for the Degree of

Master of Applied Science in Mechanical Engineering

Faculty of Engineering and Applied Science

University of Ontario Institute of Technology

October 2013

Abstract

The current work is a thermodynamic-based design and analysis of a solar-based integrated system for power production. In this regards, a reheat supercritical carbon dioxide (S-CO_2) Rankine cycle is proposed. This cycle is then integrated with a parabolic trough collector (PTC) solar field, a thermal energy storage system and an absorption refrigeration system (ARS).

A parametric study is then conducted, involving energy and exergy analyses of each subsystem and the overall integrated system. The system performance under different operating conditions is evaluated through energy and exergy efficiencies as well as energy and exergy based coefficients of performance (COP) for the absorption system. The heat energy losses and exergy destruction rates are also evaluated for different components.

The effects of changing some radiation properties and operating conditions on the performance of the PTC solar field are investigated. This includes beam radiation incidence angle, receiver emittance and glass cover emittance. In addition, the impacts of changing these parameters on the overall integrated system energy and exergy efficiencies are illustrated. The energy and exergy efficiencies of the PTC are found to be 66.35% and 38.51%.

The energy and exergy efficiencies of the reheat S-CO_2 Rankine power cycle are examined under various operating conditions of the concentrated solar power (CSP) plants. The exergy destruction rates through the cycle components are determined and evaluated.

The results show that the S-CO_2 Rankine power cycle is expected to achieve energy and exergy efficiencies of 31.6%, and 57.5%, respectively. Under the same operating conditions, the energetic COP for ARS is about 0.7 and the exergetic COP_{ex} is 0.27. Accordingly, the overall integrated system energy (heat-to-electric) and exergy efficiencies become 11.73%, and 12.36%, respectively.

Aknowledgments

First and foremost, I would like to express my deepest gratitude to “Allah” for His blessing on me in making me complete this thesis successfully.

I would like to register my thanks and appreciation to my supervisor Prof. Ibrahim Dincer for his overwhelming support and guidance that shall never be forgotten. His invaluable help of constructive comments and suggestions throughout my research journey have contributed to the successful completion of this thesis.

Special thanks to my supervisory committee for their effort and advice. It is also a great opportunity to thank other professors and researches whom I met at UOIT.

I would like to thank all Dr. Dincer group especially Tahir Ratlamwala, Calin Zamfirescu and Hasan Ozcan for their support and help. Then, my sincere thanks to a number of success partners, whom without, I would not have been able to do it.

I would like to extend my thanks to Umm Al-Qura University for their generous financial support over the last three years, which have made my academic dream true. Also, I sincerely thank Umm Al-Qura University administration and all my colleagues there as I am looking forward to joining your academic community.

Last but not least, I am extremely thankful and grateful to my beloved family for their unconditional support.

Table of Contents

List of Figures

List of Tables

Nomenclature

A	Area (m^2)
C	Cooling; Concentration
C_p	Specific heat (kJ/kg-K)
D	Diameter (m)
E	East
ex	Specific exergy (kJ/kg)
$\dot{E}x$	Exergy rate (kW)
F	Removal factor; Collector efficiency factor
h	Specific enthalpy (kJ/kg) ; Convective heat transfer(W/m^2-K)
I	Radiation flux (W/m^2)
k	Thermal conductivity (W/m-K)
K	Incident angle modifier
L	Length
m	Mass (kg)
$\dot{m}$	Mass flow rate (kg/s)
N	Number of the day; North
Nu	Nusselt number (-)
P	Pressure
Pr	Prandtl number (-)
Q	Heat energy (kJ)
$\dot{Q}$	Heat rate (kW)
Re	Reynolds Number(-)
S	South
s	Specific entropy (kJ/kg)
T	Temperature (°C)

U	Overall heat transfer coefficient (W/m-K)
V	Volumetric flow rate (m^3/s)
W	Power (kW); West
$\dot{W}$	Work rate, W

Greek Letters

α	Solar altitude(°); Absorptivity
β	Slop angle (°)
γ	Surface azimuth (°); Intercept factor
δ	Declination (°)
ε	Emittance (-); Heat exchanger effectiveness
η	Efficiency
θ	Incidence angle (°); zenith angle (°)
μ	Viscosity (kg/m-s)
σ	Stefan-Boltzmann constant($W/m^2\text{-}K^4$); Density (kg/m^3)
φ	Latitude (°)
ω	Hour angle (°)

Subscripts

a	Ambient
abs	Absorber; Absorbed
av	Average
b	Beam (direct)
c	Cover; Cold stream; convection
ch	Charging
CON	Condenser
CP	Circulating pump
d	Diffuse

D	Destroyed
des	Desorber
dis	Discharging
en	Energy
eva	Evaporator
ex	Exergy
f	Factor; Final;
g	Global
h	Hot stream
HE	Heater
htf	Heat transfer fluid
i	Internal; Inlet
k	State point
L	Loss
o	Outer; Exit; Optical; Output
on	Extraterrestrial
ov	Overall
p	Constant pressure; Aperture; Pump
r	Receiver; Radiation
R	Removal
RE	Reheater
rec	Rectifier
s	Solar
sc	Solar constant
SP	Solution pump
st	Storage
t	Total

th	Thermal
u	Useful; Gain
w	Wind
z	Zenith

Acronyms

AM	Air mass
ARS	Absorption refrigeration system
CO_2	Carbon dioxide
COP	Coefficient of performance
CSP	Concentrating solar power plant
DNI	Direct normal irradiance (insolation)
EES	Engineering equation solver
EJ	Exajoule
EV	Expansion valve
GHG	Greenhouse gasses
HCE	Heat collector element
HEX	Heat exchanger
HFC	Heliostat field collectors
HPT	High pressure turbine
HTF	Heat transfer fluid
IHE	Internal heat exchanger
IEA	International energy agency
LFR	Linear Fresnel reflector
LPT	Low pressure turbine
NREL	National renewable energy laboratory
PTC	Parabolic trough technology
PV	Photovoltaic

RE	Renewable energy
SAM	System model advisor
SCA	Solar collector assembly
S-CO_2	Supercritical carbon dioxide
SEGS	Solar electric generation system
SM	Solar multiple
TES	Thermal energy storage
TMY	Typical metrological year

Chapter 1: Introduction

1. 1 Renewable Energy

Since the prehistoric era, the sun has been an abundant source of energy, organization and inspiration. The sun is the largest star at the center of our solar system. Its energy is behind numerous forms of energy and phenomena that occur on earth such as wind and tides. The concepts of time, such as days, months and years, are all defined based on the sun's motion with respect to earth. The moments of sunset and sunrise encourage thoughts of leaving the past behind and moving with optimism towards the future.

The energy content of sunlight hitting the earth's surface for two hours is sufficient for the entire world's energy demand for more than a year. However, the barrier between harnessing this abundant source and the growing energy demand is the absence of mature technologies that can harvest solar energy efficiently and supply power as economically as conventional systems. The current share of solar energy in energy demand is only a tiny fraction as shown in Fig. 1.1.

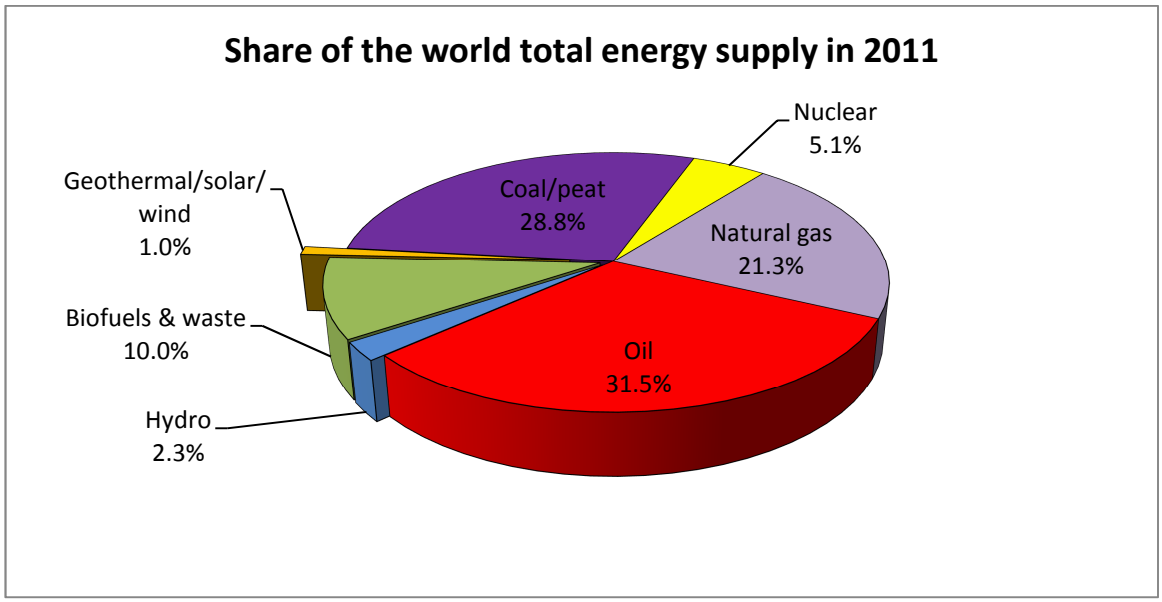

Figure 1.1: Share of total energy supply in 2011. (Data source, IEA 2011).

During the last century, the industrial revolution and economic growth evolved, in parallel with population growth, while depending on fossil fuels as the main energy

source for the different services. Nowadays, oil, coal and gas provide more than 80% of the world's primary energy supply. By contrast, renewable energies such as hydropower, bioenergy, ocean, and wind energy together comprise about 13% (Philibert, 2011). Renewable energies have a considerable potential to replace fossil fuel burning energy systems and subsequently offset CO_2 emissions and mitigate climate change.

Renewable energy (RE) is the energy coming from natural processes such as solar, geophysical or biological sources that are continuously replenished. Solar energy, hydropower, wind, geothermal, and ocean energy are considered as forms of renewable energy. In addition, RE includes renewable fuels such as biomass. RE sources are inexhaustible and have no impact on the environment if properly utilized. The pathways each of these energies take, from a primary energy supply to an end-user as well as its share (EJ)[1] in global RE, are presented in Fig. 1.2. This figure shows that bioenergy provides the largest share with about 10.3% of total global energy supply. That means, if bioenergy is excluded, all other types of RE contribute with only about 3%. In contrast, there is as increasing number of countries and cities that are developing policies and legislations to limit their fossil fuel dependence. Furthermore, some have already scheduled plans to switch from fossil fuels to RE based systems to reduce GHG emissions. This implies a considerable amount of work needs to be conducted for studying each of these abundant energies and exploring its potential.

The current study focuses on solar energy systems. Mankind's knowledge in harnessing solar energy has been evolving over history. For example, in the third century B.C., Greeks were able to make fire using mirrors. In the 4th century B.C., the Romans employed large windows facing south in their houses to allow more access for sunlight and since then, interest in developing efficient ways of using sunlight has been steadily growing. However, during the last two centuries, solar energy experienced major advances, including the photovoltaic effect discovery in 1839, the building of the first solar-powered steam engine in the 1860s, the construction of the first solar cell from selenium wafers in 1889, and the discovery of the photoelectric effect by the end of 1916.

[1] EJ is an abbreviation of exajoule, energy unit which equal 278 billion kilowatt hours.

Currently, there are three major directions of utilizing the sun's energy which include: 1) solar heat capturing, 2) electricity generation using photovoltaic (PV) cells, and 3) solar fuel production, such as hydrogen production using sunlight. The solar energy conversion processes from sunlight to a more useful from of energy are illustrated in Fig. 3. Solar energy heat can be directly utilized in heating applications such as space heating, and domestic and industrial water heating. Alternatively, it can be concentrated in order to heat fluids to a high temperature; these fluids are then, used in a heat engine to generate electricity. On the other hand, PV cells use plates of semiconductor materials, such as Silicon (Si), Cadmium sulfide (CdS), and Gallium arsenide (GaAs), to directly convert solar radiation to electricity. PV cells are stationary devices without any moving parts, thus, need limited maintenance and have an extended life. Currently, available PV cells have conversion efficiency in the range of 6% to 15%, however, the main challenge for this technology markets is the high manufacturing cost (Kalogirou, 2009).

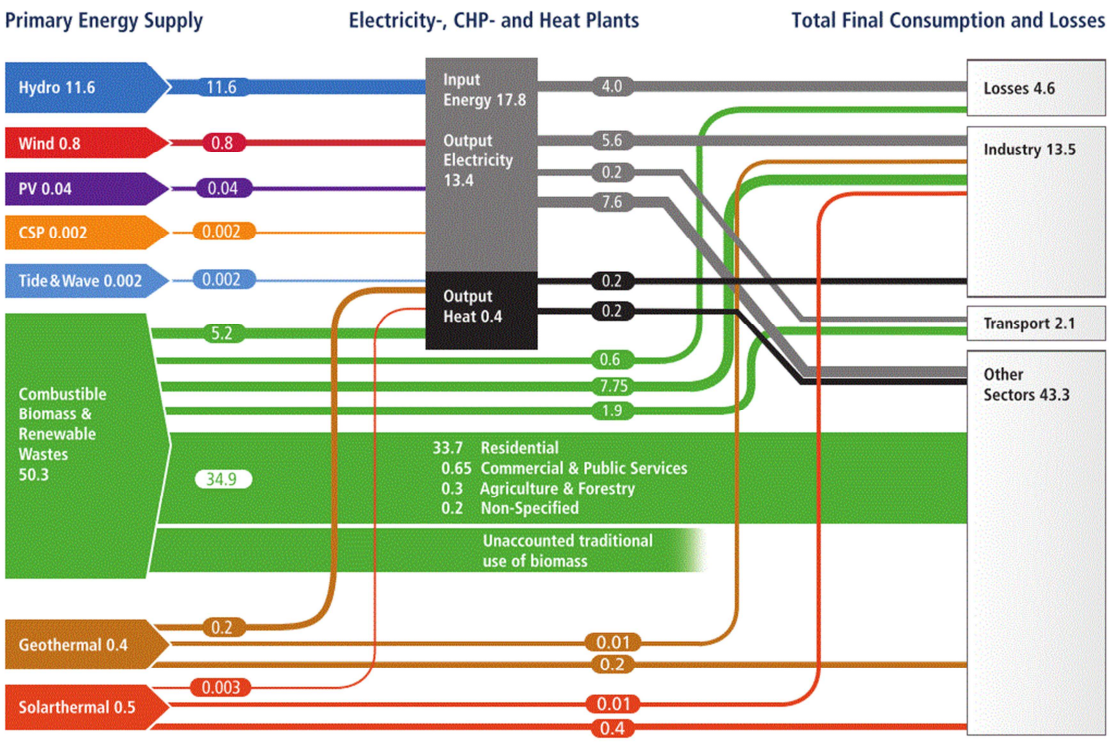

Figure 1.2: Pathways of renewable energies from primary source to end-user (adapted from Iii, 2012).

Solar fuel production, such as hydrogen, is another growing field of solar energy applications, in which solar source of energy is used, in assisting processes, to split water

into its main constituents hydrogen and oxygen. As presented in Fig. 3, there are several methods to produce hydrogen from solar energy. For example, in an electrolysis process the electricity, generated by either concentrated power plants or PV cells, can be used to drive a chemical reaction to dissociate water to hydrogen and oxygen. This process is capable of producing hydrogen with high purity. Alternatively, other processes, such as photo-chemical process, can use the direct sunlight. More details can be found in (Dincer, 2012).

In contrast to photovoltaic systems, concentrating solar power (CSP) plants do not convert sunlight directly to electricity. Instead, it utilizes reflecting mirrors to concentrate beam solar radiation to heat a fluid. This fluid carries heat energy to a heat engine, such as steam Rankine cycle, where the heat can be converted to a mechanical energy and then, electricity. CSP plants use tucking systems to track sun motion and keep solar beam focused targeting a receiver, though which fluid is being circulating to transport heat. These technologies mature and are capable of reach high temperatures, form 350 ^{o}C to 1000 ^{o}C, depending on the solar collector technology been employed. Accordingly, three types of collector technologies commonly used with for CSP plants. These are as per following: 1) parabolic trough collectors, 2) Fresnel reflectors and 3) solar towers or central receivers.

Steam Rankine power cycle has been the dominant technology used for converting heat, generated mainly be fossil fuel combustion, to electricity. It is also used with other heat energy sources such as nuclear, biomass, and concentrating solar systems. Steam power cycles have received considerable amount of research and development over the past years, leaving it in a mature and reliable status. However, there are still some challenges associated with using water as working fluid in this cycle. For example, steam needs to be superheated to prevent condensation during expansion, steam turbine blades are in risk of erosion, high pressure boiler, and high-tech expensive turbines Bao et al. (2013). Moreover, the energy shortage encourages exploring different working fluids that may suite various applications such as low-grad heat and heat recovery systems. Therefore, numerous recent cycles have been increasingly investigated such as organic Rankine cycles which use organic fluid as working fluid. However, there are

limited studies examined the use carbon dioxide CO_2 as a working fluid for Rankine cycles despite the fact that CO_2 has a suitable thermal and chemical properties. As result, supercritical carbon dioxide Rankine cycle is a focus of this work as well as the integration of this novel cycle with solar based energy systems.

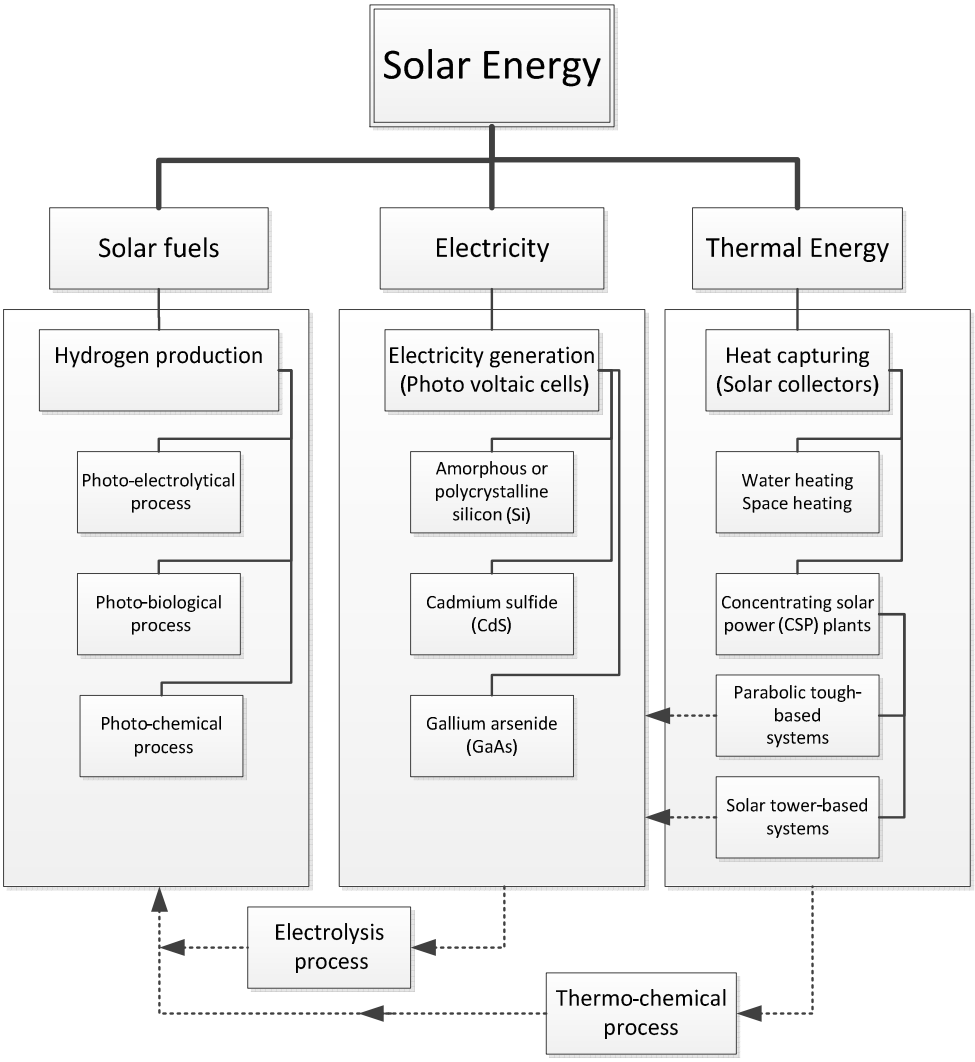

Figure 1.3: Solar energy conversion processes and technologies.

One of the major challenges against the wide spread of CSP plants, which largely depend on wet cooling systems, is the vast amounts of water these plants need where its best potential commonly lies in locations with limited water resources. According to (FLAGSOL, 2013) about 95% of water demand in CSP plants is for cooling purposes while only about 5% is used for mirror cleaning and other purposes. Therefore, a new

cooling system with lower water consumption is very desirable and will significantly boost the CSP technology. This challenge is considered in the current work and the development of water independent cooling system was among other essential goals of this research which will be detailed in the following section.

1. 2 Thesis Motivation and Objectives

The main motivation for this thesis study in the area of solar energy related field is to participate in tackling the global energy challenge that is facing the world today. It is believed that developing such RE based system can contribute to energy security, environmental safety and economic growth. These contributions can be summarized in the following points:

- Developing renewable energy RE based systems increases energy supply diversity.
- Greenhouse gas and CO_2 emissions can be reduced by increasing RE share, such as solar energy, in satisfying global energy demands.
- Increasing the efficiency of RE systems will help offset costs, hence the competitiveness of RE systems compare to conventional systems increases.
- Enhancing economic stability through the provision of local and affordable energy.

Various environmental organizations have found a close link between climate change and the amount of emissions produced by conventional energy systems. Climate change is a global-wide issue leading to serious consequences, such as increases in the earth's average temperature, rising global sea levels, and melting snow and ice. In addition, these changes in weather patterns last for generations to come and have a significant impact on humans, animals and plants. Numerous environmental scientists affirm that human activity is responsible for most of the carbon dioxide CO_2 that has been accumulating in the atmosphere. This carbon is being released from fossil fuel based energy systems that are categorized as a primary source for today's consumers.

On the other hand, the increasing global demand for energy, promoted by population and economic growth, causes another challenge. Although fossil fuel burning is the major reason for climate change, it is a finite source of energy and subsequently, fossil fuel reserves are depleting. Therefore, different alternative resources must be introduced.

Realizing the significance of these challenges has been a driving force for the author and other scientists in undertaking such research that could be a part of an energy solution for a brighter future. Through a scientific methodology, this study proposes and analyzes new solar based power cycles that use supercritical carbon dioxide (S-CO_2) as a working fluid. Such power cycles have a great potential to improve the system's thermal-to-electric conversion efficiency compare to conventional cycles that have been in use since the 1880s. Successful efficiency improvement will have a significant impact on solar-based electric power cost and hence the portion of solar energy.

The specific objectives of this thesis study are listed as follows:

- To develop a novel power cycle that uses S-CO_2 as a working fluid and efficiently converts thermal energy to electric power.
- To develop an integrated cooling system for the cycle (Absorption Refrigeration System-ARS) capable of achieving the targeted cooling/refrigeration duties.
- To implement the designed integrated system as a power block in a CSP plant with a thermal energy storage system TES.
- To conduct a parametric energy and exergy study for the cycle to investigate the effect of the different operating parameters on the cycle's energy and exergy performance.
- To evaluate energy and exergy performance for the parabolic trough collectors (PTC), TES, ARS and the overall integrated system.
- To design the system heat exchangers network for minimum energy losses and maximum heat recovery.

- To evaluate the energy and exergy efficiencies of the system and the exergy destruction rates per components.

1. 3 Thesis Outline

This thesis is contained in seven chapters. The first chapter is a brief introduction, provides an overview of current energy supply and demands. Moreover, it examines RE systems contribution in global energy mix and address the importance of increasing renewable resource share. Of the solar energy research development, have been presented followed by the thesis objectives and motivation.

In the second chapter, covers the essential backgrounds and concepts. Several subjects are considered including solar energy, solar concentrating technologies, CO_2 thermo-physical properties, and ammonia water absorption systems. This chapter is aimed to develop an understating of certain concepts that will be frequently used in later chapters.

The third chapter presents a comprehensive literature review on the following themes: 1) CSP plants energy and exergy studies, 2) S-CO_2 based power cycles, 3) TES integration to CSP plants, and Ammonia/Water absorption refrigeration systems. Furthermore, special attention is given to energy and exergy studies on solar based integrated systems.

The fourth chapter, embraces systems detailed descriptions includes the systems layout figures and a description of the different constitutes subsystems. The physical and chemical properties of the selected equipment and materials are tabulated.

The fifth chapter deals with thermodynamic analysis and mathematical modeling of the proposed systems. The analysis approach is presented and the energy and exergy balance equations are written for each component.

The sixth chapter is devoted for presenting the results and outcomes of this research. These results are then, critically discussed and compared with previous published literature for validation. Additionally, the impact that this result may have on the industrial scale of CSP is addressed.

In chapter seven, the conclusions of this thesis are delivered as associated with the future work recommendation and the promising directions that could be an extension to the current work.

Chapter 2: Background

In the last few decades, solar energy based energy systems for power production have experienced significant development; however, these have not reached a competitive level with traditional fossil fuel based power plants. Therefore, extensive research is required to overcome the current challenges facing the commercialization of solar generated electricity. In addition, a future energy solution must consider the environmental impact of the technologies as well as the economic aspect. Solar based integrated systems have a major potential in satisfying global energy demand, although studying such integrated systems commonly involves investigating multiple systems and how they can be efficiently combined to achieve the above mentioned goals.

Solar energy is considered as the most attractive renewable energy source that can provide a solution to the major world energy challenges that can be summarized in, climate change and energy shortage. However, a way forward significant solar energy share in the global energy mix must include research and policy stages. Thus, research can increase solar energy systems reliability and performance while policies can help implement the research outcomes in a better way.

In the current study, the integration of S-CO_2 Rankine cycle combined with ARS in a solar concentrating power system is thermodynamically investigated using both energy and exergy analyses to examine the overall integrated system energy and exergy efficiencies as well as individual component performance. The exergy analysis of this integrated system is expected to provide further insight beyond common energy analysis. The evaluation of the exergy destruction rate that occurs per system element is an excellent diagnosing tool though which the components with the most deficiencies can be easily identified.

Before introducing a related literature survey or presenting a more detailed analysis, the current chapter is developed to cover a wide range of important concepts and definitions that will be essential for understanding and analyzing this research problem.

2. 1 Solar Energy

The sun's characteristics, geometry and position play an important role in defining solar energy terminology in general, and solar radiation availability and variation in particular. Therefore, the sun's dimensions, sun-earth relations and other related subjects will be briefly discussed in the following sections.

2. 1. 1 Solar Radiation Constant

The sun is estimated to have a surface of blackbody temperature of 5777 K. However, the sun's internal temperature is expected to be about 1400 to 7000 times greater than that at the surface. It has a spherical shape with a dimension of 1.39×10^9 m. The distance between the sun and the earth varies according to the earth's orbital rotation from 152.1×10^6 km in the summer solstice, to 147.1×10^6 km in the winter solstice. This variation is only about ± 1.7 %, which maintains almost constant solar radiation reaching the earth's atmosphere. The solar radiation constant is about 1367 (W/m^2). A schematic representation of the sun-earth layout and relations is illustrated in Fig. 2.1.

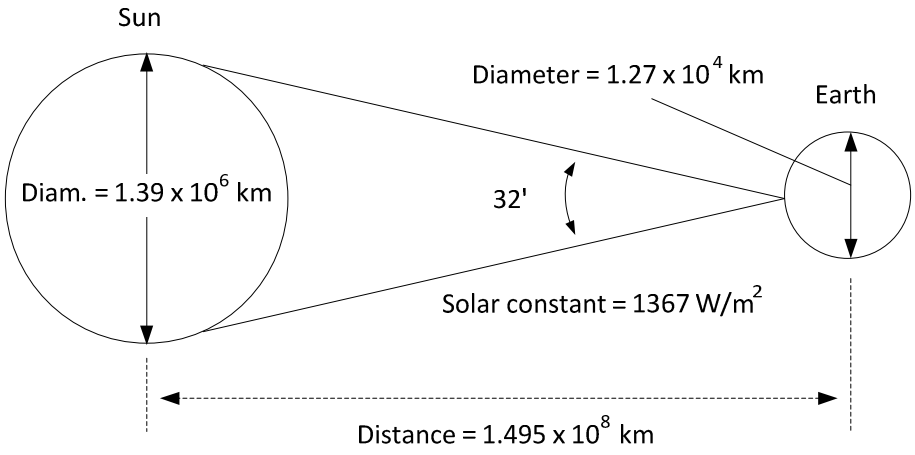

Figure 2.1: Sun-earth relationships (adapted from Duffie and Beckman, 2006).

2. 1. 2 Extraterrestrial Radiation

Extraterrestrial radiation can be defined as the solar energy radiated per unit time that would strike a unit area of the earth's surface if not partially scattered and/or absorbed by the atmosphere layer. There is a limited variation (about 3.3%) in the extraterrestrial radiation caused by two main reasons: variation in the sun-earth distance and variation in the sun's emitted radiation. On any day of the year, N, the extraterrestrial radiation, G_{on},

can be determined, according to Duffie and Beckman (2006), from the information of the solar constant G_{sc} as

$$G_{on} = G_{sc}\left[1 + 0.033\,cos\left(\frac{360N}{365}\right)\right] \tag{2.1}$$

The variation in the extraterrestrial radiation with the day number of a year can be seen in Fig. 2.2, for the maximum, average, and minimum solar constant values.

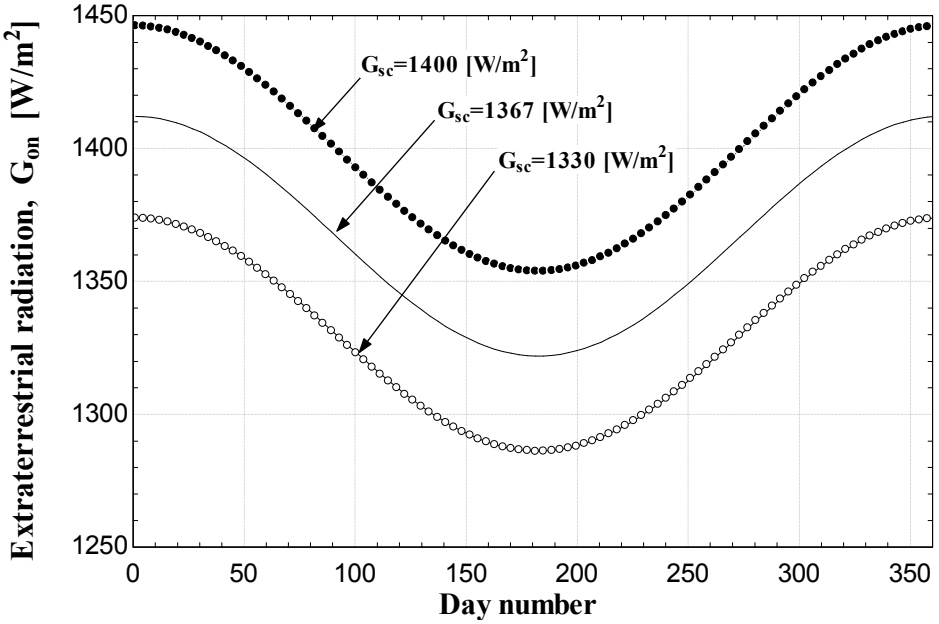

Figure 2.2: The variation in extraterrestrial radiation for three solar constant values high, low and average, with the different days of a year.

2. 1. 3 Spectral Distribution

Solar radiation energy can be distributed over a range of wavelength λ, at which it is emitted at varying from about 0.2 μm to 8.0 μm. However, most of the radiation received on the earth is in the range of 0.3 μm to 3.0 μm. This is mainly because of the atmospheric effect. Atmospheric molecules such as air, dust, water, CO_2 and O_3 are responsible for scattering and absorbing some of the extraterrestrial spectral irradiation. According to the wavelength, solar irradiation can be classified into ultraviolet, visible, thermal and infrared. The effect of atmospheric constituents on exterritorial radiation is shown in Fig. 2.3.

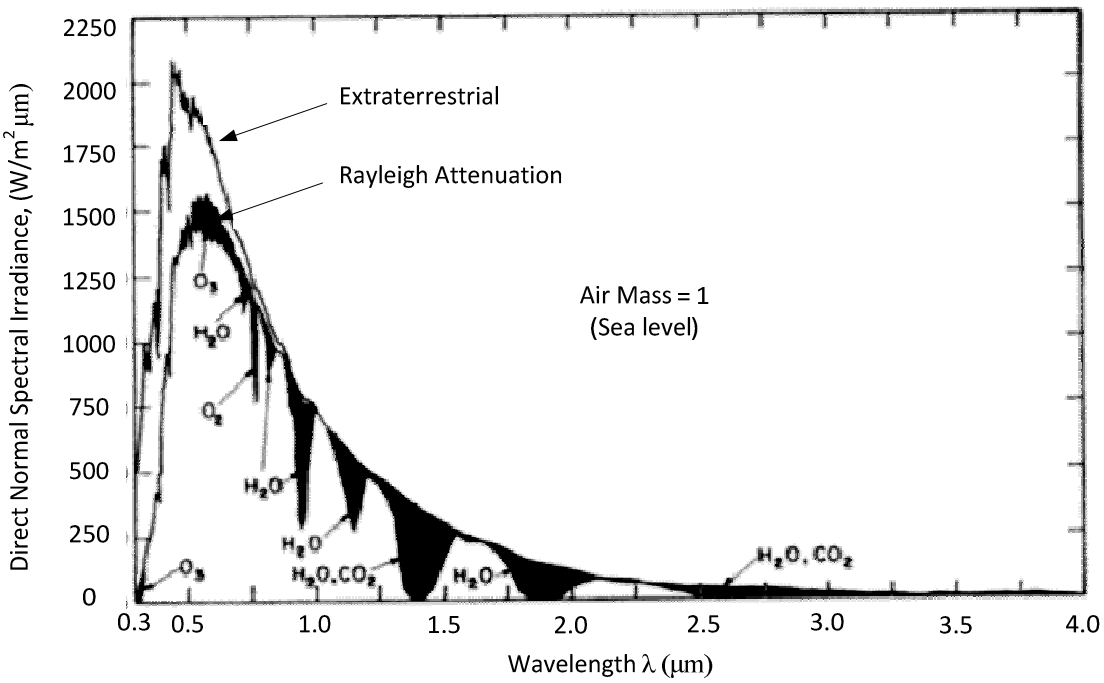

Figure 2.3: The effect of atmospheric absorption and scattering on the spectral distribution of direct normal irradiance (adapted from Duffie and Beckman, 2006).

After the extraterrestrial radiation experiences scattering, reflection and absorption while passing through the atmosphere, it decomposes to two components: beam radiation and diffused radiation. The following are definitions of the key terms as used throughout this thesis:

Beam radiation (I_b):

It is defined as the solar radiation received from the sun without change in its original direction. It is also referred to as direct normal radiation.

Diffuse radiation (I_d):

It is defined as the solar radiation received from the sun after its direction is changed through reflection and scattering by atmospheric molecules.

Global radiation (I_g):

The total radiation which combines both beam and diffuse radiation and given by

$$I_g = I_d + I_b \tag{2.2}$$

Irradiance:

It is defined as the power incident per unit area of the receiving surface, (W/m^2).

Irradiation (Insolation):

It is defined as the energy incident on a surface per unit area.

Air mass (AM):

The path length of radiation through the atmosphere, considering the vertical path at sea level as unity. Thus, at sea level AM=1 (when the sun is directly overhead, at zenith).

$$AM = sec\,\theta = \frac{1}{cos\,\theta} \tag{2.3}$$

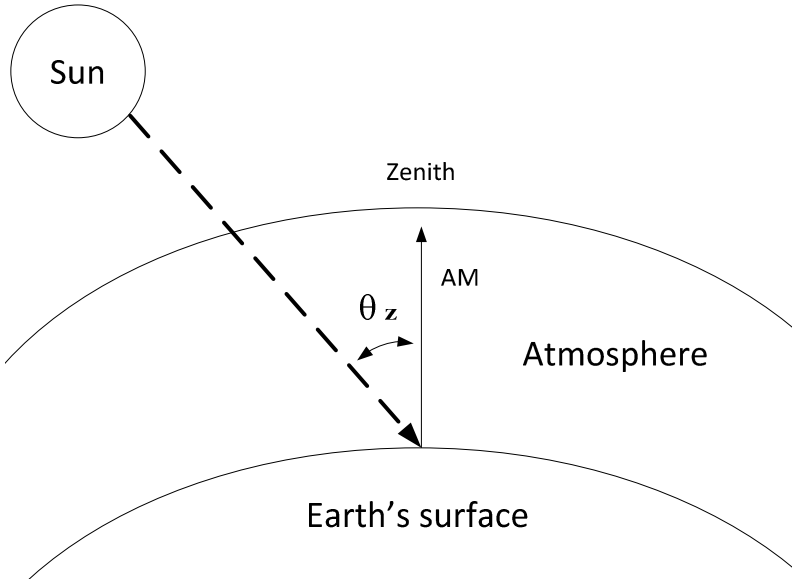

Figure 2.4: Illustration of the air mass AM.

Instruments:

The two instruments that are used commonly for the solar radiation measurements are defined as follows, according to Duffie and Beckman (2006):

1- Pyrheliometer; a device uses a collimated detector for measuring direct (beam) solar radiation from the sun.

2- Pyrometer; a device for measuring total hemispherical solar (beam + diffuse) radiation, usually on a horizontal surface. It can measure diffuse radiation only once it is shaded from the beam radiation.

The solar radiation amount and direction is closely linked with the sun's motion across the sky. Therefore, it is important to develop the proper definition and relationships that accurately describe the sun's position. Several fundamental definitions and relations of some solar angles are presented in Table 2.1.

Table 2.1: Definitions of the different solar angles.

Symbol	Name	Definition
φ	Latitude	The sun's angular position with respect to the equator, south or north. ($-90^0 \leq \varphi \leq 90°$) where north is positive
β	Slope	The angle between horizontal ground and the plane's surface ($0^0 \leq \beta \leq 180°$)
θ_z	Zenith angle	The angle between the direct beam from the sun and the vertical line
δ	Declination	The angular position of the sun at solar noon. ($-23.45^0 \leq \delta \leq 23.45°$)
γ	Surface azimuth	The angle between the projection on a horizontal surface and the normal to the object is surface.
θ	Incidence angle	The angle between the radiation beam incidence line and the line normal to the receiving surface.
α_s	Solar altitude	The angle between the horizontal plan and the radiation beam line, $\alpha_s = 90 - \theta_z$
γ_s	Solar azimuth	The angle that the radiation line projection on the horizontal plane makes with the south.
ω	Hour angle	The angular movement of the sun east or west of the local meridian due to the earth's motion around its axis at (15°/hour).

Fig. 2.5 illustrates the different angles above mentioned in Table 2.1 and the relationships between solar radiation and a plane's object or surface on the earth.

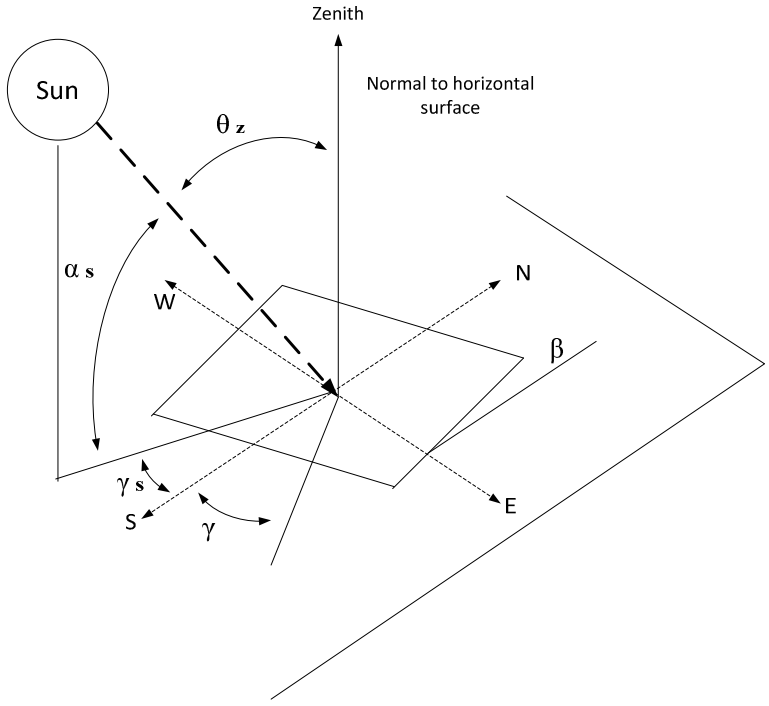

Figure 2.5: The different angles used to define solar radiation directions.

2. 1. 4 Solar Energy Resource Data

A primary stage in designing a solar power plant is the selection of the proper location. This process involves the evaluation of a number of factors. However, the high potential of the site is considered the most important among these factors. Therefore, the availability of accurate solar radiation data is fundamental for a reliable energy and cost assessment for the potential locations. There are different types of solar resource data; some are locally measured, other either modeled or collected from satellite measurements.

In spite of the fact that weather patterns are changing from year to year, the historical solar resource data are the most preferable for solar plant output prediction. The uncertainty that may rise from the weather changing over the years can be reduced in future weather forecasting when a longer data history is available. Thus, the longer the data history, the less the uncertainty.

Typical meteorological year (TMY) datasets are long term weather data collected over a period of 15 to 30 years and statistically processed to show the typical climate for a specific location (Stoffel, 2010). TMY data are commonly used to evaluate solar resource potential for the targeted locations and to compare their annual power output. Subsequently, a premium site can be selected. However, for plant monthly or daily performance optimization and operation strategies more temporal data with extreme conditions are needed.

2. 2 Concentrating Solar Power (CSP) Plants

CSP plants concentrate solar beam radiation to a receiver where the concentrated radiation heat is absorbed and transferred to a fluid. The fluid (heat transfer fluid) transports heat energy to a heat engine such as the steam Rankine cycle, where the heat can be converted to a mechanical energy and then electricity. Currently, there are four solar power production technologies classified under CSP plants:

- Parabolic trough technology
- Central receiver towers (or solar towers)
- Liner Fresnel reflectors
- Parabolic dish-Stirling systems

The main difference between the above mentioned technologies is the collector configuration. Fig. 2.6 schematically shows the layout of these collectors.

2. 2. 1 Parabolic Trough Technology

Parabolic trough technology is comprised of parabolic trough collectors (PTCs), receivers, a supporting structure, a single-axis tracking system and a piping system. Parabolic-shaped reflectors are used to reflect and concentrate solar beam radiation to its focal line. A metal tube (receiver) is then placed along the reflectors' focal line to intercept reflected beam radiation. The receiver tube is coated with a black material to enhance heat radiation absorption and is covered with a glass tube to reduce convective heat losses to the environment. A schematic representation of a typical parabolic trough CSP plant with thermal energy storage and a reheat steam Rankine cycle is shown in Fig. 2.7.

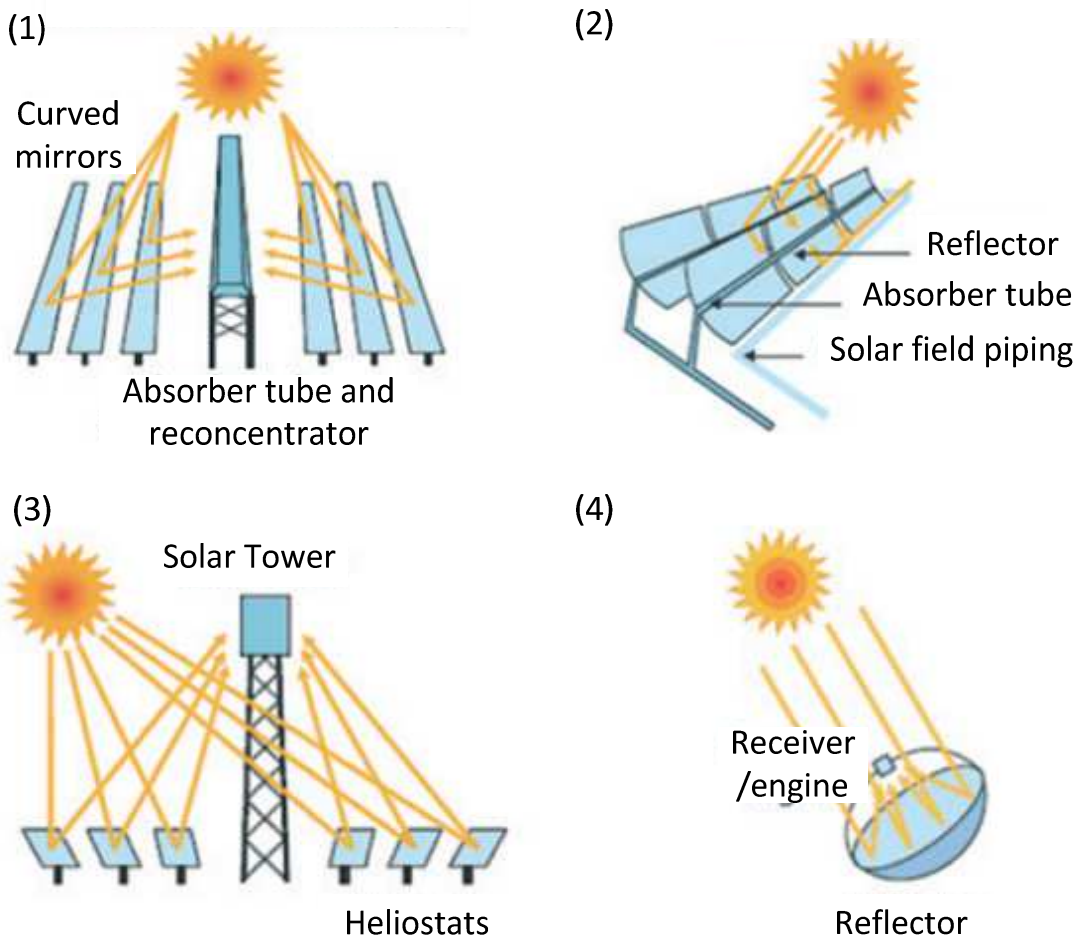

Figure 2.6: Solar concentrating technologies; (1) linear Fresnel reflectors, (2) parabolic trough technology, (3) central receiver rower, (4) parabolic dish-Stirling collector, (adapted from Quaschning, 2003).

Parabolic trough technologies have been used since the 1980s, when nine Solar Electric Generating Systems (SEGSs) were built in the Mojave Desert of Southern California. These SEGS plants have a total of 354 MW installed capacity. Thereby, parabolic trough based CSP systems are considered the most advanced and commercially proven technology among all other types of CSP plants (Kalogirou, 2009).

PTC has a concentration ratio of 70 to 80 suns, and an operating temperature in the range of 290 to 550 °C. Thermal energy storage can be easily integrated to a PTC based plant or it may be hybridized with a natural gas back-up system, to extend its full

load operating hours, as is the case of a number of operating PTC plants. The peak efficiency of PTC based CSP plants is between 14 to 20% and the annual solar-to-electricity net efficiency is about 11 to 16%, as reported by Kuravi et al. (2013).

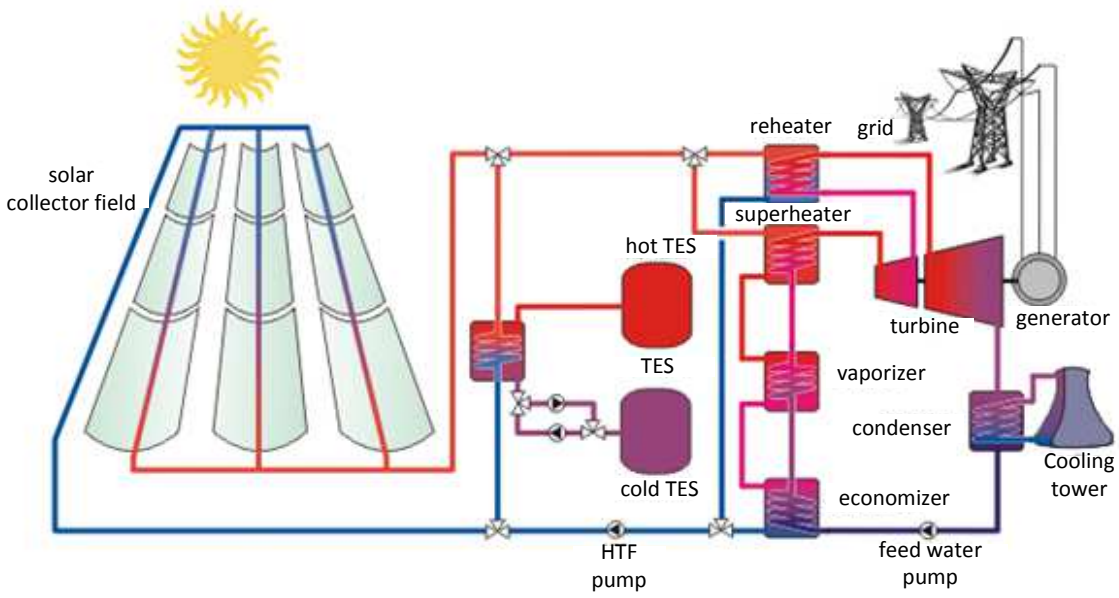

Figure 2.7: Schematic representation of a typical PTC based CSP plant with a TES (adapted from Quaschning, 2003).

2. 2. 2 Central Receiver Towers

A central receiver tower, also known as heliostat field collectors (HFCs), consists of a large number of flat mirrors (heliostats) distributed around a tower on which a receiver is mounted. A tracking system is used to adjust the heliostats to reflect solar beam radiation to the common receiver. A heat transfer fluid is then used to transport heat from the receiver to a power block where the heat is converted to mechanical energy to drive a generator and eventually produce electricity. This technology is capable of reaching high concentration ratios of about 300 to 1500 suns, which lead to higher HTF temperature and subsequently higher efficiency. A central receiver tower uses a single receiver at one location; therefore it reduces piping system energy losses and cost. However, this technology is suitable for large scale facilities (more than 10 MW) to be economically feasible (Kalogirou, 2009). From a technology maturity perspective, central receiver towers are considered to be in early commercial stages; several pilot plants have

demonstrated success and currently a number of plants are under construction. A schematic representation of a typical central receiver is shown in Fig. 2.8.

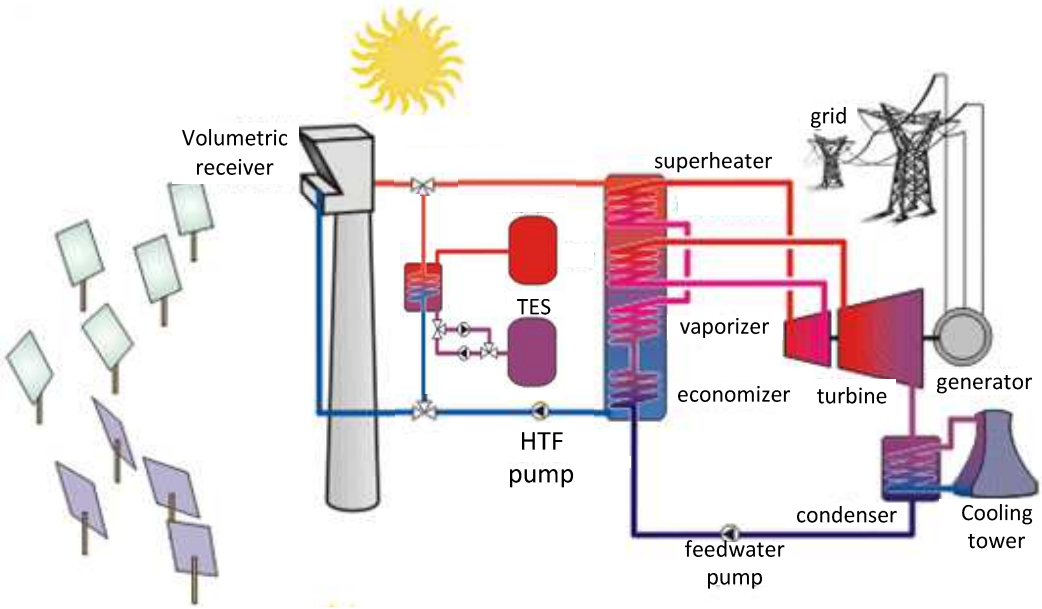

Figure 2.8: Schematic representation of central receiver based CSP plant with TES (adapted from Quaschning, 2003).

Central receiver tower technology has a solar field operating temperature between 250 to 650 °C. Its peak efficiency is in the range of 23 to 35% for a combined cycle turbine while the annual solar-to-electricity net efficiency is about 7 to 20 % (Kuravi et al., 2013).

2. 2. 3 Linear Fresnel Reflectors

A Linear Fresnel reflector (LFR) uses arrays of linear reflector strips that reflect and concentrate solar beam radiation to a linear receiver which is commonly mounted on a fixed tower to be in parallel with the reflectors. Fig. 2.6 system number (1) schematically shows the layout of LFR arrays and the receiver. LFR technology is considered to be in the pilot scale project stage where it needs a significant amount of research to be commercially available. However, one of the advantages of this technology is the cheap material and the fairly simple shape to manufacture which could reduce the system cost.

On the other hand, a major challenge facing LFR technologies is the shading and blocking by adjacent reflectors, in order to overcome this problem, an increase in reflector spacing and receiver height must be made. Accordingly the cost will increase.

LFR technology has a concentration ratio of more than 60 suns, with a solar field operating temperature in the range of 250 to 390 °C. It is capable of achieving around 18% as plant peak energy efficiency.

2. 2. 4 Parabolic Dish-Stirling System

Parabolic dish-Stirling technology is quite different from the above mentioned technologies since it mainly depends on Stirling heat engine rather than conventional cycles such as the steam Rankine cycle or the Brayton gas cycle. In addition, it uses a parabolic dish, with two-axis tracking system, to concentrate solar beam radiation to the focal point of that dish parabola where a receiver is placed to utilize the concentrated heat energy. The system number (4) in Fig. 2.6 shows a schematic representation of the parabolic dish reflector and receiver layout. In parabolic dish-Stirling systems, it is common to use a Stirling engine-generator unit attached directly to the receiver to produce electricity. Heat also can be transported from the multiple parabolic dish receivers to a central heat engine where the electricity is generated.

Parabolic dish collectors have concentration ratios in the range of 600 to 2000 suns; therefore, they are capable of achieving a fluid temperature as high as 1500 °C (Kalogirou, 2009). The energy peak efficiency of parabolic dish-Stirling systems can reach 30% and the annual solar-to-electricity net efficiency is about 12 to 28%. However, this technology is still in development stages and has not been commercially proven in spite of the demonstration projects that have been built in multiple locations.

2. 3 Thermal Energy Storage (TES)

One of the major challenges facing all types of RE based systems is that most of these resources encounter a fluctuating energy production due to the intermittent nature of such an energy resource. This includes solar energy based systems such as PV cells and CSP plants, wind and tides energy systems. However, in the case of CSP plants a TES system

can be incorporated to make the plant energy production more uniform and highly dispatchable.

TES systems have demonstrated several advantages over other current energy storage systems such as mechanical, chemical and magnetic storages. Two primary advantages are the high round-trip (charging, storing, and discharging) energy efficiency and the low cost. The energy efficiency of the TES integrated with the pilot Solar Two project is reported to be higher than 97%, according to Herrmann and Kearney (2002), as cited by Kuravi et al. (2013).

On the other hand, TES systems can have a positive contribution in reducing the environmental impact of electric generation power plants. Moreover, they may offer considerable economic benefits such as reducing energy cost, reducing power block size and increasing the utilization factor of the plant (Dincer and Rosen, 2011).

The integration of TES with CSP is expected to accomplish the following primary operations: (1) buffering: TES can eliminate the transient plant operation due to weather changing and variation in solar radiation due to clouds. (2) Dispatch energy: a storage system can be used to store thermal energy during the peak hours of solar field production and discharge stored energy at the time of peak energy demand. (3) Enhancing annual capacity factor: TES can significantly increase the annual operating hours of the plant through storing enough energy for continuous or extended hours further than the hours of sun availability (Kuravi et al., 2013).

Thermal energy storage systems are classified, according to storing methods, into three main types: sensible heat, latent heat, and chemical heat storage. There are several criteria that must be taken into consideration when selecting the material and mechanisms of a TES system, such as high thermal capacity, chemical stability, good heat transfer performance, and cost effectiveness. Currently, sensible heat storage is the most common TES system used for CSP plants. In sensible heat storage, the processes of storing thermal energy are associated with the temperature change of the storing medium. According to the storing medium material phase (liquid/solid) and type of configuration, there are four categories classified under sensible heat storage which are:

- Two-tank direct thermal energy storage,
- Two-tank indirect thermal energy storage,
- Single-tank thermocline storage, and
- Concrete thermal energy storage.

In the current system, the two-tank direct thermal energy storage is used. This system is comprised of two tanks (hot storage, cold storage), circulation pumps and an insulation system. The TES systems work in a cyclic operation manner involving three processes: charging, storing, and discharging. The two-tank direct TES uses the same HTF used for heat collection through the receiver's loop, to store thermal energy. The hot HTF coming from the field is stored in the high temperature (hot TES) tank; once it is needed, it flows through the power plant heat exchangers to be utilized for electric power generation. It then exits the heat exchangers at a low temperature and is stored in the low-temperature (cold TES) tank. The other types of TES will be considered in the literature review chapter, where related studies and figures are comprehensively presented.

2. 4 Absorption Refrigeration System (ARS)

An absorption refrigeration system (ARS) refers to an energy system that uses heat to provide a refrigeration effect. The performance and operating conditions of an absorption refrigeration system are strongly dependent on the properties of the working fluid used. An ammonia/water mixture has been used since the mid-1800s as a working fluid for absorption systems, thus is well-known technology. The components of an ammonia/water absorption refrigeration system are as follows: desorber, condenser, evaporator, rectifier, absorber, expansion valves, and heat exchangers. The layout of a typical single stage ammonia/water refrigeration cycle is shown in Fig. 2.9.

In the single effect absorption refrigeration system, the low pressure refrigerant (ammonia) evaporates in the evaporator while absorbing heat. It is then fed to the absorber where the refrigerant vapor is absorbed and the heat is released to the surroundings. The absorber strong solution is pumped to the desorber, raising the pressure from the evaporator pressure level to the desorber pressure. The solution passes through a heat exchanger in which the weak solution coming from the desorber is heated

by the strong solution, leaving the desorber to the absorber. In the desorber, the solution is heated by an external heat source, causing the refrigerant to evaporate. The weak solution is circulated to the absorber while the refrigerant vapor flows through the rectifier to improve its quality by condensing some of the water vapor that evaporates with the refrigerant. It is then sent to the condenser where it condenses and releases its latent heat to leave in a liquid phase. After that, an expansion valve is used to throttle the refrigerant and passes towards the evaporator where eventually it completely evaporates and the cycle is repeated.

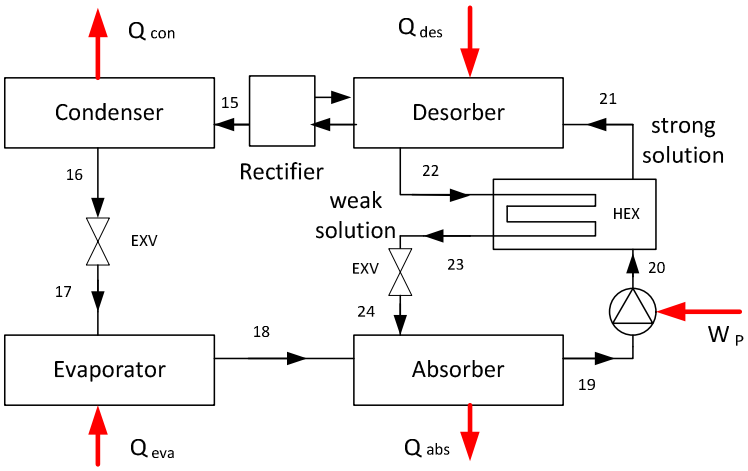

Figure 2.9: Schematic representation of a single stage ammonia water absorption cycle.

2. 5 Carbon dioxide (CO_2) Properties

The use of CO_2 as a working fluid in power cycles has been growing in interest because of the several advantages that CO_2 may have compared to conventional power cycles. CO_2 is a cheap non-toxic gas, and abundant in nature. Knowledge of the thermal and chemical properties of CO_2 is available. In addition, some recent work has demonstrated a practical project. For example, Niu et al. (2011) experimentally investigated a supercritical CO_2 Rankine cycle. More detail will be given in the relevant literature review in the following chapter.

The relevant thermo-physical properties of CO_2 are presented in the following figures (Figs. 2.10 and 2.11). The critical point of CO_2 is at a pressure of 7.37 MPa, and a temperature of 30.98 °C. Constant pressure lines are selected near the critical point of

CO_2 to show the significant variation in these properties. These figures are produced using the software Engineering Equation Solver (EES), in which built-in functions for thermo-physical properties for a number of materials are available (Klein, 2002).

Fig. 2.10 shows the variations of the CO_2 specific heats for constant pressure with temperature variation. It can be noticed that the specific heats of the CO_2 variations decrease with increasing pressure.

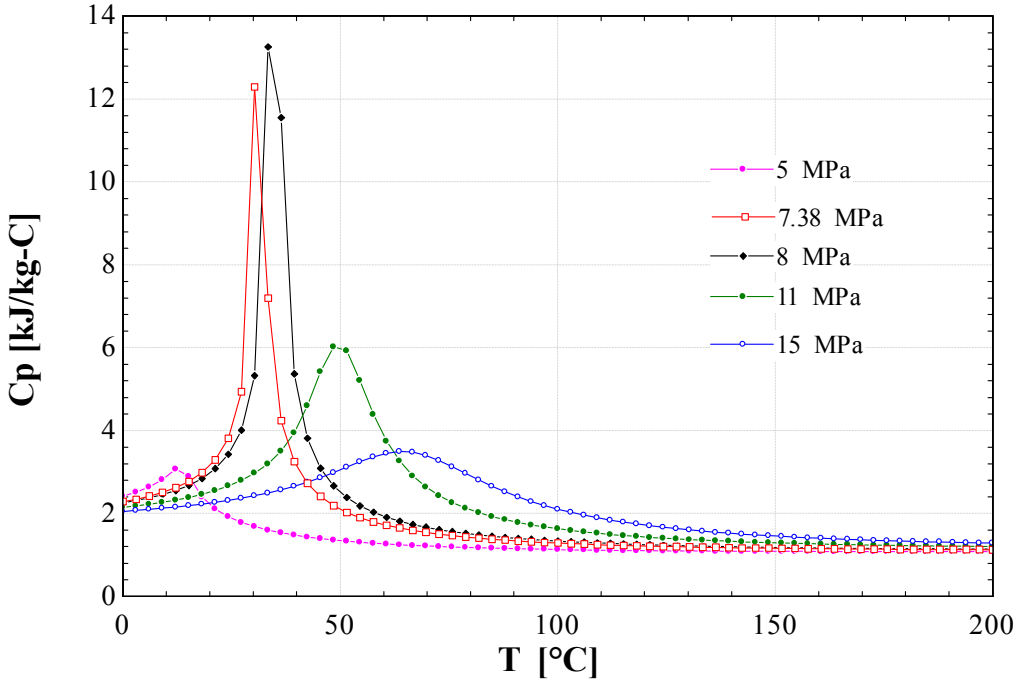

Figure 2.10: Carbon dioxide (CO_2) specific heat with temperature.

Fig. 2.11 shows the variation in the thermal conductivity of CO_2 for different constant pressure lines near the critical point. The thermal conductivity of CO_2 varies between 0.02 and 0.12 (*W/m-C*) for pressures in the range of 5 to 15 MPa. The thermal conductivity of decreases with temperature increases to be in the range of 0.05 to 0.02 (*W/m-C*) when the temperature is above 100 °C.

Fig. 2.12 shows the viscosity of CO_2 for constant pressure lines near the critical point with temperature. The CO_2 viscosity shows a sharp drop near critical temperature. The variations of these constant lines with temperature become less with higher temperatures.

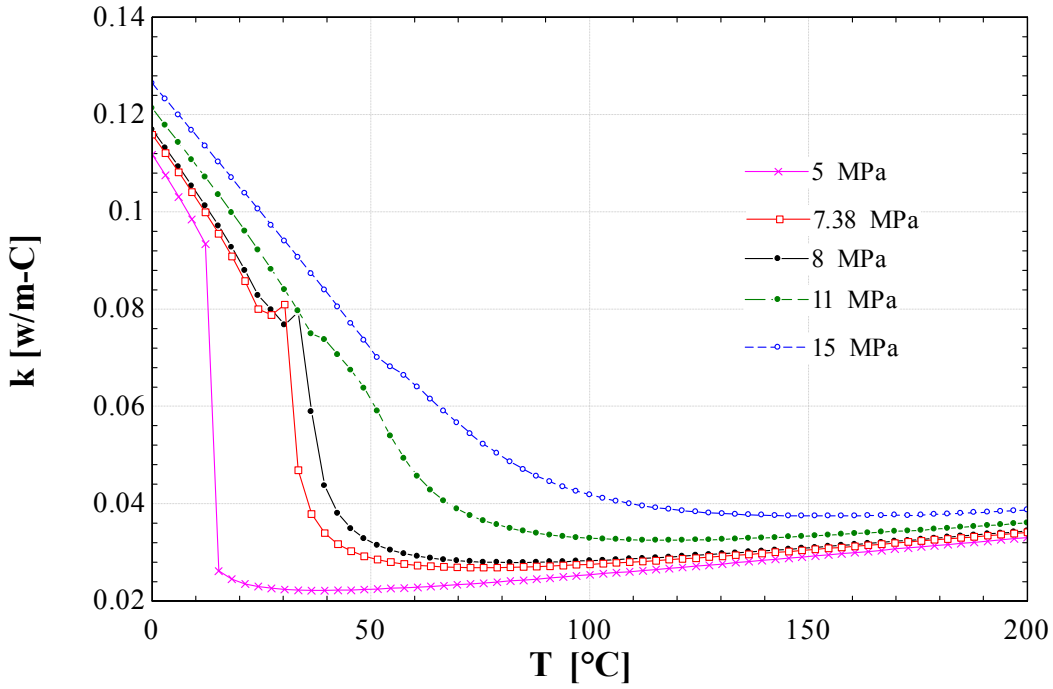

Figure 2.11: Carbon dioxide (CO_2) thermal conductivity with temperature.

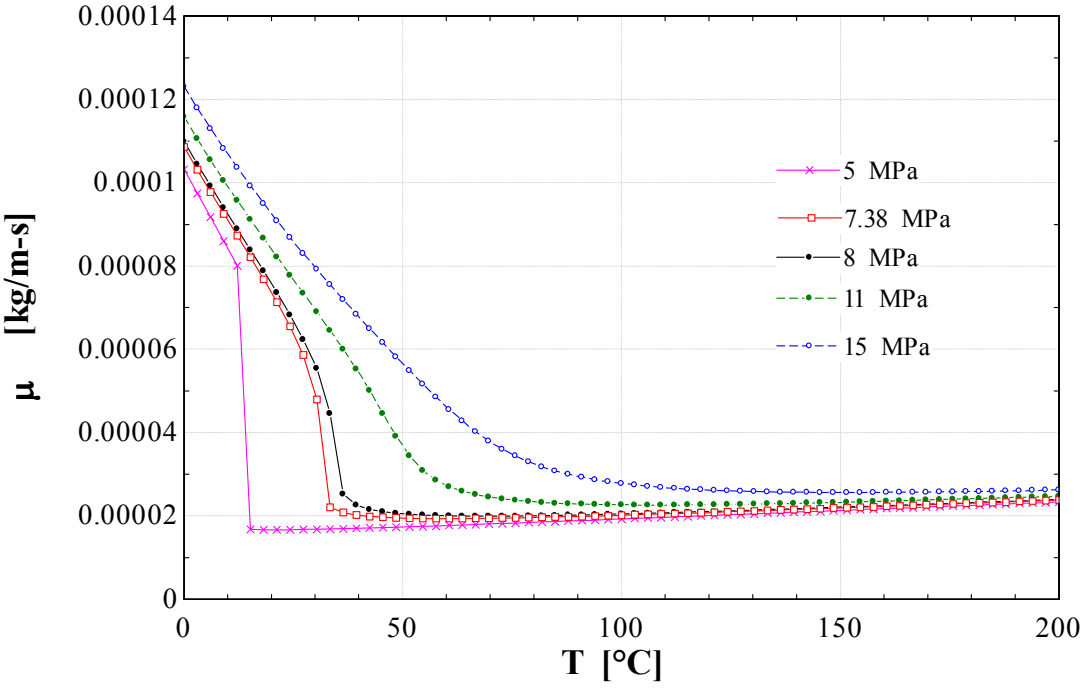

Figure 2.12: Carbon dioxide (CO_2) vescocity with temperature.

Fig. 2.13 shows the density of CO_2 for different constant pressure lines with temperature near the critical point. It can be noticed that the density of CO_2 decreases significantly with the increase in temperature. This phenomenon was an essential reason

for the continuous research efforts to utilize CO_2 in a Brayton power cycle. The power consumption for compressing the working fluid can be reduced significantly if this process is carried out just above the critical point. The reduction in the compression power will result in an improvement in the cycle efficiency.

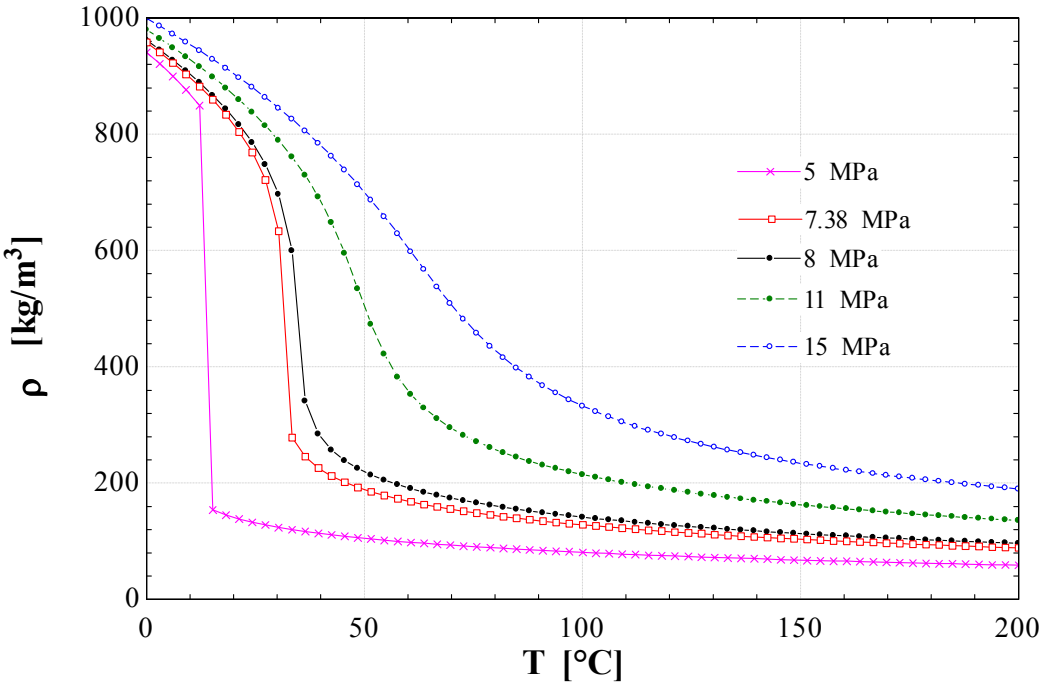

Figure 2.13: Carbon dioxide (CO_2) density with temperature.

Chapter 3: Literature Review

3. 1 Overview

International awareness of the severe environmental consequences of the continuous use of fossil-fuel-based energy systems is the main motivation for many researchers, scientists, and organizations to investigate alternative renewable-based energy systems. Furthermore, the depleting reserves of fossil fuel resources could lead to an unstable global economy.

3. 2 PTC Solar Field

Parabolic trough Concentrated Solar Power (CSP) plants are mainly comprised of a solar collector field, Thermal Energy Storage (TES), and a power generation block. The solar collector field consists of parabolic mirrors, receivers, and a single-axis-tracking system. The parabolic mirrors reflect and concentrate sunlight onto the receivers which are positioned along the focal line of the parabolic trough. Receivers, in turn, are connected in a series to form a loop through which heat transfer fluid (HTF) is circulated to absorb the heat generated by a solar concentrated beam. The HTF leaves the field loop with a high temperature to be pumped through a hot header and, based on the operating condition, either to the TES or directly to the power generation block.

An energy and exergy analysis was performed by Reddy et al. (2012) for a CSP system. They evaluated the energy and exergy losses and the efficiencies under the operating conditions of specific locations in India. It was found that the energy and exergy efficiencies of the plant increased by 1.49% and 1.51% with an increase in the cycle pressure from 9 MPa to 10.5 MPa.

Gaul and Rabl (1980) studied the incidence-angle modifier for a PTC and investigated the relation between a PTC test and long-term performance prediction of a solar field. Gupta and Kaushik (2010) proposed a direct steam generation trough-based CSP and conducted an energy and exergy analysis for different plant components. The maximum energy loss was found to be in the condenser and the PTC solar field. However, the maximum exergy destruction rate was reported to be in the PTC solar field.

Forristal (2003) developed a detailed heat transfer analysis of a PTC. The model was implemented in EES Engineering Equation Solver software. The code involves one and two dimensional energy balances. The model was validated and appeared to be in agreement with published experimental results. Therefore the one dimensional heat transfer approach was adapted by a number of studies including the current study.

Roesle et al. (2011) developed a model for heat loss in a PTC with active vacuum receivers using heat transfer software that includes different modes of heat transfer (conduction, convection and radiation). Al-Sulaiman (2014) carried out an exergy analysis of a number of PTC-based combined power cycles. The study examined the exergy efficiency and exergy destruction rate per component of different a configurations of steam Rankine cycle and an organic Rankine cycle.

Patnode (2006) conducted a detailed energy and heat transfer analysis for SEGS VI to evaluate heat losses and assess the plant performance. For this purpose, a model has been developed and solved using EES and TRNSYS software. It was reported that the operation at lower PTC solar field flow rates and higher field temperature will increase the net energy efficiency of the plant. On the other hand, in attempting to reduce plant water requirement, the impact of using an air-cooled condenser was examined and the results showed a considerable reduction in the power output estimated to be 1.3 MW. This is due to the increase in the condensation pressure and temperature.

It can be concluded from the literature review that there are few research studies that have considered energy and exergy analysis along with heat transfer analysis. Therefore, the current study is conducted to evaluate the exergy destruction rates in the different plant components. The energy and exergy efficiencies will also be examined under various operating conditions.

Furthermore, limited water reserves, especially at locations that were high potential for a CSP plant, such as deserts hot climate areas, it is highly desirable to develop a CSP integrated system that could reduce water consumption by the plant cooling system and maintain relatively good performance. Thereby, the current system is proposed to reduce the water demand.

3. 3 S-CO_2 Power Cycles

The interest in using CO_2 as a fluid in a power cycle has been growing over the last four decades, and this interest was motivated by a number of advantages that a CO_2 power cycle can achieve, compared to conventional cycles. The first proposal of a supercritical carbon dioxide (S-CO_2) Brayton cycle is credited to Ernest G. Feher back in 1967. Since then, several institutions have conducted a number of theoretical studies on S-CO_2 power cycles. However, a more recent work done by Dostal (2004) has resumed previous efforts in investigating (S-CO_2) by studying and optimizing number of CO_2 Brayton power cycles for nuclear application.

Seidel (2011) developed a simulation model for an S-CO_2 Brayton cycle for CSP applications. The model is used to assess the annual efficiency and energy production of the different S-CO_2 Brayton cycle configurations. Chacartegui et al. (2011) investigated different configurations of CO_2 cycles for central receiver CSP application. Bao et al.(2013) carried out a review on working fluid and expander selection for organic Rankine cycles. Sarkar (2009) carried out a second law based analysis of the S-CO_2 recompression Brayton cycle. The results showed that the heat exchangers have the maximum exergy destruction rates while turbo-machineries have less exergy destruction.

Perez-Pichel et al. (2012) conducted a thermal analysis of S-CO_2 power cycles. In this study, it was reported that a thermal efficiency as high as 43% is achievable.

Niu et al. (2013) optimized the solar collectors arrangement of an S-CO_2 Rankine cycle system. A cascaded arrangement of the solar collector was investigated to obtain best performance. The solar based S-CO_2 Rankine cycle has gained considerable interest by numerous researchers; however, the research group X. R. Zhang et al. (2006) and X. R Zhang et al. (2007) have conducted an extensive amount of both theoretical and experimental work.

Niu et al. (2011) experimentally investigated the heat transfer characteristics of the S-CO_2 fluid in solar collectors of a Rankine cycle. The results demonstrated the substantial effect of the CO_2 properties near critical point on the heat transfer behavior of the CO_2. Lakew, Bolland, and Ladam (2011) developed a new approach to improve the

performance of the S-CO_2 Rankine cycle by replacing the mechanical pump by a thermally driven pump. The results indicated that the thermally driven pump will consume more heat at a low temperature (around 60 ^{o}C) to pressurize the working fluid.

AlZahrani et al. (2013) conducted energy and exergy analyses on an integrated geothermal based energy system for power, hydrogen and heat production. The integrated system was comprised of S-CO_2 Rankine cycle cascaded by organic Rankine cycle, electrolyzer and heat recovery system. In this study the performance of the integrated system and the cycles was assessed through the energy and exergy efficiencies. It was reported that the S-CO_2 Rankine cycle has an energy conversion efficiency of 9.2% when a geothermal source temperature of 200 ^{0}C is used.

From the literature review, a conclusion can be drawn that the application of S-CO_2 is very attractive for CSP applications. The integration of an S-CO_2 Rankine power cycle with an absorption refrigeration cycle to condense the CO_2 by a low grade heat has not yet been proposed or studied by any research group. Therefore this study will consider the energy and exergy analysis of the entire system. In addition, it will evaluate the energy and exergy efficiencies and exergy destruction rate for the cycle and different operating conditions.

Chapter 4: System Description

4. 1 Overview

The block diagram of the conceptual design of the system is shown in Fig. 4.1, while the detailed system configuration and layout is illustrated in Fig. 4.2. It consists of four major subsystems: the PTC solar field, thermal energy storage (TES) unit, supercritical carbon dioxide (S-CO_2) Rankine cycle, and single stage ammonia/water absorption refrigeration (ARS) system. The solar collector field encompasses a number of parabolic trough arrays which concentrate solar beam radiation onto receivers. This concentrated solar radiation generates heat energy, which is absorbed by a heat transfer fluid (HTF) flowing through the receivers. The HTF transports the absorbed heat to the power block where it can be utilized for electric power production.

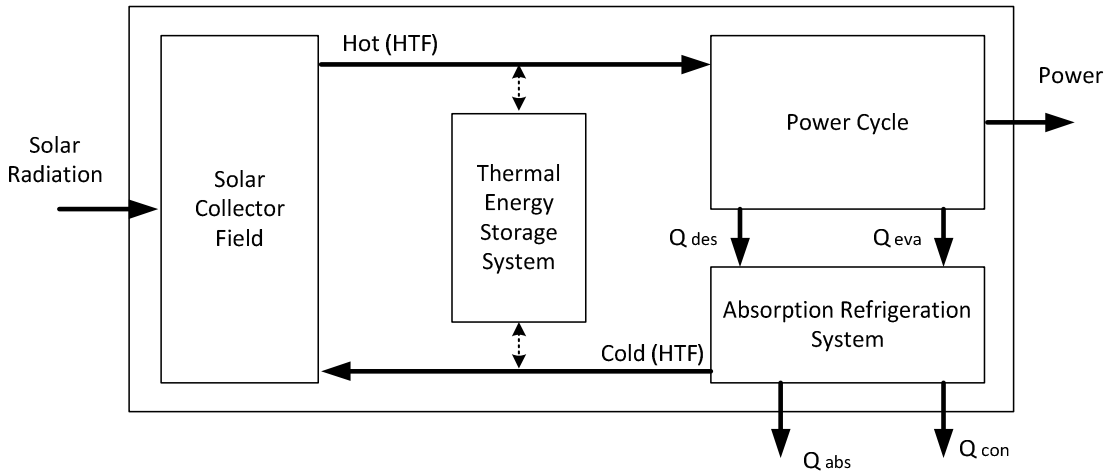

Figure 4.1: Block diagram of the conceptual design of the integrated system.

The conventional systems rely mainly on the steam Rankine cycle to be used in the power block for heat energy conversion to electric power. The current system uses the same Rankine cycle, but with different working fluid. This cycle uses CO_2 as a working fluid. The integrated system's power block is configured of a reheat S-CO2 Rankine cycle with an internal heat exchanger. The CO_2 is first heated in the internal heat exchanger, through a regenerative process, then in the heater. During these heating processes, the CO_2 state changes from a low temperature liquid phase to a high temperature supercritical gaseous state. High CO_2 gas is then allowed to expand through

a high pressure turbine (HPT) and returned to the reheater to be heated again at constant pressure before being sent to a low pressure turbine (LPT) to expand to the condenser pressure.

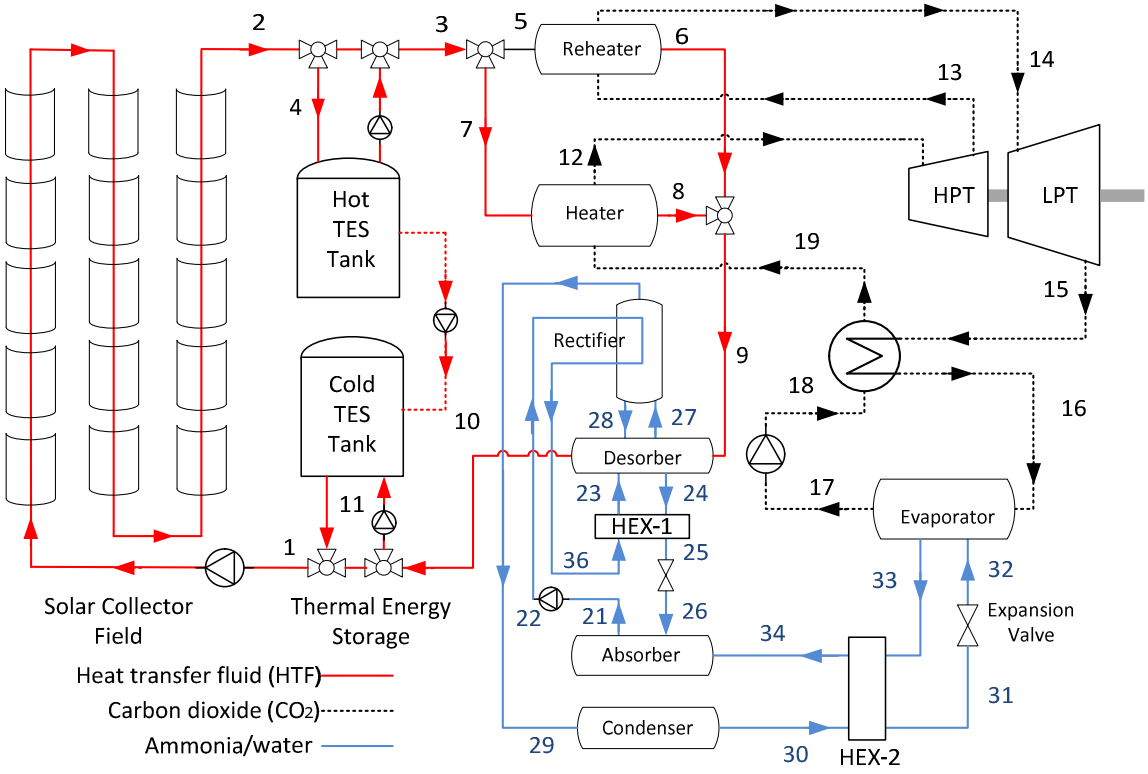

Figure 4.2: Schematic diagram of the overall system layout with the different state points.

Since CO_2 has a relatively low critical temperature, 31^0 C, the condensation process of CO_2 could be challenging or impossible for both wet and air cooling systems. However, for the cycle, a new integrated cooling system has been developed to achieve the cooling/refrigeration target at different operation conditions.

The condensation process takes place in a special condenser enhanced with a cooling system capable of cooling CO_2 to a temperature of about -5 ^{0}C where it eventually condenses to leave in liquid form. Thus, liquid CO_2 can be easily pumped to repeat the same cycle. The cooling system is based on a single stage ammonia/water absorption cycle that utilizes a portion of the heat leaving the heater and reheater to thermally drive the cycle.

To extend the system's power production at night or on a cloudy day without using a fossil fuel backup system, a thermal energy storage system (TES) is incorporated. TES is located between the PTC solar field and the power block. It consists of two tanks for hot and cold storage. The hot storage tank is used to store the surplus high temperature HTF coming from the PTC solar field during solar radiation peaks. At night or when solar radiation is interrupted by clouds, this energy can be discharged to the power block to maintain continuous power production. Low temperature HTF then leaves the power block to be stored in the cold storage tank, before being sent to the PTC solar field to be reheated.

4. 2 PTC Solar Field

The solar collector field is the area responsible for harvesting sun radiation heat through numerous arrays of parabolic troughs. The parabolic trough solar collectors (PTC) are comprised of parabolic mirrors (reflectors), receivers, and a single-axis-tracking system. The parabolic mirrors reflect and concentrate the solar beam radiation onto the receivers, which are positioned along the focal line of the parabolic troughs. The heat generated by the concentrated solar beam is then absorbed by the heat transfer fluid (HTF), which is circulated through the receivers. The solar field consists of three loops connected in a series; each loop is composed of a number of solar collector assemblies (SCA). The SCA is about 100 m in length and includes reflectors, receivers, supporting structures and an independent tracking system. The collector trough type selected for PTC is Luz system LS-3 collectors. These collectors are manufactured of galvanized steel so that they can meet commercial scale demand. Luz system collectors have been used in SEGS power plants where they have demonstrated a high reliability (NREL, 2010). The dimensions and specifications of LS-3 are presented in Table 4.1. The various components of the PTC loop are illustrated in Fig. 4.3. The overall solar field layout and the HTF cycle as a part of the integrated system is presented previously in Fig. 4.2.

The receivers (or so-called: the heat collection elements (HCEs)) are configured to be capable of absorbing as much as possible of the concentrated heat and to ensure as low as possible to the environment. Thus, a receiver consists of a metal tube coated with special material to increase the absorptivity and decrease the emissivity.

Table 4.1: Solar collector technology and specifications (adapted from SAM, 2012).

Component	Specification
Trough Type	Luz LS-3
Aperture width (m)	5.75
SCA length (m)	100
Focal length (m)	2.1
SCA Aperture reflective area (m^2)	545
Concentration ratio	82
Tracking error and twist	0.99
Geometric accuracy	0.935
Mirror cleanliness (average)	0.98

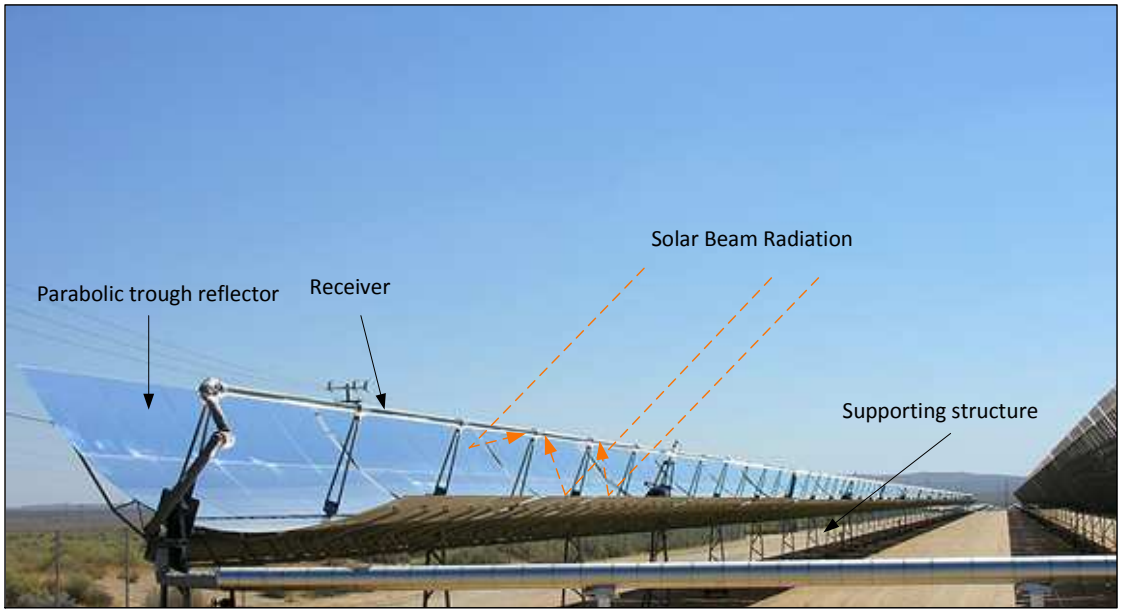

Figure 4.3: Parabolic trough collector assemblies with the differnet componetes (photo source; Wikiperia, 2013).

The metal tubes are enclosed in glass envelope to reduce the convective heat losses to the environment. The receiver is a critical part of a PTC power plant and the ability to reduce heat losses from receivers will result in higher temperature HTF produced by the PTC solar field, and subsequently, higher overall plant efficiency. A partial view with the different receiver components is illustrated in Fig. 4.4.

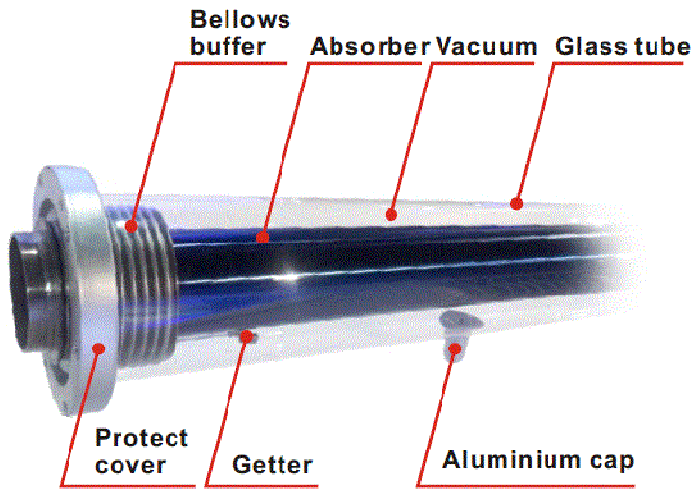

Figure 4.4: Partial view of parabolic trough receiver (HCE) (adapted from Beijing Sunda Solar Energy Technology Co).

The absorber tube is made mainly from stainless steel coated with special material, with bellows at inlet and outlet. These bellows are glass-to-metal seals designed to minimize heat conduction loss while maintaining the vacuum enclosed by the glass cover. The glass cover is made to withstand the high temperature operating condition. In addition, the outer glass is commonly treated to improve its transmittance to solar radiation and reduce its reflectivity. The getter is used to absorb the hydrogen that penetrates through the receiver tube from the HTF. The getter is a vacuum indicator that shows a different color when vacuum is lost. The receiver, manufactured by SCHOTT solar (SCHOTT PTR® 70), is selected for the present study. The dimensions and specification of the SCHOTT PTR® 70 receivers are given in Table. 4.2.

The synthetic heat transfer oil (Therminol-PV1) is used as a HTF. Therminol-PV1 is a eutectic mixture of 73.5% diphenyl oxide and 26.5% biphenyl. It is designed to match the demanding requirements of liquid phase applications from 12 to 400 °C, and vapor phase applications from 257 to 750 °C (Therminol®). The wide range of the Therminol-PV1 liquid phase temperature has made it preferable for the plant operating conditions. The relevant properties of the Therminol-PV1 are presented in Table 4.3. The

thermodynamic properties of the Therminol-PV1 at the different state points of the system are evaluated using the Engineering Equation Solver EES (Klein, 2002).

Table 4.2: Technical specification of the SCHOTT PTR® 70 receiver (adapted from SCHOTT solar).

Components	**Specification**
Dimension	Length: 4.060 (m) at 20 ° C
Absorber	Outer diameter: 0.07 (m) Material: steel DIN 1.4541 or similar Absorptivity, $\alpha_r \geq 0.955$ Thermal emittance, $\varepsilon_r \leq 0.095$ at 400° C
Glass envelope	Material: borosilicate glass Outer diameter: 0.125 (m) Solar transmittance, $\tau_c \geq 0.965$
Vacuum	Gas pressure $\leq 10^{-3}$ mbar
Operating pressure	$\leq$ 40 bar (absolute)

Table 4.3: Relevant properties of the heat transfer fluid (Therminol-PV1) (adopted from Therminol®, 2013).

Parameter	**Value/Type**
Composition	Biphenyl and diphenyl oxide
Crystallization point (℃)	12
Flash point (℃)	124
Fire point (℃)	127
Auto-ignition point (℃)	621
Density at 25 ℃, (kg/m^2)	1060
Kinematic viscosity (mm^2/s) at 40 ℃ at 100 ℃	 2.48 0.99
Optimum use range (Liquid phase) (℃)	12 – 400

A circulating pump is used to circulate the HTF through the PTC solar field. The system is designed to produce HTF with a temperature of about 396 ℃ when solar radiation is available, and to keep this temperature constant the mass flow rate of the HTF is allowed to vary according to the intensity of the solar radiation. The HTF coming back to the solar field from the power block is expected to be about 60 ℃. Because of the temperature difference between the field inlet and outlet temperature, a larger PTC area is required to achieve the targeted temperature. Typically, a PTC solar field undergoes three operation modes depending on the availability of solar radiation:

1. No solar radiation
2. Solar radiation is less than that needed for full load operation
3. Solar radiation is more than that needed for full load operation

In the first mode, the solar field does not produce energy and for the power block to operate, it must either operate form the TES or use a backup system. While in the case of operation when solar radiation is not sufficient for full load operation, supplementary thermal energy can be withdrawn from the TES or external source, otherwise the power block will operate on partial load. However, in the third scenario, the solar field will produce more than what is needed and this surplus can be stored in the TES to be used at night.

The PTC uses a single-axis tacking system where the PTC loops aligned in parallel with the south-north axis, while the sun is being tracked in the east-west axis. Defocusing techniques are used to avoid over production while the solar field HTF mass flow rate is over the maximum limit. The high temperature HTF leaves the PTC solar field at state point 2, as shown in Fig. 4.2, either to the power block or power block and the TES. In the flowing section, the TES will be discussed in more detail.

4. 3 Thermal Energy Storage

TES systems are considered as an essential part of fossil fuel independent solar thermal power plants. They are integrated between the supply and the demand in order to overcome the intermittent nature of the solar energy and to produce a stable form of thermal energy. In addition, TES dispatches the energy stored to target the peak periods

where electric power is more valuable. Thus, they eliminate or reduce fossil fuel consumption during peak demands and subsequently reduce the generation cost and improve the system's reliability.

The TES integrated in the current system is classified as two direct tank sensible TES. It consists of two tanks, one for high temperature HTF (hot TES tank) and the other for low temperature HTF leaving the power block (clod TES tank). As explained in previous chapters, direct TES system does not need heat exchangers to transport heat since it simply uses the same HTF as the storing medium. Therefore, the excess HTF flow is sent to the hot TES tank (charging mode) and whenever the solar field production is not sufficient, this stored HTF can be pumped to the power block (discharging mode). The HTF leaves the power block to the solar field during the solar field operation period. However, at night time, when the solar field is not in operation, the low temperature HTF can be stored in the cold TES tank, to be pumped out to the solar field the next day at peak radiation hours.

The two direct tanks TES have several advantages over other types of TES. For example, the heat exchanger costs that are associated with the two indirect TES systems are eliminated. In addition, higher temperature HTF can be delivered to the power block, since the temperature difference in the heat exchange processes (charging and discharging) between the HTF and the TES medium is eliminated. Therefore, the cycle efficiency will be higher as subsequently the overall plant efficiency for the same solar field temperature output.

The TES layout as part of the overall integrated system is shown in Fig. 4.2. The size of the TES mainly depends on the hours of full operation that can be supplied from the storage tanks. The thermal properties of the material used as storing medium are an important factor upon which the TES volume can be calculated. The properties of the HTF (Therminol-PV-1) used for storing heat are presented in Table. 4.2.

4. 4 Reheat S-CO_2 Rankine Cycle

During the last decade, there was a growing interest in S-CO_2 as a working fluid for the Brayton gas cycle. However, up to now there are very limited studies conducted on S-

CO_2 for the Rankine cycle as discussed in the previous chapter in presenting the relevant literature. The main reason behind ignoring S-CO_2 Rankine is the challenging condensation process that requires a low temperature cooling medium. However, this problem is tackled and an S-CO_2 Rankine cycle is integrated with a cooling system in which the condensation process is successfully executed.

The S-CO_2 cycle layout and flow diagram is illustrated in Fig. 2.4. The cycle is composed of a CO_2 pump, an internal heat exchanger, a heater, a reheater, two turbines, high pressure turbine (HPT) and low pressure turbine (LPT), and a condenser integrated with a cooling system. The temperature –entropy (T–s) diagram of the cycle is shown in Fig. 4.5. Firstly, gaseous CO_2 at state point 19 inters the heater, where it is heated to a high temperature (about 390 °C) by the HTF coming from the solar field. Next, CO_2 is allowed to expand in the HPT form state 12 pressure (15 MPa) to state 13 of about 7.5 MPa pressure. The CO_2 is then heated in the reheater to state 14 of 390 °C.

Following this, CO_2 is allowed to expand in the LPT from state 14 to the pressure condenser level (about 3.77 MPa) at state point 15. Since the temperature of CO_2 gas at state 15 is still high enough to be utilized, it is sent to the internal heat exchanger to recycle its heat in a regenerative process before being sent to the condenser. The CO_2 is expected to leave the internal heat exchanger at state 16 with a temperature of 22 °C and subsequently enter the condenser where CO_2 will undergo a refrigeration process and eventually is condensed to leave the condenser as a liquid with a temperature of 3 °C. At this stage, the liquid phase is easy to pump, to the heater pressure level, to state 18, with a reasonable power input. The liquid CO_2 then leaves the pump to the internal heat exchanger to be heated by the hot stream coming from the LPT to state 19, where the cycle can be repeated.

4. 5 Absorption Refrigeration System

The absorption refrigeration system (ARS) utilizes a portion of the remaining heat that leaves the heater to generate a cooling effect in an evaporator. The ammonia/water absorption refrigeration system layout is presented in Fig. 4.6, which shows the different components of the cooling cycle. The system operates on a single-stage ammonia/water

absorption cycle and consists of the following: desorber, rectifier, condenser, expansion valves, evaporator, absorber, heat exchangers, and a solution circulation pump.

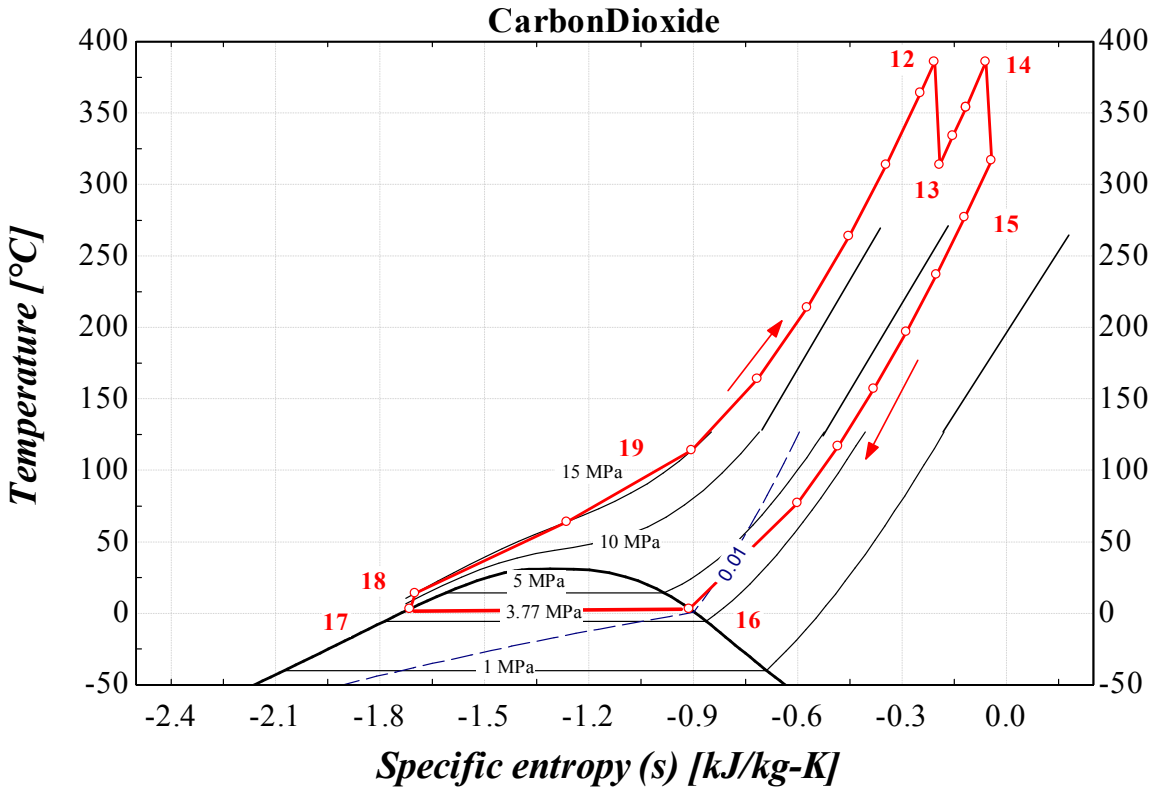

Figure 4.5: T-s diagram of the supercritical carbon dioxide cycle.

After the HTF is utilized for power production in the heater, and the reheater the two steams exit at points 8 and 6 and combine at state 9 with a temperature of 247 °C. This temperature is high enough to drive an absorption cycle whose refrigeration effect will be used for condensing the CO_2 in the Rankine power cycle. Therefore, instead of sending the HTF to the solar field, it is used in the ARS desorber where an ammonia/water mixture is heated. The ammonia evaporates to the rectifier in which buffers are used to condense the water droplets associated with the ammonia vapor. The ammonia vapor is expected to leave the rectifier with a high quality to reach the condenser inlet at state 29. The ammonia vapor is then condensed and assumed to reach state 30 in a liquid phase. Before sending the ammonia refrigerant to an expansion valve, it is used to preheat the stream coming from the evaporator state 33 in heater exchanger (HEX-2). Following this, the refrigerant is allowed to expand through the expansion

valve, where its pressure drops from state 31 to state 32. In the evaporator, the refrigerant evaporates carrying out the heat load while the CO_2 (on the other side of the evaporator heat exchanger) is cooled and subsequently condensed, as illustrated in Fig. 4.6. The refrigerant returns through the heat exchanger (HEX-2) to the absorber.

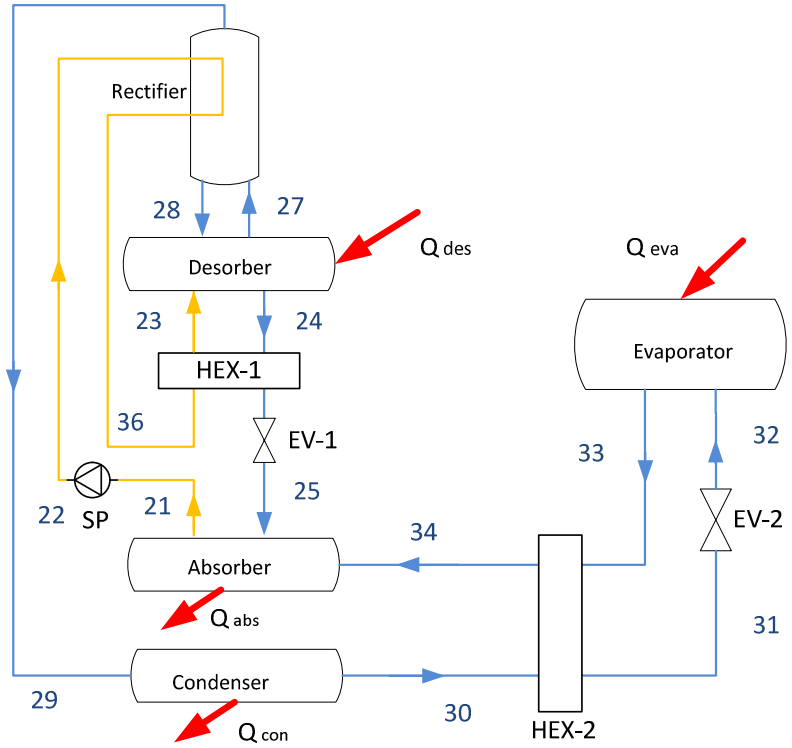

Figure 4.6: Schematic representation of the ammonia/water absorption system.

Chapter 5: Thermodynamic Analysis

In this chapter, the thermodynamic analysis approach is described including the simplification and assumptions, methodology and mathematical model. The objective of undertaken this analysis task is to examine the performance of the proposed integrated systems under different operating conditions. Therefore, the mass, energy and exergy balance equation have been written or each component and subsequently the energy losses, exergy destruction and the energy and exergy efficiencies are evaluated.

The general forms of the mass, energy and exergy balance equations over a control volume, inclosing involved component, are presented, under a steady state condition with neglected potential and kinetic energy changes, in the following

$$\sum \dot{m}_i = \sum \dot{m}_e \tag{5.1}$$

$$\dot{Q} - \dot{W} = \sum \dot{m}_e h_e - \sum \dot{m}_i h_i \tag{5.2}$$

$$\dot{E}x_Q - \dot{W} = \sum \dot{m}_e ex_e - \sum \dot{m}_i ex_i + \dot{E}x_D \tag{5.3}$$

where $\dot{\mathrm{E}}\mathrm{x}_Q$ represents the net exergy transfer associated with the heat $\dot{\mathrm{Q}}$ transferred to / from the component at temperature T, which is calculated as

$$\dot{E}x_Q = \sum (1 - T_a/T)\, \dot{Q} \tag{5.4}$$

The specific exergy at point k is given by

$$ex_k = h_k - h_a - T_a(s_k - s_a) \tag{5.5}$$

and $\dot{\mathrm{E}}\mathrm{x}_k$ is the exergy rate at point k given by

$$\dot{\mathrm{E}}\mathrm{x}_k = \dot{m}\, ex_k = \dot{m}\, [h_k - h_a - T_a(s_k - s_a)] \tag{5.6}$$

In order to analyze the present integrated system, mass, energy and exergy balance equations are

5. 1 PTC Solar Field

The analysis of the PTC solar field is conducted energetically for the entire solar field including the heat transfer analysis and the optical analysis of the receiver. Following this an exergy analysis has been performed. The detailed approach and model are presented in the following sections:

5. 1. 1 Energy Analysis

The balance equation for the mass flow entering and leaving the solar field, (mass flow of HTF circulating through PTC), can be written as

$$\dot{m}_1 = \dot{m}_2 \tag{5.7}$$

Then, the energy balance equation is written as

$$\dot{Q}_o + \dot{m}_1 h_1 + \dot{W}_{CP} = \dot{m}_2 h_2 + \dot{Q}_{Lt} \tag{5.8}$$

where $\dot{Q}_o$ is the total solar radiation, incident on the field area at zero incident angle, and can be evaluated as

$$\dot{Q}_o = I_b \, A_{sf} \tag{5.9}$$

Here, I_b is the beam solar radiation in (W/m^2). A_{sf} is the total solar field area in (m^2). $\dot{m}_1 h_1$, $\dot{m}_2 h_2$ represents the energy rate flowing in to and out of the field, accordingly the net rate can be written using equation (5.7) as

$$\dot{Q}_{ut} = \dot{m}_1 (h_2 - h_1) \cong \dot{m}_1 Cp_{av} \, (T_2 - T_1) \tag{5.10}$$

where Cp_{av} is the average specific heat given as

$$Cp_{av} = (Cp_{\,2} + Cp_{\,1})/2 \tag{5.11}$$

Here, T_1 and T_2 are the temperatures of HTF entering and leaving the solar field. $\dot{Q}_{Lt}$ is the total heat losses rate, (kW), from the PTC field, which includes the all forms of heat losses for HCEs and piping system.

5. 1. 2 PTC Heat Losses

In order evaluation $\dot{Q}_L$ for the entire PTC field, energy balance and heat transfer analysis must be conducted for each of the HCEs. The heat transfer analysis approach presented by Duffie and Beckman, (2006) for PTC is adapted. Fig. 5.1 illustrates the one dimensional heat transfer model for the heat losses from a receiver with an evacuated annulus.

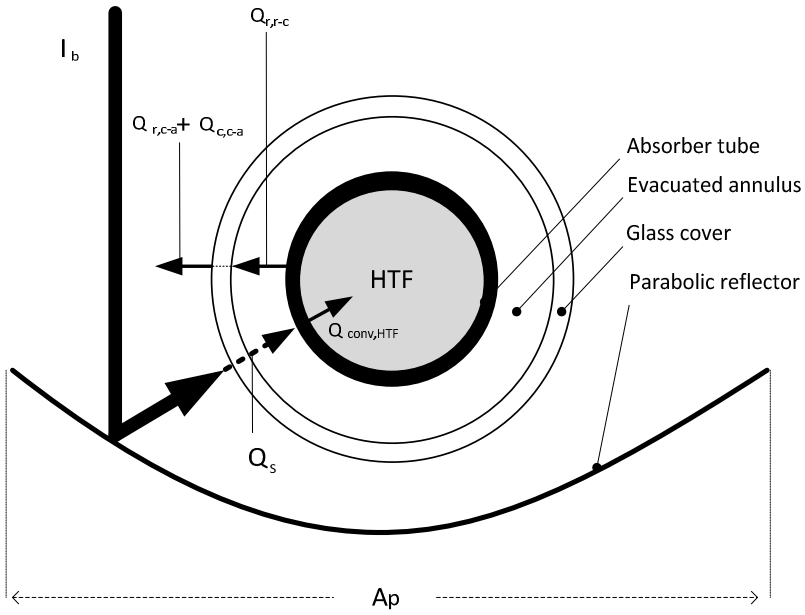

Figure 5.1: One dimensional schematic representation of the heat transfer to and from HCE.

The energy balance equation for a HCE can be written as

$$\dot{Q}_u = \dot{Q}_s - \dot{Q}_l \tag{5.12}$$

where $\dot{Q}_s$ is the concentrated beam radiation absorbed by the absorber (W). It is given as

$$\dot{Q}_s = I_b \, A_p \, \eta_o K \tag{5.13}$$

where η_o is the optical efficiency and it is given by

$$\eta_o = \rho_o \, \tau_o \, \alpha_o \, \gamma_o \left[\left(1 - A_f \tan\theta\right) \cos\theta\right] \tag{5.14}$$

where ρ_o is reflectance of mirror, τ_o is transmittance of the glass cover, α_o is reflectance of mirror, γ_o is intercept factor, A_f is geometric factor and it is denied as

$$A_f = \frac{A_{loss\ area}}{A_{aperture}} \tag{5.15}$$

Here, A_p is the collector aperture area, m^2 and K is the incidence angle modifier which is evaluated as suggested by Dudley (1994) as

$$K = \cos\theta + 0.000884(\theta) - 0.0000537(\theta^2) \tag{5.16}$$

where θ is the incident angle, degrees. $\dot{Q}_l$ can be written in in terms of temperature difference a cross the absorber-vacuum-cover composite wall using loss coefficient, U_l, and the as follows:

$$\dot{Q}_l = A_r\ U_l\ (T_r - T_a) \tag{5.17}$$

Therefore, U_l is evaluated based on the receiver area A_r as

$$U_l = \left[\frac{A_r}{(h_w + h_{r,c-a})A_c} + \frac{1}{h_{r,r-c}}\right]^{-1} \tag{5.18}$$

where h_w is the convective heat transfer to ambient due to wind, $(W/m^2.C)$. For evaluation of h_w, the following correlation are used based on flow nature (Reynolds number):

For (0.1 < Re < 1000)

$$Nu = 0.4 + 0.54\ (Re)^{0.52} \tag{5.19}$$

For (1000 < Re < 50,000)

$$Nu = 0.3\ (Re)^{0.6} \tag{5.20}$$

Here, $h_{r,c-a}$ is the normalized radiation coefficient from glass cover to ambient (W/m^2K). This coefficient can estimated as

$$h_{r,c-a} = 4\,\sigma\,\varepsilon_c\,{T_{sky}}^3 \tag{5.21}$$

where the sky temperature is evaluated, according to Forristall (2003), as

$$T_{sky} = T_a - 8 \tag{5.22}$$

Here, $h_{r,r-c}$ is the normalized radiation coefficient from receiver to glass cover

$$h_{r,c-c} = \frac{\sigma\ ({T_r}^2 + {T_c}^2)(T_r + T_c)}{\frac{1}{\varepsilon_r} + \frac{\mathrm{A}_r}{\mathrm{A}_c}\left(\frac{1}{\varepsilon_c} - 1\right)} \tag{5.23}$$

In this approach the radiation absorbed by the glass cover is assumed to be negligible, and its temperature T_c is estimated (relatively closer to the ambient temperature).

Next, the estimated value of T_c can be validated by solving the following equation, for T_c, iteratively.

$$\mathrm{A}_c(h_w + h_{r,c-a})(T_c + T_a) = \mathrm{A}_r\,h_{r,r-a}(\mathrm{T}_r - \mathrm{T}_c) \tag{5.24}$$

The overall heat transfer coefficient, U_o , is then, evaluated as

$$U_o = \left[\frac{1}{U_L} + \frac{D_o}{h_{htf}\,D_i} + \frac{D_o\,ln(D_o/D_i)}{2k}\right]^{-1} \tag{5.25}$$

where D_o is the receiver outside diameter, (m), and D_i is the receiver inside diameter, (m). Also, h_{htf} is the internal convective heat transfer coefficient, (W/m^2K). This coefficient can be evaluated based on the flow regime (turbulent or laminar). For turbulent flow (Re > 2300) the following equation can be used:

$$Nu = 0.023(Re)^{0.8}(Pr)^{0.4} \tag{5.26}$$

where Re is Reynolds number and given by

$$Re = \frac{\rho V D_i}{\mu} \tag{5.27}$$

And Pr is the Prandtl number and given by

$$Pr = \frac{c_p \mu}{k_{htf}} \tag{5.28}$$

Here, μ is the heat transfer fluid viscosity (*kg/m-s*), and k_{htf} is the heat transfer fluid thermal conductivity (*W/m-K*). However, if the flow is laminar, then Nusselt number can be taken as constant

$$Nu = 4.364 \tag{5.29}$$

Now, the previous equation (5.12) obtained form an energy balance over the receiver can be rewritten in terms of U_L as

$$\dot{Q}_u = \dot{Q}_s - A_r\, U_l\, (T_r - T_a) \tag{5.30}$$

This equation determines the useful heat gain in terms of receiver local temperature T_r, however, for convenience it can be written in terms of heat transfer fluid temperature T_i , by defining collector efficiency factor F', and heat removal factor F_R, as follows:

$$F' = \frac{1/U_L}{\frac{1}{U_l} + \frac{D_o}{h_{htf}\, D_i} + \left(\frac{D_o}{2k}\, ln \frac{D_o}{D_i}\right)} = \frac{U_o}{U_L} \tag{5.31}$$

and

$$F_R = \frac{\dot{m}_{htf}\, c_p}{A_r\, U_L}\left[1 - exp\left(-\frac{U_L\, F'\, A_r}{\dot{m}_{htf}\, c_p}\right)\right] \tag{5.32}$$

Thus, $\dot{Q}_u$ can be written as

$$\dot{Q}_u = F_R[\dot{Q}_s - A_r\, U_l\, (T_i - T_a)] \tag{5.33}$$

The energy efficiency of PTC solar field can be calculated as

$$\eta_{en,PTC} = \frac{\dot{Q}_u}{I_b\ A_p} \tag{5.34}$$

5. 1. 3 Circulating Pump Power

The power required for the HTF circulating pump $\dot{W}_{CP}$ is calculated as

$$\dot{W}_{CP} = \frac{\dot{V}_{htf}\ \Delta P}{\eta_p} \tag{5.35}$$

where η_p is the HTF circulating pump isentropic efficiency, and $\dot{V}_{\text{htf}}$ is the volumetric flow rate of the HTF through the PTC loop, and calculated as

$$\dot{V}_{htf} = \frac{\dot{m}_{htf}}{\rho_{htf}} \tag{5.36}$$

Here, ΔP is the total pressure drop through the PTC loop. For turbulent flow the following equation used to determine ΔP (Munson et al. 1990).

$$\Delta P = \frac{f\ \Delta L_r\ \left(\frac{\dot{m}_{htf}}{A_{cs}}\right)^2}{2\ D_i\ \rho_{htf}} \tag{5.37}$$

where e_f is the roughness of the internal tube surface, (m), and f is the-dimensionless-friction factor and given by (Bergman & Incropera, 2011) as

$$\sqrt{f} = \frac{1}{-2\log\left[\frac{(e_f/D_i)}{3.7} + \frac{2.51}{Re\ \sqrt{f}}\right]} \tag{5.38}$$

In the case of laminar flow, f is calculated as

$$f = \frac{64}{Re} \tag{5.39}$$

5. 1. 4 Solar Field Area Evaluation

The area required for the solar field is evaluated based on the knowledge of the power block performance (energy efficiency)

$$A_{SF} = SM \;\; A_{p,t} \tag{5.40}$$

where A_{SF} is the solar field area, (m^2), SM is the solar multiple, and $A_{p,t}$ is the total aperture area, (m^2). The total collector's area is evaluated as (SAM, 2012)

$$A_{p,t} = \frac{\dot{Q}_{th,in}}{I_b \; \eta_o \; K - \left(\frac{\dot{Q}_l}{A_p}\right) - \left(\frac{\dot{Q}_{pip}}{A_p}\right)} \tag{5.41}$$

where $\dot{Q}_{th,in}$ is the design thermal input power to power block, (W), $\left(\frac{\dot{Q}_l}{A_p}\right)$ is the heat losses normalized per square meter of the collector area, (W/m^2), and $\left(\frac{\dot{Q}_{pip}}{A_p}\right)$ is the heat losses from the piping normalized per square meter of collector area, (W/m^2).

5. 1. 5 Exergy Analysis

An exergy analysis is conducted for the parabolic trough solar collector field, following the previous energy losses and heat transfer model, the exergy balance is evaluated on a collector area bases.

The exergy of the solar heat radiation absorbed by the receiver can evaluated according to (Petela, 1964):

$$Ex_s = Q_s \left[1 - \frac{4}{3}\left(\frac{T_a}{T_s}\right) + \frac{1}{3}\left(\frac{T_a}{T_s}\right)^4\right] \tag{5.42}$$

where T_s is the sun temperature, (K), and T_a is the ambient temperature, (K).

Similarly, the exergy rates per collector area due to the heat losses is given as

$$Ex_l = Q_l\left(1 - \frac{T_a}{T_r}\right) \quad (5.43)$$

The net exergy gained form the solar field is calculated as

$$Ex_u = Q_u\left(1 - \frac{T_a}{T_2}\right) \quad (5.44)$$

Therefore, the exergy balance equation can be written for the solar field as

$$Ex_s = Ex_u + Ex_l + Ex_{D,PTC} \quad (5.45)$$

where $Ex_{D,PTC}$ is the exergy consumption rate per PTC.

The exergy efficiency is, then, can be determined for the solar field area as

$$\eta_{ex,PTC} = \frac{Ex_u}{Ex_s} \quad (5.46)$$

The overall system exergetic efficiency is defined as

$$\eta_{ex,overall} = \frac{\dot{W}_{net}}{Ex_s \times A_p} \quad (5.47)$$

5. 2 Thermal Energy Storage (TES)

The TES is modeled according to the three operations mode: charging, storing, and discharging. In the charging mode the solar field is able to produce surplus thermal energy than what is needed for the power cycle operation. In this case the surplus HTF is stored in hot storage. The operation strategy of the plant is set to start charging form (9:00) to (18:00) every day. The system is storing heat simultaneously while charging. The discharging is started (19:00) or (20:00), depending on the season winter or summer, and continues till (8:00) or (9:00) depending on season as well. In the following thermodynamic modeling of the TES processes is presented.

5. 2. 1 Charging Process Energy Analysis

The rate of heat charged into the hot tank during the charging mode is calculated as

$$\dot{Q}_{ch} = \dot{m}_4(t_{ch})\ C_{p_{htf}} T_4 \tag{5.48}$$

and the total heat energy charged to the hot storage can be evaluated as

$$Q_{ch} = M_{st}\ C_{p_{htf}} T_4 \tag{5.49}$$

where M_{st} is the total stored mass and given as

$$M_{st} = \int_0^t \dot{m}_4(t)\ dt_{ch} \tag{5.50}$$

where dt_{ch} is the charging time differential.

The heat loss during the charging period is determined as follows:

$$\dot{Q}_{L.ch} = U_{TES}\ A_{TES}\ (T_{htf} - T_a) \tag{5.51}$$

where U_{TES} is the overall heat transfer coefficient for the hot tank walls (W/m^2-C), and A_{TES} is the surface area of that walls (m^2).

5. 2. 2 Storing Process Energy Analysis

If the total HTF temperature drop, over a storage period of time (dt_{st}), evaluated as $\Delta T_{st}$where

$$\Delta T_{st} = (T_i - T_f) \tag{5.52}$$

The total heat loss during this mode can then be determined as

$$Q_{L.st} = M_{st}\ C_{p_{htf}} \Delta T_{st} \tag{5.53}$$

where T_i is the HTF temperature at the beginning of the storage mode, and T_f is the final HTF temperature at the end of the storing mode.

5. 2. 3 Discharging Process Energy Analysis

The heat discharging rate from the hot tank to the plant is given as

$$\dot{Q}_{dis} = \dot{m}_4\ C_{p_{htf}} T_f \tag{5.54}$$

The total discharged heat energy can be evaluated as

$$Q_{dis} = M_{st}\, C_{p_{htf}} T_f \tag{5.55}$$

where M_{st} is the total stored mass and given as

$$M_{st} = \int_0^t \dot{m}_4(t)\ dt_{dis} \tag{5.56}$$

Here, dt_{dis} is the discharging time differential.

The TES is operating in a cycle operation manner, during which a full cycle is performed daily. An energy balance of a cycle is presented as

$$Q_{ch} = Q_{dis} + Q_{L.st} \tag{5.57}$$

The performance of the TES is given, by the energy efficiency, as

$$\eta_{en,TES} = \frac{Q_{dis}}{Q_{ch}} \tag{5.58}$$

5. 2. 4 Exergy Analysis

The exergy analysis of the TES is performed for the different modes according to the following: An exergy balance is then introduced, over the full cycle, as

$$Ex_{ch} = Ex_{dis} + Ex_{L.st} + Ex_{D,TES} \tag{5.59}$$

The exergetic efficiency is evaluated as

$$\eta_{ex,TES} = \frac{Ex_{dis}}{Ex_{ch}} \tag{5.60}$$

where Ex_{ch} is the total exergy contents charged into the hot TES tank, and calculated as

$$Ex_{ch} = \left(1 - \frac{T_a}{T_5}\right) \times Q_{ch} \tag{5.61}$$

Here, Ex_{dis} is the total exergy content discharged to the plant, and calculated as

$$Ex_{dis} = \left(1 - \frac{T_a}{T_5}\right) \times Q_{dis} \tag{5.62}$$

where $Ex_{L.st}$ is the exergy loss associated with heat loss to the environment as

$$Ex_{L.st} = \left(1 - \frac{T_a}{T_5}\right) \times Q_{L.st} \tag{5.63}$$

5. 3 Reheat S-CO_2 Rankine Power Cycle

The reheat S-CO_2 Rankine cycle is mathematically modeled and all the required mass, energy, and exergy equation and assumptions are presented in the following:

5. 3. 1 Energy Analysis

The thermal energy delivered by the HTF to the power cycle, is received by two major heat exchangers, the heater and the reheater, and is given for heater by

$$\dot{Q}_{HE} = \dot{m}_{CO2}(h_{12} - h_{19}) \tag{5.64}$$

and for reheater by

$$\dot{Q}_{RE} = \dot{m}_{CO2}(h_{14} - h_{13}) \tag{5.65}$$

The turbines work output is evaluated for the HPT as

$$\dot{W}_{HPT} = \dot{m}_{CO2}(h_{12} - h_{13}) \tag{5.66}$$

and for the LPT as

$$\dot{W}_{LPT} = \dot{m}_{CO2}(h_{14} - h_{15}) \tag{5.67}$$

The heat exchange rate through the internal heat exchanger is calculated as

$$\dot{m}_{CO2}(h_{15} - h_{16}) = \dot{m}_{CO2}(h_{19} - h_{18}) \tag{5.68}$$

The heat rejected to the cooling system through the condensation process is given by

$$\dot{Q}_{CON} = \dot{m}_{CO2}(h_{16} - h_{17}) \tag{5.69}$$

The work required for pumping the working fluid from the condensation pressure to the heater pressure is calculated as

$$\dot{W}_{CO2} = \dot{m}_{CO2}(h_{18} - h_{17}) \tag{5.70}$$

The energy efficiency of the cycle is given by

$$\eta_{en,CO2} = \frac{\dot{W}_{net}}{(\dot{Q}_{HE} + \dot{Q}_{RE})} \tag{5.71}$$

5. 3. 2 Exergy Analysis

The exergy content is evaluated at each state point of the cycle according to the following

$$\dot{E}x_i = \dot{m}_i[(h_i - h_a) - T_a(s_i - s_a)] \tag{5.72}$$

Then, the exergy balance equations are written for the different components of the power cycle. The exergy of the thermal energy supplied to the cycle is evaluated for the heater as

$$\dot{E}x_{HE} = \left(1 - \frac{T_a}{T_7}\right) \times \dot{Q}_{HE} \tag{5.73}$$

and for the reheater as

$$\dot{E}x_{RE} = \left(1 - \frac{T_a}{T_5}\right) \times \dot{Q}_{RE} \tag{5.74}$$

Similarly, the exergy of the heat rejected though the condenser is given as

$$\dot{E}x_{CON} = \left(1 - \frac{T_a}{T_{33}}\right) \times \dot{Q}_{CON} \tag{5.75}$$

The exergy efficiency of the cycle is defined as

$$\eta_{ex,CO2} = \frac{\dot{W}_{net}}{\left[(\dot{Q}_{HE} + \dot{Q}_{RE}) \times \left(1 - \frac{T_a}{T_5}\right)\right]} \tag{5.76}$$

In order to obtain the exergy destruction rate per each component as exergy balance equations must be written for the component in question.

Exergy balance equation over the heater is written as

$$\dot{E}x_5 + \dot{E}x_{13} = \dot{E}x_{14} + \dot{E}x_6 + \dot{E}x_{D,HE} \tag{5.77}$$

And for the reheater as

$$\dot{E}x_7 + \dot{E}x_{19} = \dot{E}x_{12} + \dot{E}x_8 + \dot{E}x_{D,RE} \tag{5.78}$$

The exergy balance for the HPT given by

$$\dot{E}x_{12} = \dot{E}x_{13} + \dot{W}_{HPT} + \dot{E}x_{D,HPT} \tag{5.79}$$

and for the LPT given by

$$\dot{E}x_{14} = \dot{E}x_{15} + \dot{W}_{LPT} + \dot{E}x_{D,LPT} \tag{5.80}$$

The exergy balance over the IHE is written as

$$\dot{E}x_{15} + \dot{E}x_{18} = \dot{E}x_{19} + \dot{E}x_{16} + \dot{E}x_{D,IHE} \tag{5.81}$$

The exergy balance pump given by

$$\dot{E}x_{17} + \dot{W}_P = \dot{E}x_{18} + \dot{E}x_{D,P} \tag{5.82}$$

Finally, for the condenser

$$\dot{E}x_{16} + \dot{E}x_{32} = \dot{E}x_{17} + \dot{E}x_{33} + \dot{E}x_{D,CON} \tag{5.83}$$

By solving the above equations simultaneously, the exergy destruction rate per each cycle component is identified and the exergy efficiency of the cycle evaluated.

5. 4 Absorption Refrigeration System

Energy and exergy analysis conducted of the ammonia/ water absorption cycle, in which mass, concentration, energy, and exergy balance equations have been written for each component of this cycle. In the following these equations are presented, some (mass and concentration) trivial equations are omitted, to avoid unnecessary redundancy.

5. 4. 1 Assumptions and Approximations

For the analysis to be carried out a number of assumptions are made to facilitate the modeling. These assumptions are listed as follows:

- The condenser and absorber operating temperature is 35 ^{0}C.
- The evaporator at operate at -5 ^{0}C.
- The state points 28, 21, 30 and 24, according to the numbering system shown in Fig.4.1, are taken as saturation liquid states.
- The points 33, 29 and 27 are taken as saturation vapor states.
- The refrigerant concentration at state point 29 is set as 0.99
- The heat exchangers effectiveness is defined as

$$\varepsilon = \frac{\dot{Q}_c}{\dot{Q}_h} = 97\%$$

where $\dot{Q}_h$ is the hot stream utility, and $\dot{Q}_c$ is the cold stream utility.

- The solution pump efficiency is taken as 65%.

5. 4. 2 Energy and Exergy Analyses

Energy and exergy analyses conducted of the ammonia/ water absorption cycle, in which mass, concentration, energy, and exergy balance equations are written for each component of this cycle. In the following these equations are presented, some (mass and concentration) trivial equations are omitted, to avoid unnecessary redundancy.

Desorber:

$$\dot{m}_{23} + \dot{m}_{28} = \dot{m}_{27} + \dot{m}_{24} \tag{5.84}$$

$$\dot{m}_{23}\, x_{23} + \dot{m}_{28}\, x_{28} = \dot{m}_{27} x_{27} + \dot{m}_{24}\, x_{24} \tag{5.85}$$

$$\dot{Q}_{des} + \dot{m}_{23}\, h_{23} + \dot{m}_{28}\, h_{28} = \dot{m}_{27} h_{27} + \dot{m}_{24}\, h_{24} \tag{5.86}$$

$$\dot{E}x_{des} = \dot{Q}_{des} \left(1 - \frac{T_a}{T_{des}}\right) \tag{5.87}$$

$$\dot{E}x_{des} + \dot{m}_{23}\, ex_{23} + \dot{m}_{28}\, ex_{28} = \dot{m}_{27} ex_{27} + \dot{m}_{24}\, ex_{24} + \dot{E}x_{des,D} \tag{5.88}$$

Condenser:

$$\dot{m}_{29} = \dot{m}_{30} \tag{5.89}$$

$$\dot{Q}_{con} + \dot{m}_{30}\, h_{30} = \dot{m}_{29}\, h_{29} \tag{5.90}$$

$$\dot{E}x_{con} = \dot{Q}_{con} \left(1 - \frac{T_a}{T_{con}}\right) \tag{5.91}$$

$$\dot{E}x_{con} + \dot{E}x_{30} = \dot{E}x_{29} + \dot{E}x_{con,D} \tag{5.92}$$

Absorber:

$$\dot{m}_{34} + \dot{m}_{26} = \dot{m}_{21} \tag{5.93}$$

$$\dot{m}_{34}\, x_{34} + \dot{m}_{26}\, x_{26} = \dot{m}_{21} x_{21} \tag{5.94}$$

$$\dot{Q}_{abs} + \dot{m}_{21}\, h_{21} = \dot{m}_{26}\, h_{26} \tag{5.95}$$

$$\dot{E}x_{abs} = \dot{Q}_{abs} \left(1 - \frac{T_a}{T_{abs}}\right) \tag{5.96}$$

$$\dot{E}x_{abs} + \dot{E}x_{21} = \dot{E}x_{26} + \dot{E}x_{abs,D} \tag{5.97}$$

Rectifier:

$$\dot{m}_{27} = \dot{m}_{28} + \dot{m}_{29} \tag{5.98}$$

$$\dot{m}_{27}\, x_{27} = \dot{m}_{28}\, x_{28} + \dot{m}_{29} x_{29} \tag{5.99}$$

$$\dot{Q}_{rec} + \dot{m}_{29}\, h_{29} + \dot{m}_{28}\, h_{28} = \dot{m}_{27} h_{27} \tag{5.100}$$

$$\dot{Q}_{rec} = \dot{m}_{22}(h_{39} - h_{22}) \tag{5.101}$$

$$\dot{E}x_{rec} = \dot{Q}_{rec} \left(1 - \frac{T_a}{T_{rec}}\right) \tag{5.102}$$

$$\dot{E}x_{27} = \dot{E}x_{rec} + \dot{E}x_{28} + \dot{E}x_{29} + \dot{E}x_{D,rec} \tag{5.103}$$

Heat exchanger 1:

$$\dot{m}_{36} = \dot{m}_{23} \quad ; \quad \dot{m}_{24} = \dot{m}_{25} \tag{5.104}$$

$$\dot{m}_{36}\, h_{36} + \dot{m}_{24}\, h_{24} = \dot{m}_{25}\, h_{25} + \dot{m}_{23}\, h_{23} \tag{5.105}$$

$$\dot{E}x_{36} + \dot{E}x_{24} = \dot{E}x_{25} + \dot{E}x_{23} + \dot{E}x_{HEX-1,D} \tag{5.106}$$

Heat exchanger 2:

$$\dot{m}_{30} = \dot{m}_{31} \quad ; \quad \dot{m}_{33} = \dot{m}_{34} \tag{5.107}$$

$$\dot{m}_{31}\, h_{31} + \dot{m}_{34}\, h_{34} = \dot{m}_{33}\, h_{33} + \dot{m}_{30}\, h_{30} \tag{5.108}$$

$$\dot{E}x_{31} + \dot{E}x_{34} = \dot{E}x_{33} + \dot{E}x_{30} + \dot{E}x_{HEX-2,D} \quad (5.109)$$

Expansion valve 1:

$$\dot{m}_{25} = \dot{m}_{26} \quad (5.110)$$

$$h_{25} = h_{26} \quad (5.111)$$

$$\dot{E}x_{31} = \dot{E}x_{32} + \dot{E}x_{EV-2,D} \quad (5.112)$$

Expansion valve 2:

$$\dot{m}_{31} = \dot{m}_{32} \quad (5.113)$$

$$h_{25} = h_{26} \quad (5.114)$$

$$\dot{E}x_{31} = \dot{E}x_{32} + \dot{E}x_{EV-1,D} \quad (5.115)$$

Evaporator:

$$\dot{m}_{32} = \dot{m}_{33} \quad (5.116)$$

$$\dot{m}_{32}\, x_{32} = \dot{m}_{33}\, x_{33} \quad (5.117)$$

$$\dot{Q}_{eva} + \dot{m}_{32}\, h_{32} = \dot{m}_{33}\, h_{33} \quad (5.118)$$

$$\dot{Q}_{eva} = \dot{m}_{CO2}\,(h_{16} - h_{17}) \quad (5.119)$$

$$\dot{E}x_{eva} = \dot{Q}_{eva}\left(1 - \frac{T_a}{T_{eva}}\right) \quad (5.120)$$

$$\dot{E}x_{eva} + \dot{E}x_{32} = \dot{E}x_{33} + \dot{E}x_{eva,D} \quad (5.121)$$

Solution Pump:

$$\dot{m}_{22} = \dot{m}_{21} \quad (5.122)$$

$$w_{SP} = \frac{v_{21}\,(P_{22} - P_{21})}{\eta_P} \quad (5.123)$$

$$h_{22} = h_{21} + w_{SP} \quad (5.124)$$

$$\dot{W}_{SP} + \dot{E}x_{21} = \dot{E}x_{22} + \dot{E}x_{SP,D} \tag{5.125}$$

Coefficient of Performance COP:

The cooling system performance is evaluated by the COP_{en} which is defined as

$$COP_{en} = \frac{\dot{Q}_{eva}}{\dot{Q}_{des} + \dot{W}_{SP}} \tag{5.126}$$

The exergy-based COP possible at this operation conditions is given as

$$COP_{ex} = \frac{\dot{E}x_{eva}}{\dot{E}x_{des} + \dot{W}_{SP}} \tag{5.127}$$

Chapter 6: Results and Discussion

In this chapter, the results of the analysis will be presented and discussed. The assumptions and simplifications related to each section will be introduced accordingly.

6. 1 PTC Solar Field

The performance of the PTC solar field is evaluated through an energy and exergy-based parametric study. In this study, the effects of the important design and operating parameters on energy and exergy efficiencies are illustrated. In addition, the heat energy losses and the exergy destruction rate through the PTC solar field are evaluated. The influence of changing some of the important optical and design parameters of PTC on the energy and exergy efficiencies is also considered.

In the present study, the selected location is Al Madinah in Saudi Arabia. The design point parameters are presented in Table 6.1.The direct normal irradiation (DNI), ambient temperature, and wind velocities are obtained from the NREL and KACST website (KACST, 1999).

Table 6.1: Design point parameters for Al Madinah in Saudi Arabia (adapted from KACST, 1999).

Parameter	**Value**
DNI (W/m^2)	800
Longitude (°)	24.55 N
Latitude (°)	39.70 E
Altitude (m)	626
Ambient temperature ($°C$)	25
Time zone ($hour$)	+3

The main assumption and operating condition for PTC for the base case design point are given in Table 6.2. These assumptions include the fixed PTC outlet temperature with varying HTF mass flow rate according to the intensity of the solar radiation intensity, fixed PTC solar field area based on a 1 MW full load output and solar multiple

of 2. The receiver glass cover and receiver temperature are assumed, based on simultaneous solution of the above given equations of heat transfer.

Table 6.2: Main assumption of the PTC.

Main assumptions for PTC	
Field outlet temperature, T_2 (^0C)	395
Field inlet temperature ,T_1 (^0C)	60
Receiver total length, L (*m*)	3800
Wind velocity (*m/s*)	2
Receiver average temperature (^0C)	240
Glass cover average temperature (^0C)	40

The state point properties of the base case are presented in Table 6.3. This table shows the working fluid, mass flow rate, temperature, specific heat and specific exergy and the different PTC state points according to the numbering system illustrated in Fig. 4.2.

Table 6.3: The state points of the HTF cycle.

State point	**Fluid**	$\dot{m}$ (*kg/s*)	C_p (*kJ/kg-K*)	T (^0C)	ex (*kJ/kg*)
0	Therminol-PV1	-	1.559	25	0
1	Therminol-PV1	8.691	1.664	60	3.396
2	Therminol-PV1	8.691	2.611	395	338.1
3	Therminol-PV1	8.691	2.611	390	330.9
4	Therminol-PV1	0	2.611	390	330.9
5	Therminol-PV1	4.156	2.611	390	330.9
6	Therminol-PV1	4.156	2.418	338.1	239.7
7	Therminol-PV1	4.535	2.611	390	330.9
8	Therminol-PV1	4.535	1.896	143.9	35.89
9	Therminol-PV1	8.691	2.157	247.2	121.3
10	Therminol-PV1	8.691	1.664	60	3.396

The effects of the solar beam radiation intensity on the PTC and the overall system performance are shown in the following figures. The energy efficiency of the PTC and heat losses is presented in Fig. 6.1. It can be noticed that the energy efficiency of the PTC is increasing with the increase of the solar radiation. Similarly, the total heat energy loss shows a linear increase with increasing solar beam radiation. The energy efficiency

of the PTC varies between 65% and a maximum of about 68.1% at 1200 (W/m^2). An energy efficiency of above 67.5% at 800 (W/m^2) is achievable.

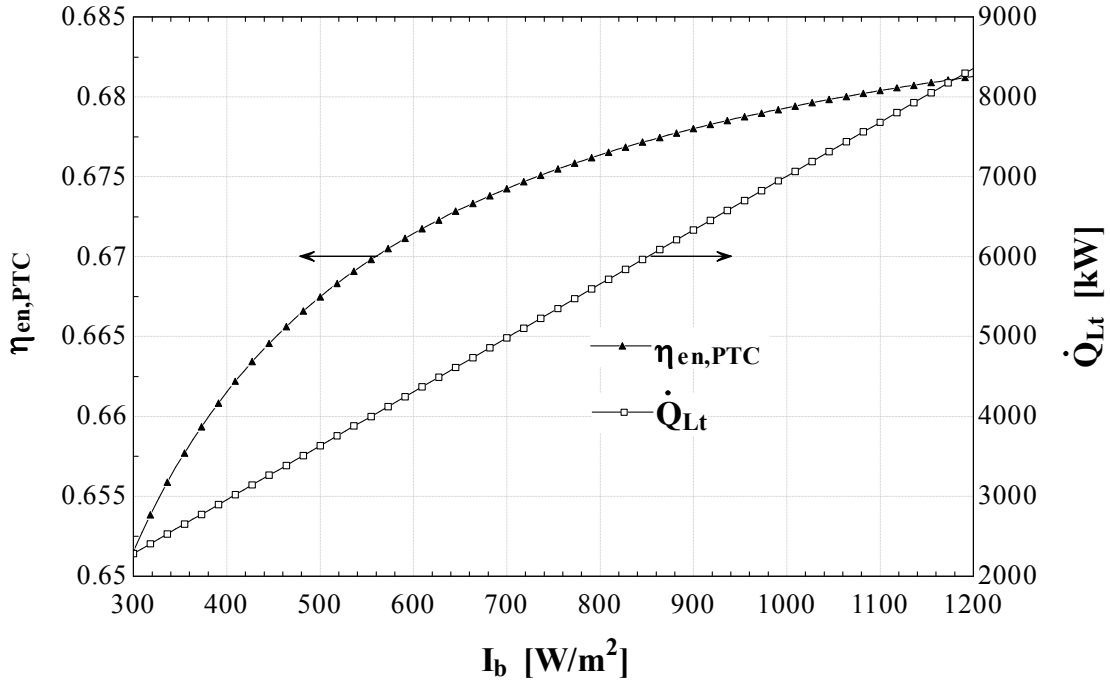

Figure 6.1: The change in the PTC energy efficiency and total solar field heat losses with the change in the solar beam radiation.

In Fig. 6.2, the exergy efficiency of the PTC and the exergy destruction rate within the PTC are evaluated under different solar beam radiation intensity. The exergy efficiency appears to be lower than the energy efficiency. It varies between 36% and 39.5%. The exergy destruction rate linearly increases with increasing solar radiation. It can be noticed that even through the PTC exergy destruction rate increases with the increase in solar beam radiation, the exergy efficiency of the PTC shows higher performance at higher solar radiation.

The variations in the available solar energy and the net heat energy produced by the PTC with the solar beam radiation are shown in Fig. 6.3. Furthermore, the heat energy losses are presented as an optical heat losses and total heat losses. Fig. 6.3 also shows a linear increase of the different heat components (available, net and loses) with the increase in solar radiation intensity. The optical heat losses can be clearly seen as a major part of the energy losses from the PTC solar field.

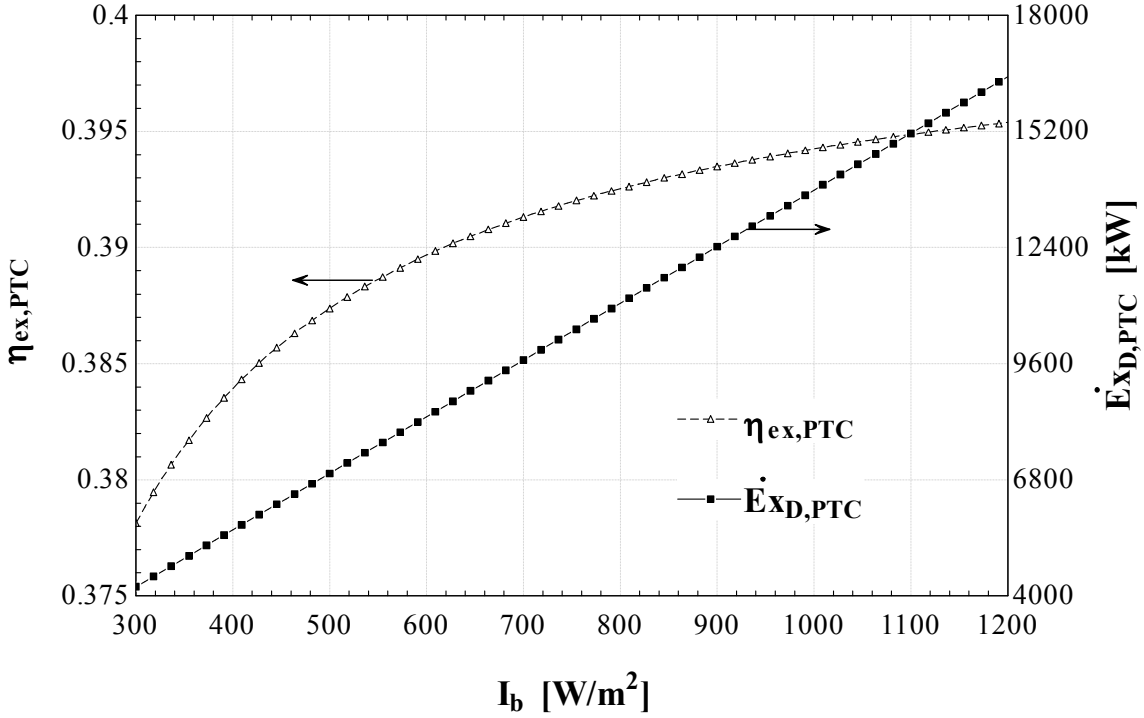

Figure 6.2: The change in the PTC exergy efficiency and solar field exergy destruction rate with the change in the solar beam radiation.

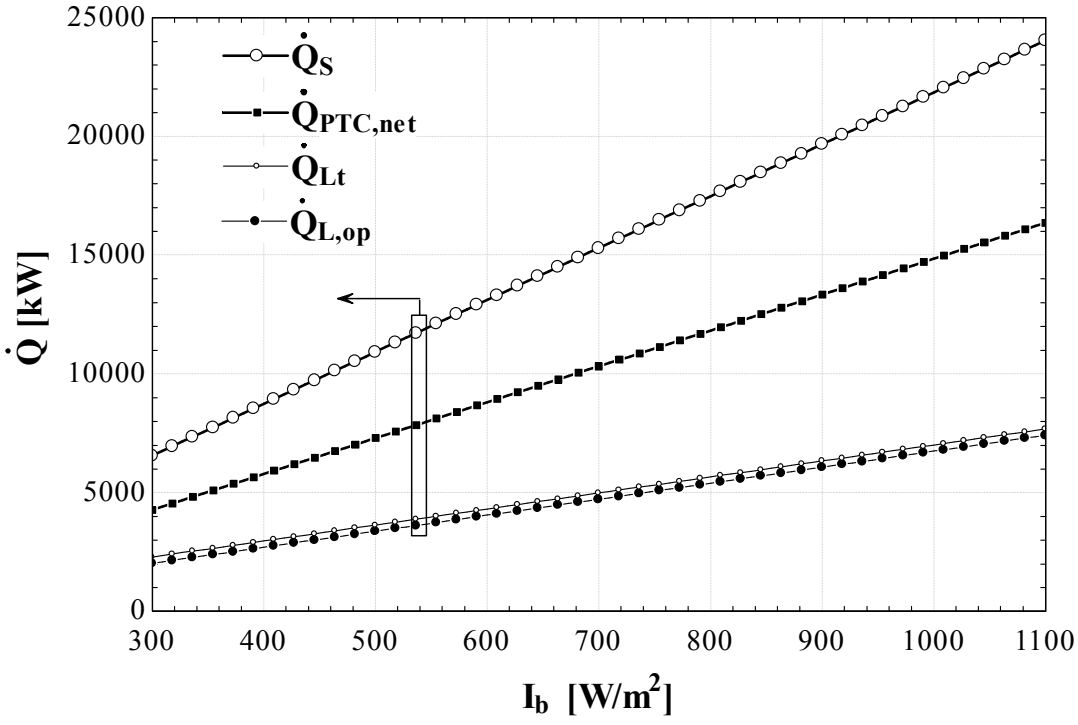

Figure 6.3: The variations in solar heat available and heat losses from the PTC solar field.

The effects of varying solar beam radiation on the overall system's performance are shown in Fig. 6.4, where energy and exergy efficiencies of the overall system are evaluated under a wide range of solar beam radiation intensity. Generally, the system shows better performance at higher solar intensities. The energy efficiency varies from 11.5% at 300 (W/m^2) to 12.1% at 1200 (W/m^2) with an increase of 0.6% over the entire range, while exergy efficiency increases from 12.1% to above 12.6% with about 0.5% increase over the same solar radiation range. It should be noted here that these efficiencies are defined based on net electric power output.

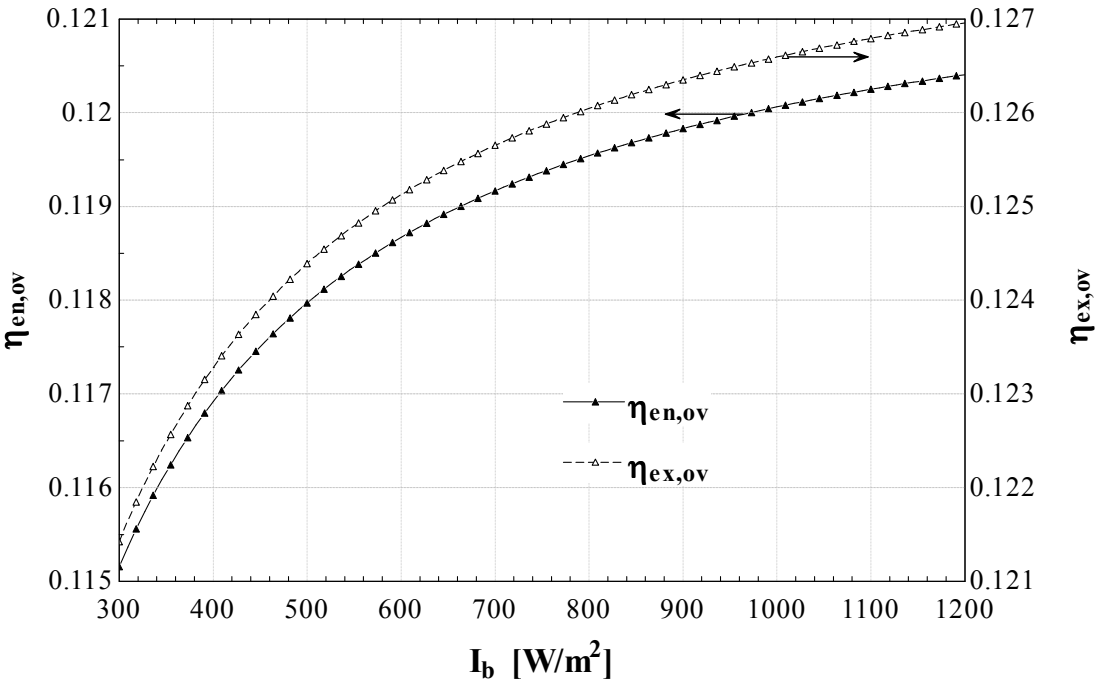

Figure 6.4: The effect of the change in the solar beam radiation on the overall system energy and exergy efficiencies.

In Fig. 6.5, the variations in the exergy destruction rate and total heat energy losses from the PTC are presented with different solar beam radiation intensities. It is noticeable that the heat losses and exergy destruction rate that occurs in the PTC has the same linear proportional trend with the increase in solar radiation intensity. This is because of the dependence of the exergy destruction rate on the heat losses from the PTC since these losses are a major reason for exergy destruction in the PTC. Over the solar radiation intensity range, from 300 to 1100 (W/m^2), the heat losses vary between 2000

and 8000 (*kW*) for the specified PTC area while the associated exergy destruction rate varies between 4000 and 15000 (*kW*).

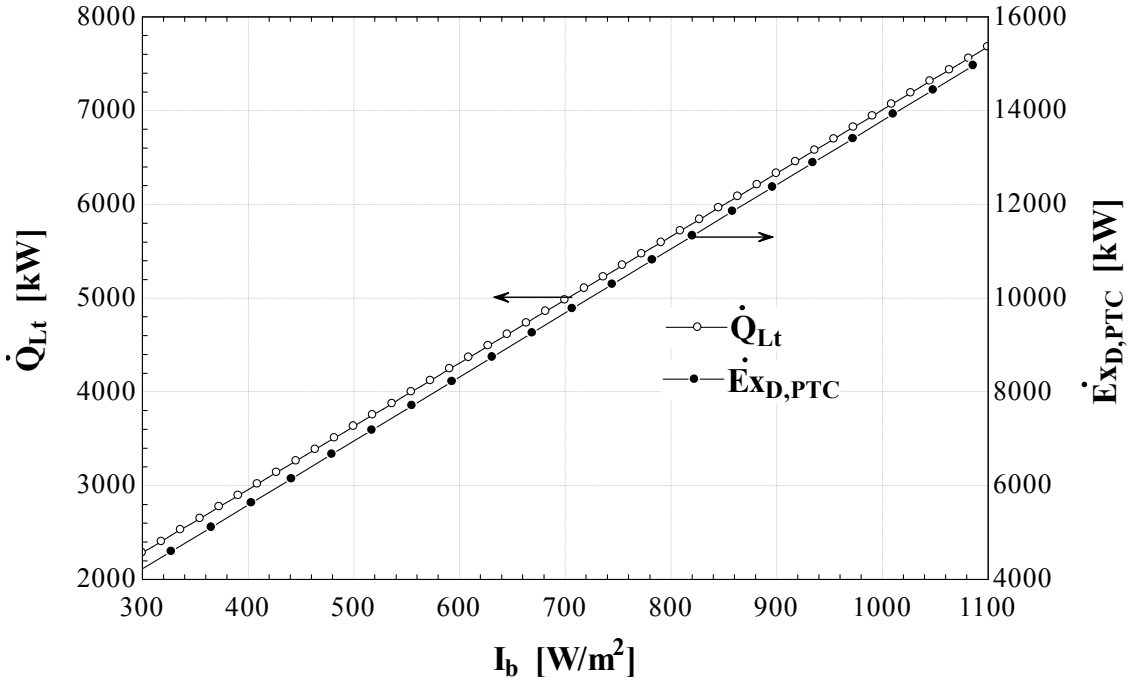

Figure 6.5: The variations in the total heat loss and exergy destruction rate under different solar beam radiation intensities.

The effect of the change in solar radiation intensity on the exergy destruction rate in the different components of the power cycle is shown in Fig. 6.6. The increase in solar radiation will increase the power output from the system. However, the exergy destruction rate in the different cycle components will also increase. The exergy destruction rates in the condenser (CON), heater (HE), reheater (RE), high pressure turbine (HPT) and low pressure turbine (LPT) vary between 30 and 280 (*kW*), while in the internal heat exchanger (IHE) it varies between 300 and 1200 (*kW*). This indicates a significant amount of exergy is destroyed within the IHX and subsequently more effort is needed to improve this element.

In Fig. 6.7 the effects of wind velocity on the energy efficiency of the PTC and the heat losses rate are shown. The wind velocity varies from 0 to 10 (*m/s*) and the changes in heat losses are noticed to sharply increase with wind velocity in the range 0 to 2 (*m/s*), above which the heat losses show slight increase with wind velocity. The PTC energy efficiency curve appears in an inverse shape to the heat losses curve. It sharply

drops with increasing wind velocity from 0 to 2 (*m/s*) with about 0.1%; however, after 2 (*m/s*) it shows a very slight decrease with wind velocity. Fig. 6.7 presents the effect of convection heat losses to the environment and this effect seems to be very limited, mainly because of the vacuum annuals employed in receivers to create a well-insulated absorbing surface from the surrounding environment.

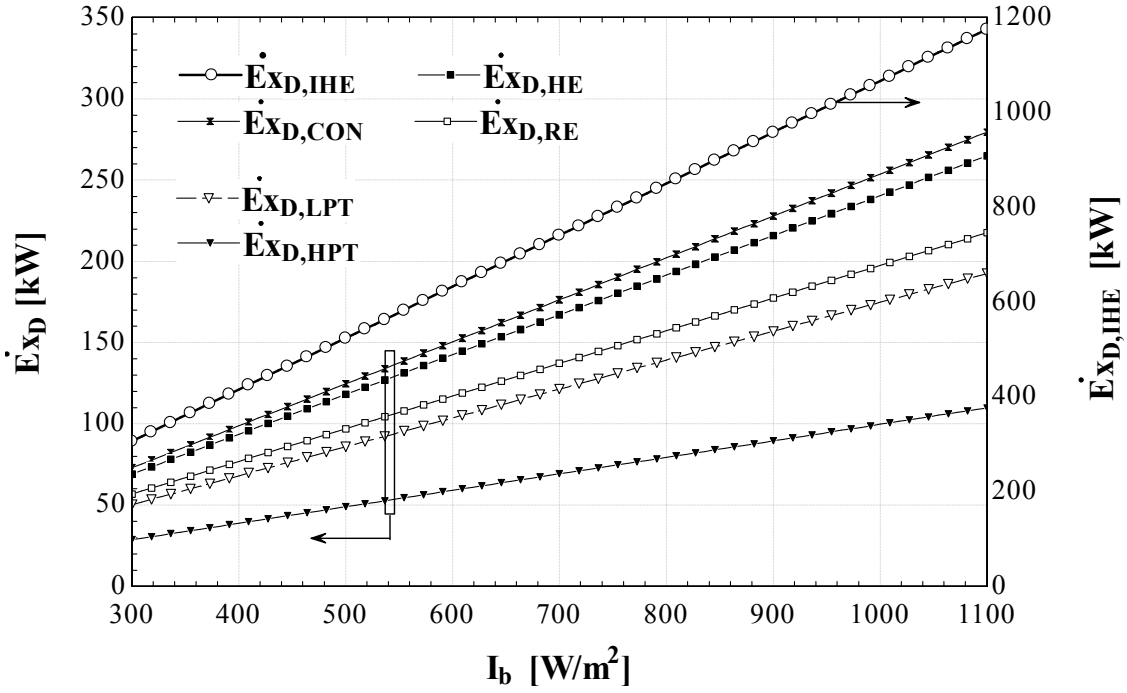

Figure 6.6: The change in the exergy destruction rate per the power cycle components with changing solar beam radiation.

The effect of wind velocity on the exergetic performance of the PTC is presented in Fig. 6.8. The exergy efficiency and the exergy destruction rate of the PTC with wind velocity have trends similar to that of energy efficiency and heat losses as presented earlier in Fig. 6.7.

The PTC exergy destruction rate increases by about 6 (*kW*) with wind velocity increase from 0 to 2 (*m/s*), while it increases by less than 1 (*kW*) with wind velocity from 2 to 10 (*m/s*). The PTC exergy efficiency drops about 0.05% over the entire range

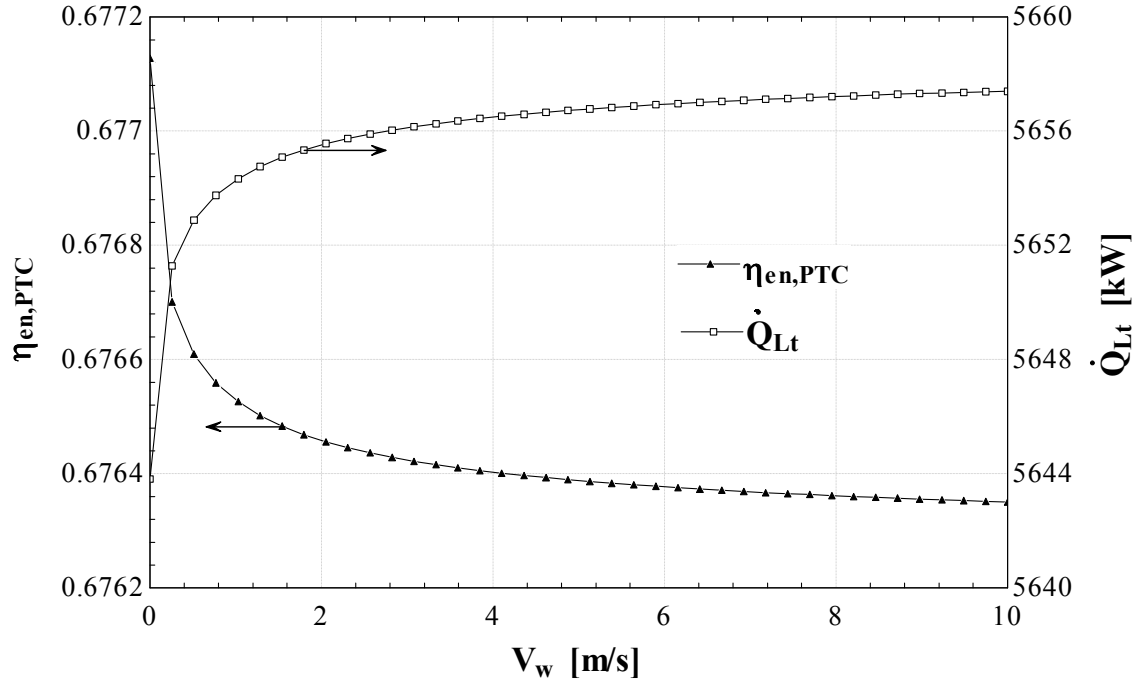

Figure 6.7: The effect of wind velocity on heat losses and energy efficiency of the PTC solar field.

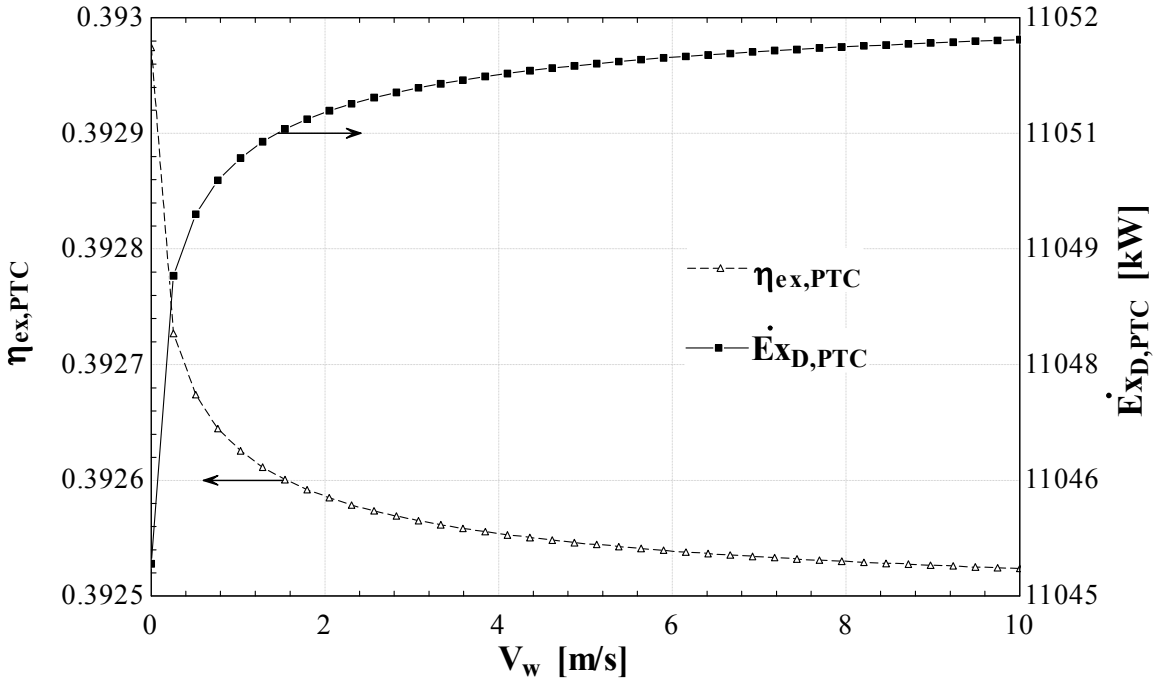

Figure 6.8: The effect of wind velocity on exergy destruction rate in the PTC solar field and the exergy efficiency of the PTC solar field.

.

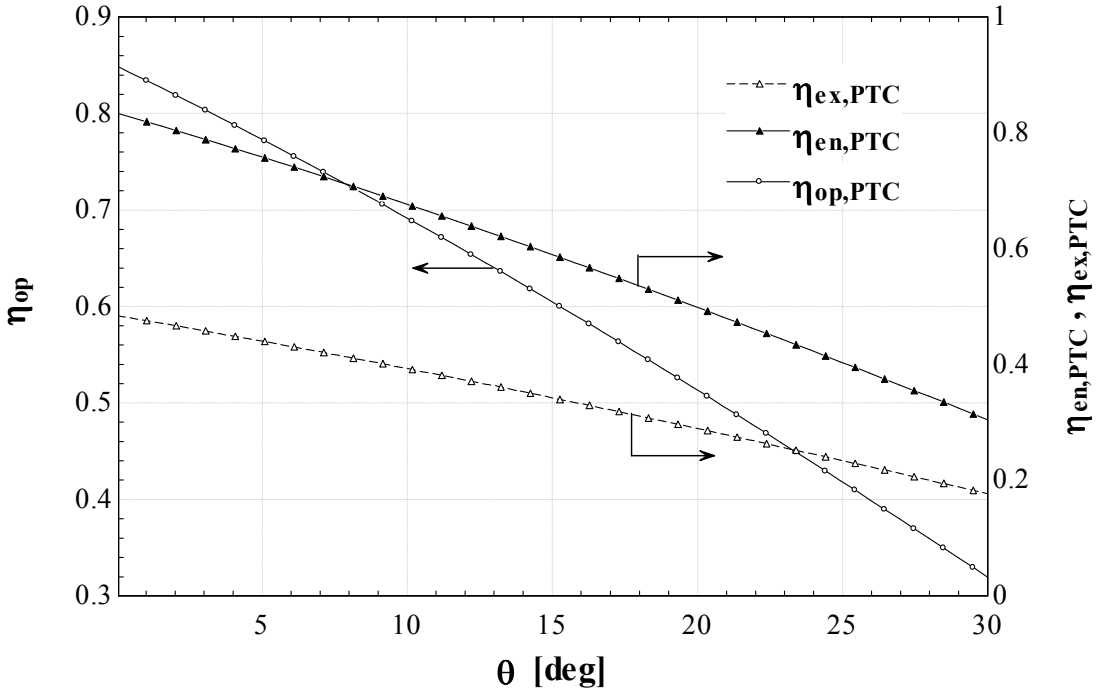

Figure 6.9: The effect of changing solar beam incidence angle on the PTC optical efficiency and subsequently on the PTC energy and exergy efficiencies.

The effects of changing the solar beam radiation incidence angle on the system performance are illustrated in Fig. 6.9. The PTC optical efficiency strongly depends on the incidence angle of the solar beam radiation. Fig. 6.9 shows this relationship and the effect of the changing incidence angle on the PTC optical efficiency and on the PTC energy and exergy efficiencies. It is clearly shown that the lower the incidence angle, the higher the PTC performance. At 0^0 radiation incidence angle, the PTC is predicted to achieve an optical efficiency of 85% which will result in high PTC energy and exergy efficiencies as high as 81% and 50% for energy and exergy efficiencies, respectively. The increase in the incidence angle from 10 to 20^0 will result in a reduction in the optical efficiency of the PTC by about 20%, and subsequently in the PTC energy efficiency by 10% and exergy efficiency by about 7%. Accordingly, the reduction of θ is required for higher PTC performance. The location selection, tracking system and design parameters all need to be adjusted to reduce the incidence angle.

The effects of the varying incidence angle on the overall system performance are illustrated in Fig. 6.10. The overall system energy efficiency can drop by almost 10% if

an error that occurs in the tracking system leads to an increase in the incidence angle from 0 to 30^0. The heat energy losses associated with this error will be about 4377 (*kW*). Similarly, the exergy efficiency would drop by about 9.4 % and with an increase in the exergy destruction rate by about 9350 (*kW*) over the entire range.

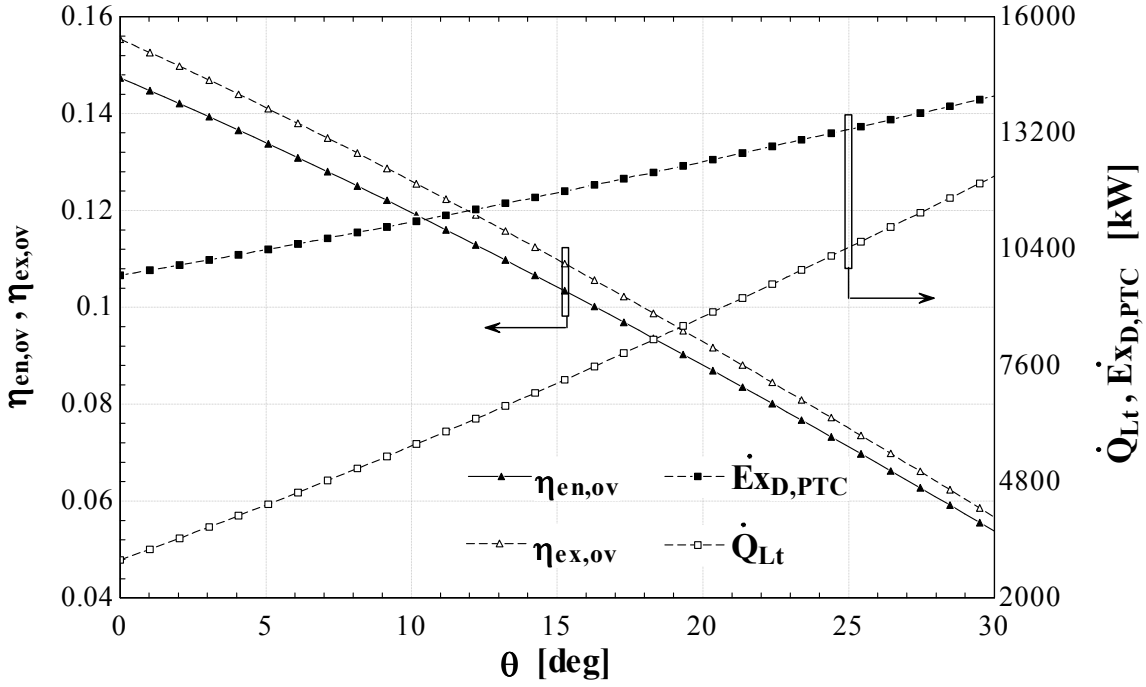

Figure 6.10: The effects of the variation of solar beam incidence angle on the overall energy and exergy efficiencies of the system as well as the associate heat losses and exergy destruction rate through the PTC.

In Fig. 6.11, the effects of the change in the receiver emittance on the PTC performance are shown. The receiver emittance is an important design parameter. Its value is commonly given as a function of the receiver temperature, therefore it is important to assess its change on the energy and exergy performance of the PTC. The increase in the receiver emittance from 0.075 to 0.175 can result in energy efficiency reduction by 1.5% and increase in receiver heat losses by 300 (*kW*). In Fig. 6.12, the effects of receiver emittance on the PTC exergy destruction rate and exergy efficiency are shown. The trend in this figure is similar to the previous energy figure and both convey the same idea that PTC performance is optimum at the lowest possible receiver emittance.

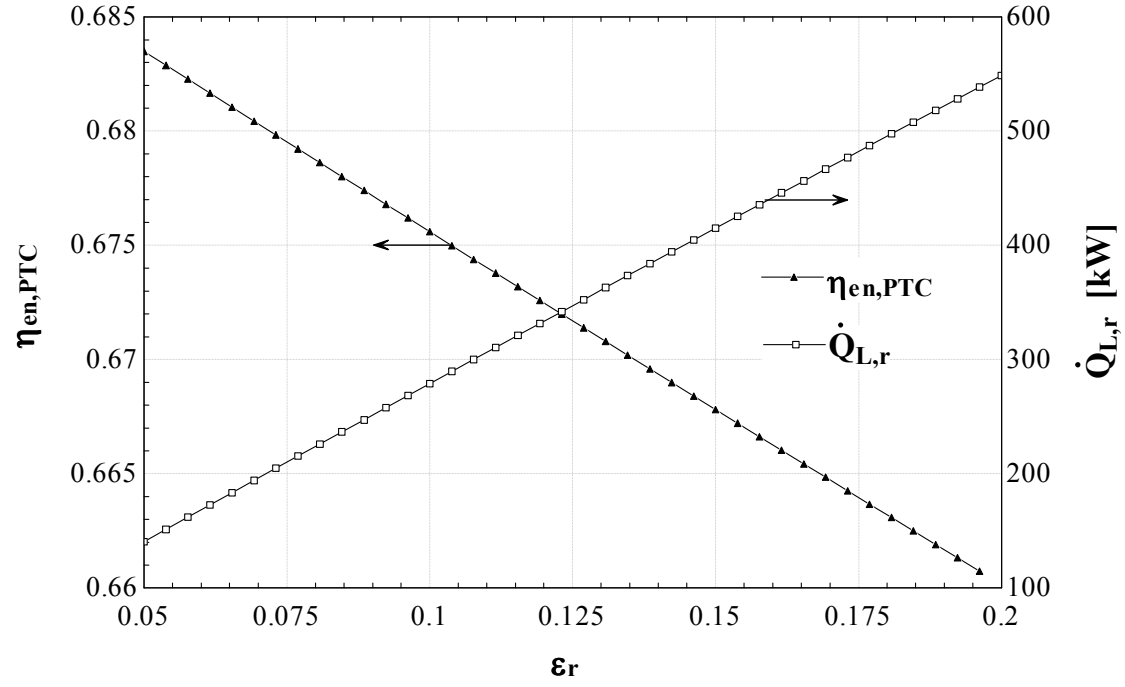

Figure 6.11: The effect of the change in receiver emittance on the PTC energy efficiency and on the heat losses rate from the receiver.

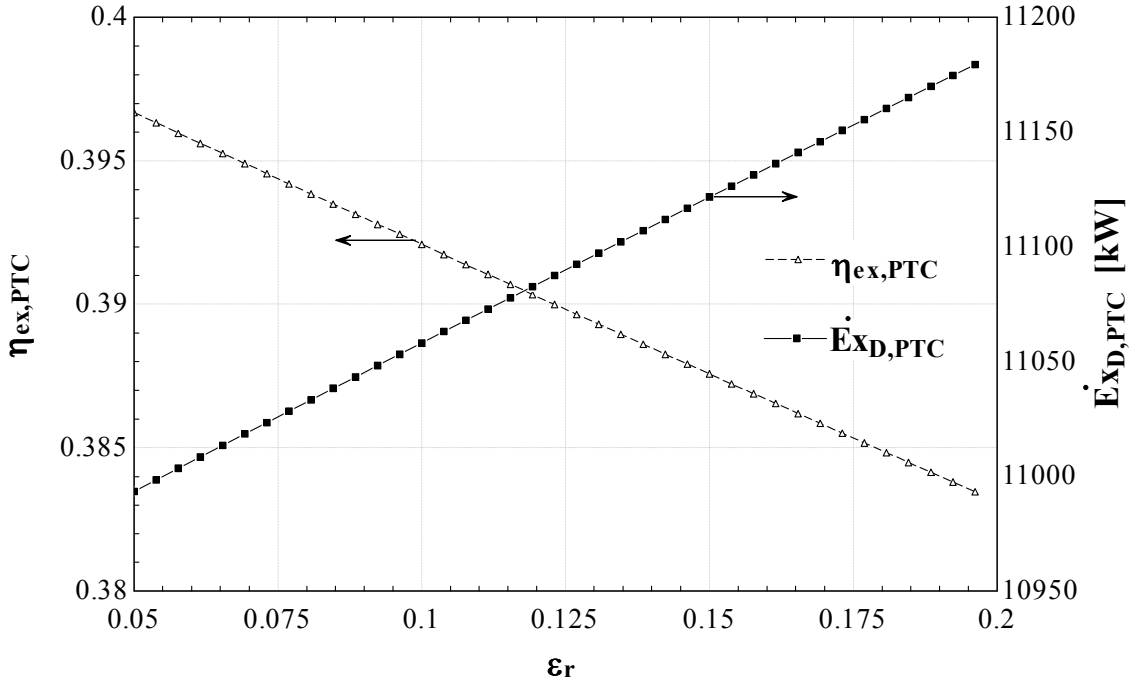

Figure 6.12: The effect of the change in the receiver emittance on the PTC exergy efficiency and the PTC exergy destruction rate.

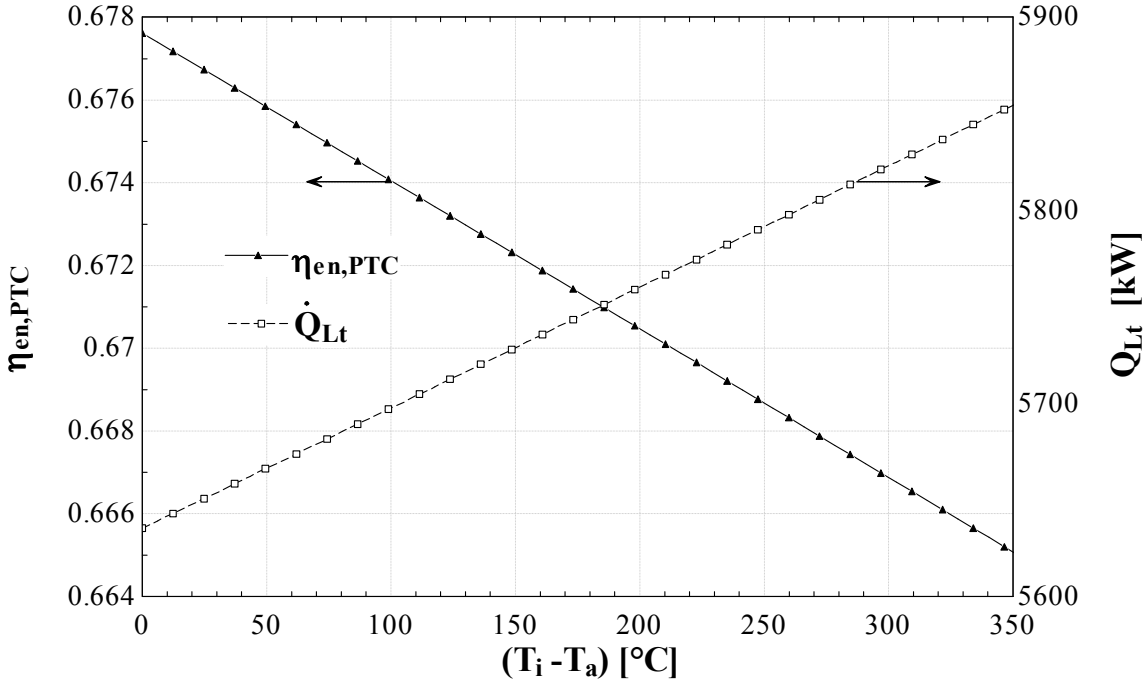

Figure 6.13: The variation in the PTC heat losses and energy efficiency with the variation in PTC inlet temperatures above ambient.

The effects of variation in the PTC operating temperature are examined for energy and exergy efficiencies and for heat losses and exergy destruction rate per PTC. In Fig. 6.13, the solar field inlet temperature above ambient is varied with the energy efficiency and the heat losses from the PTC. The energy efficiency of the PTC linearly declines with increasing solar field inlet temperature; however, the total heat loss from the PTC increases with the increase in the inlet temperature. The operation of the PTC solar field at lower inlet temperature reduces the temperature difference between the HTF and the ambient temperature and subsequently improves the energy efficiency but the challenge associated with such operation is that the reduction in the HTF inlet temperature increases the PTC area required for achieving the desirable outlet temperature. Furthermore, one of the most common types of TES is the two indirect tanks where a molten salt is used to store thermal energy in a sensible heat form where molten salt has a minimum limit of an operation in liquid phase. If HTF temperature drops below this limit the molten salt will encounter solidification. For this reason, the solar field inlet temperature is limited by the TES system operating range.

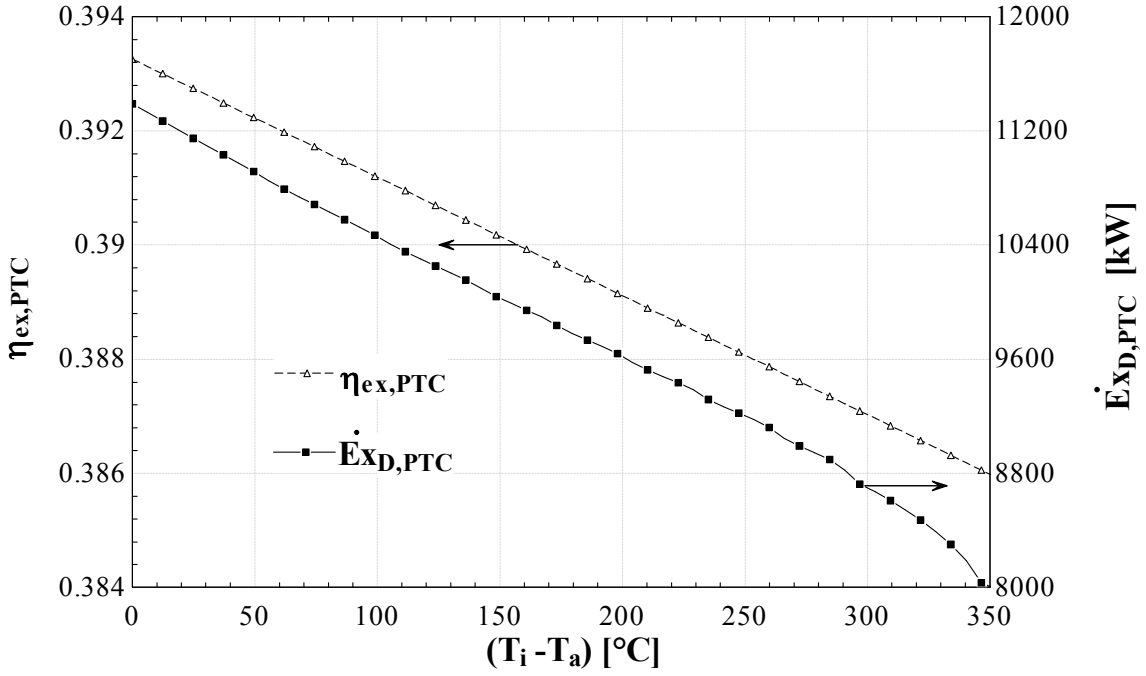

Figure 6.14: The variations in the PTC exergy destruction rate and exergy efficiency with the variation in PTC inlet temperature above ambient.

Fig. 6.14 shows the effects of the variation in the solar field inlet temperature above the ambient on exergy efficiency and exergy destruction rate per PTC. The exergy efficiency of the PTC linearly declines with the increase in the solar field inlet temperature. Also, the exergy destruction rate per PTC follows the same decline trend in spite of the increase of the total heat loss that has been presented in Fig. 6.14. Over the temperature range presented in Fig. 6.14, the exergy efficiency shows an improvement of 0.8% when operating at low temperature (around ambient) and in spite of the high exergy destruction rate that occurs at the lower PTC inlet temperature, exergy wise it is better to operate at a lower PTC inlet temperature.

In Fig. 6.15, the variations in the net PTC exergy output and exergy destruction rate are presented with the variation in the solar field inlet temperature above the ambient. It can be noticed that the net exergy output from the PTC decreases with the increase in the solar field inlet temperature. Likewise, the exergy destruction rate has the same trend. This figure relates the exergy net with the exergy destruction.

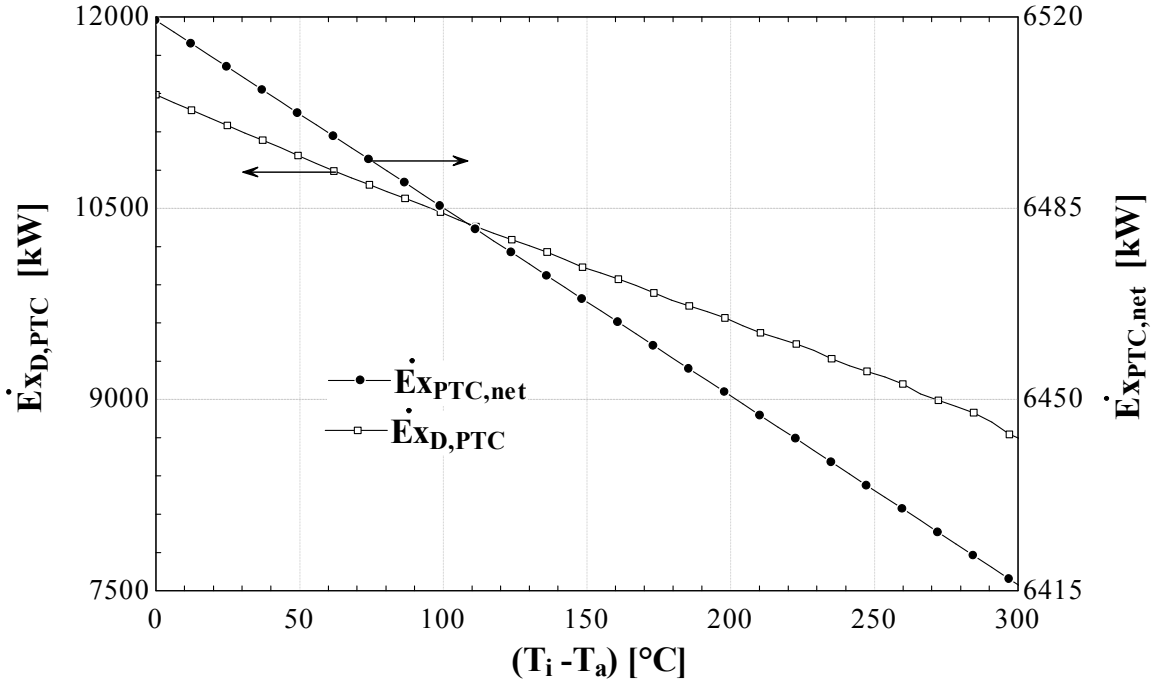

Figure 6.15: The variations in the net PTC exergy output and exergy destruction rate in PTC solar field with the variation in PTC inlet temperature above ambient.

The variations of different heat losses from the PTC with the variation in the PTC inlet temperature above ambient are presented in Fig. 6.16. The total heat energy losses are comprised of two main types of optical heat losses and receiver heat losses. As observed from the Fig. the optical heat losses remain constant and show no variation with the change in inlet temperature, because the heat losses, due to optical and geometrical factors, are almost independent of the temperature change within the receiver. However, the receiver heat losses considerably vary with the inlet temperature of the solar field. This trend is expected since the rise in temperature in the receiver will increase the heat transfer between the HTF and ambient air.

In Fig. 6.17, the effects of the variation in the solar radiation incidence angle on the absorbed solar radiation and total heat energy loss from the PTC are shown. It can be noticed that, with increasing the solar radiation incidence angle, the absorbed solar radiation declines and the total heat loss increases. This figure confirms that the orientation of the collector is critical and errors that could increase the radiation incidence angle can be costly in terms of thermal energy losses.

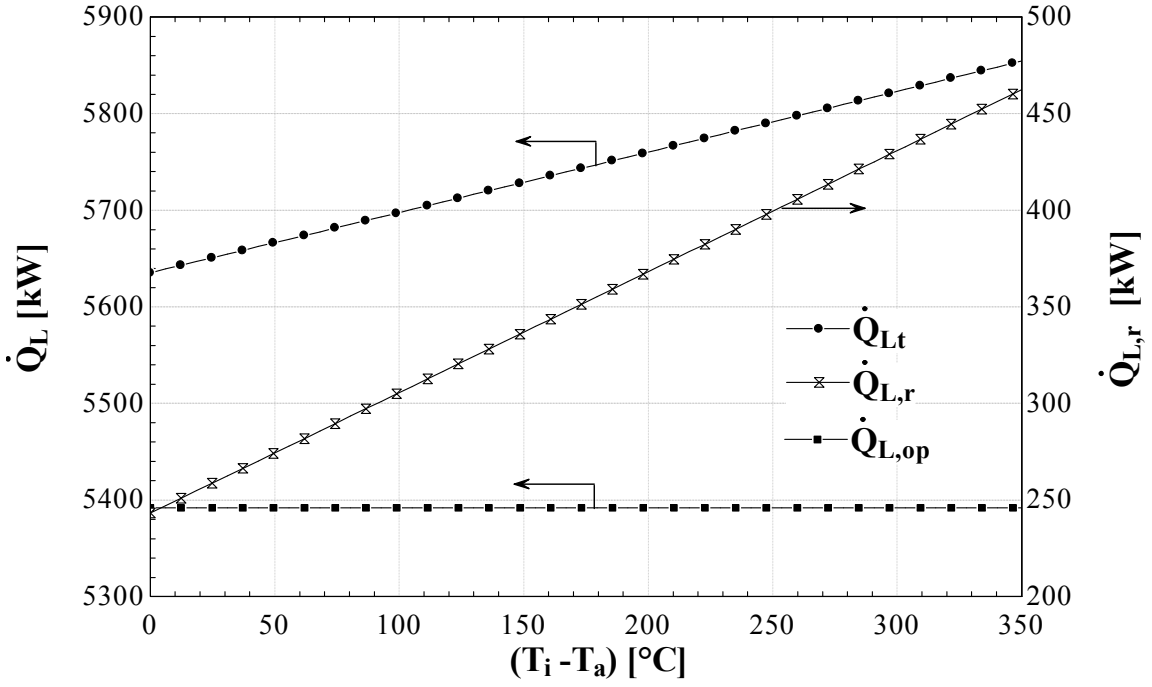

Figure 6.16: The variation in the different heat losses from the PTC with various inlet temperatures above ambient.

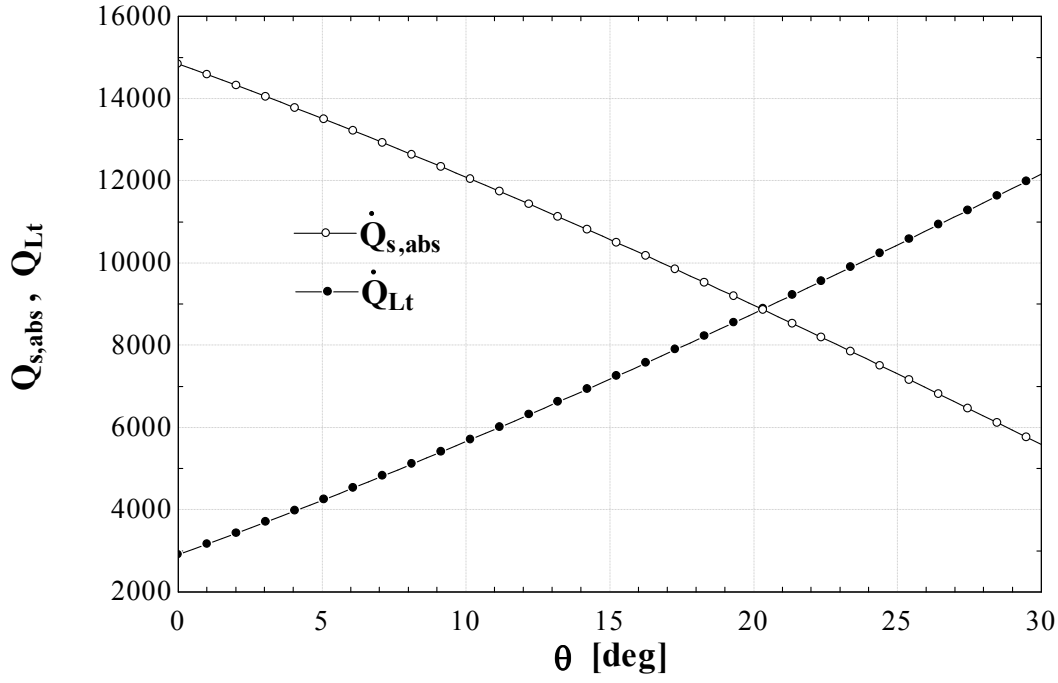

Figure 6.17: The effects of the variation in solar radiation incidence angle on the absorbed solar radiation heat and total heat loss.

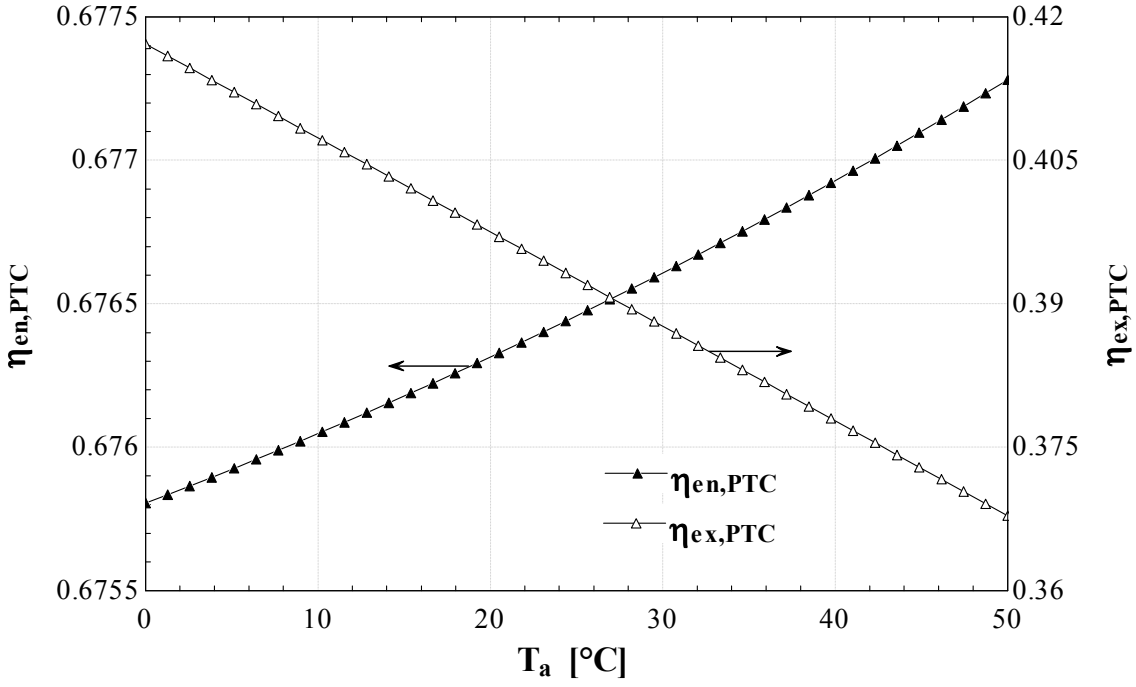

Figure 6.18: The effects of changing ambient temperature on the energy and exergy efficiencies of the PTC.

In Fig. 6.18, an assessment of the PTC performance at different ambient temperatures is presented, including the energy and exergy efficiencies of the PTC. The energy shows a linear increase with increasing the ambient temperature. However, the exergy shows exactly the opposite since, the increase in the ambient temperature results in a reduction in the temperature difference between the HTF, flowing through the receiver, and the ambient temperature and subsequently, the heat losses from the receiver decrease and energy efficiency increases. In contrast, exergy-wise, the increase in the ambient temperature will result in a reduction in the exergy of the HTF thereby reducing the exergy efficiency. In many cases, the ambient temperature is not a matter of choice for the designer, rather it is a comparative reference point.

In Figs. 6.19 and 6.20, the exergy destruction rates in the different power cycle components are evaluated over a range of ambient temperatures. In Fig. 6.19, the exergy destruction rate in the cycle's condenser, high pressure turbine, and low pressure turbine are illustrated. They show a slight increase with increasing ambient temperature. In Fig. 6.20, the exergy destruction rate in the cycle's internal heat exchanger, heater and reheater are presented for the same ambient temperature range. However, the heater and

reheater show a considerable reduction in exergy destruction with the increase in ambient temperature. The amount of exergy destruction rate per IHE increases considerably with increase in the ambient temperature. It is noticeable from Fig. 6.19 and Fig. 6.20 that most of the exergy destroyed within the power cycle is associated with the heat transfer processes, and highest exergy destruction occurs in the IHT followed by the HE then, the condenser and the RE. The lowest exergy destruction rate occurs in the HPT.

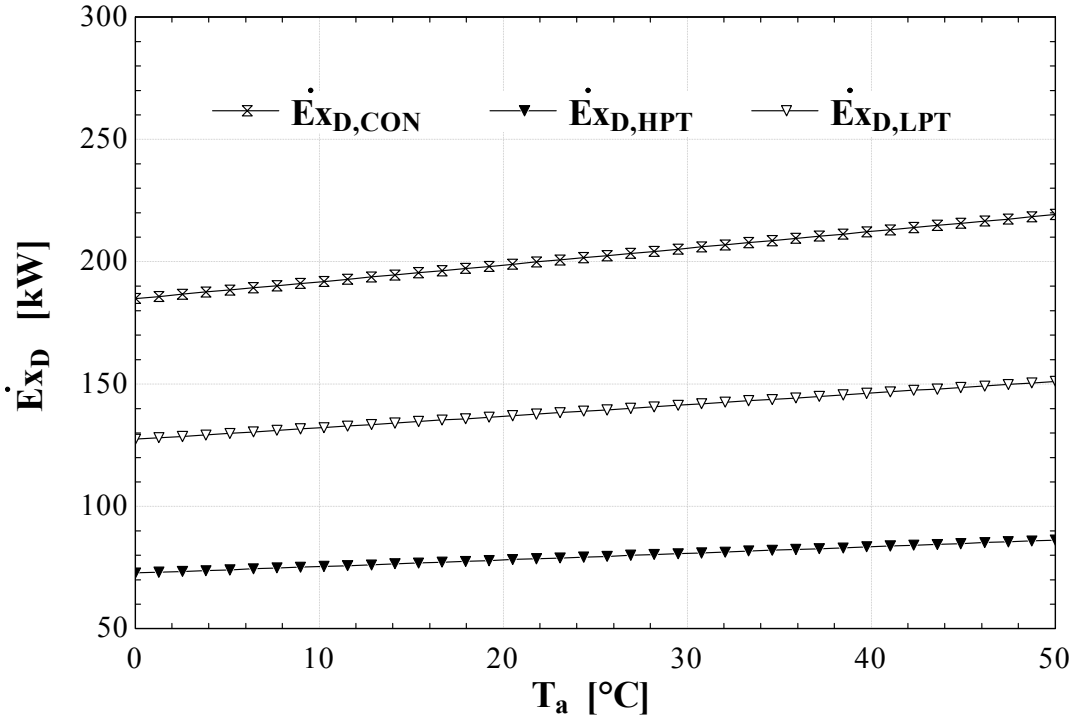

Figure 6.19: The effect of changing ambient temperature on the exergy destruction rate in the condenser, high pressure turbine, and low pressure turbine.

Fig. 6.21 presents the shares of exergy destruction rate of each subsystem related to the total exergy destruction within the overall integrated system. Furthermore, this figure shows that the most of the exergy is destroyed within the PTC which represents about 65% of the total exergy destruction. The exergy destruction rate share of the S-CO_2 Rankine power cycle and the ARS are 17% and 18%, respectively.

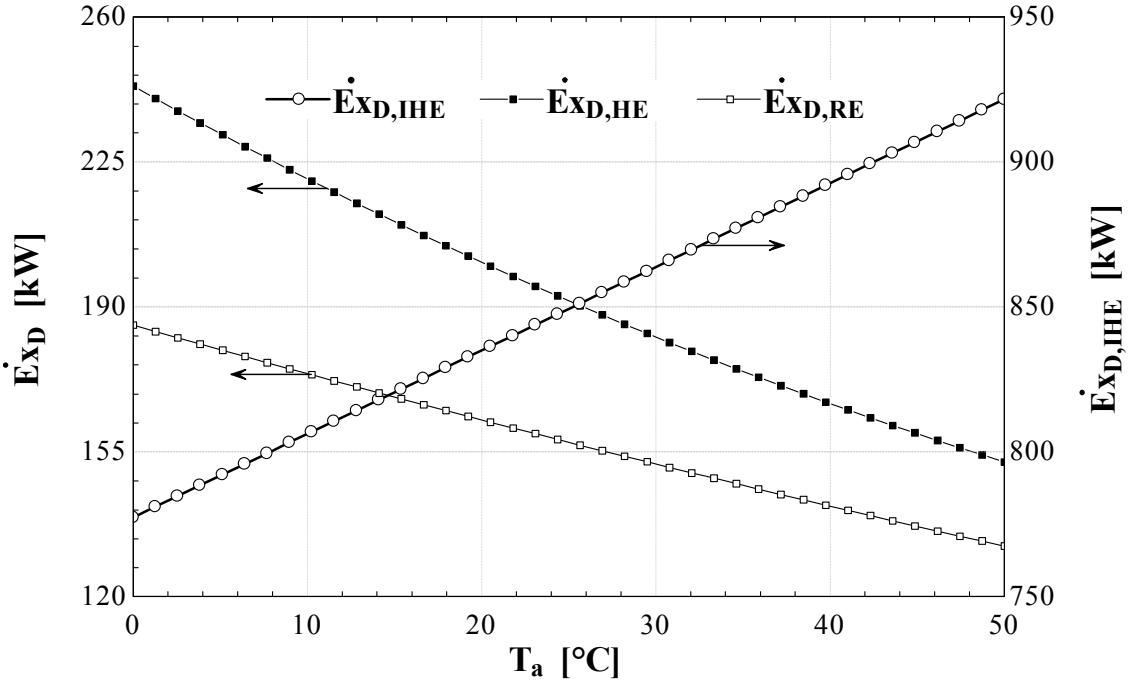

Figure 6.20: The effect of the change in ambient temperature on exergy destruction rate in the internal heat exchanger, heater and reheater.

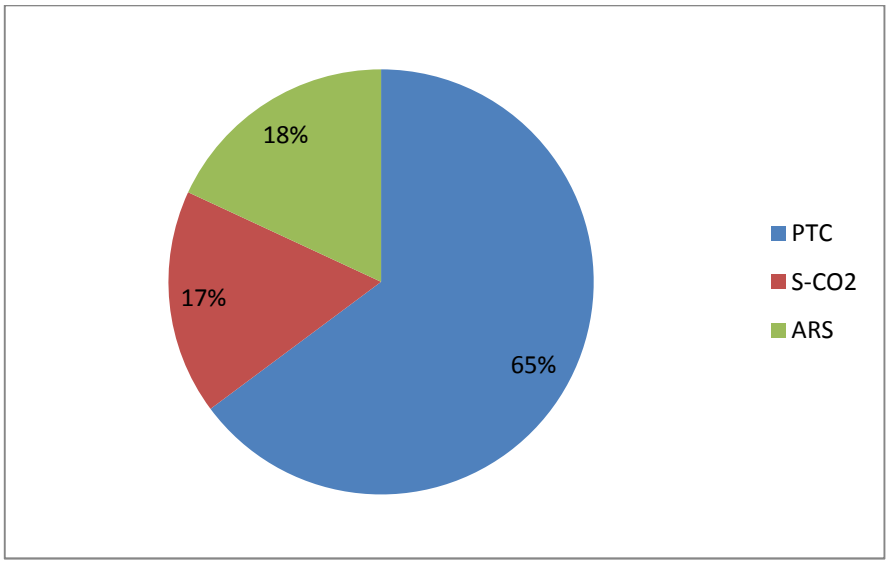

Figure 6.21: Shares of exergy destruction rate within the PTC, the S-CO_2 Rankine power cycle and the ARS.

A better illustration of exergy destruction rates occurred within the S-CO_2 Rankine power cycle and the ARS is given in Fig. 6.22, where exergy destruction rate per every component is presented in a comparison layout with other components. It can be noticed that the maximum exergy is destroyed within the S-CO_2 Rankine power cycle is

occurred in the IHE while with regard to the ARS the maximum exergy is destroyed in the desorber.

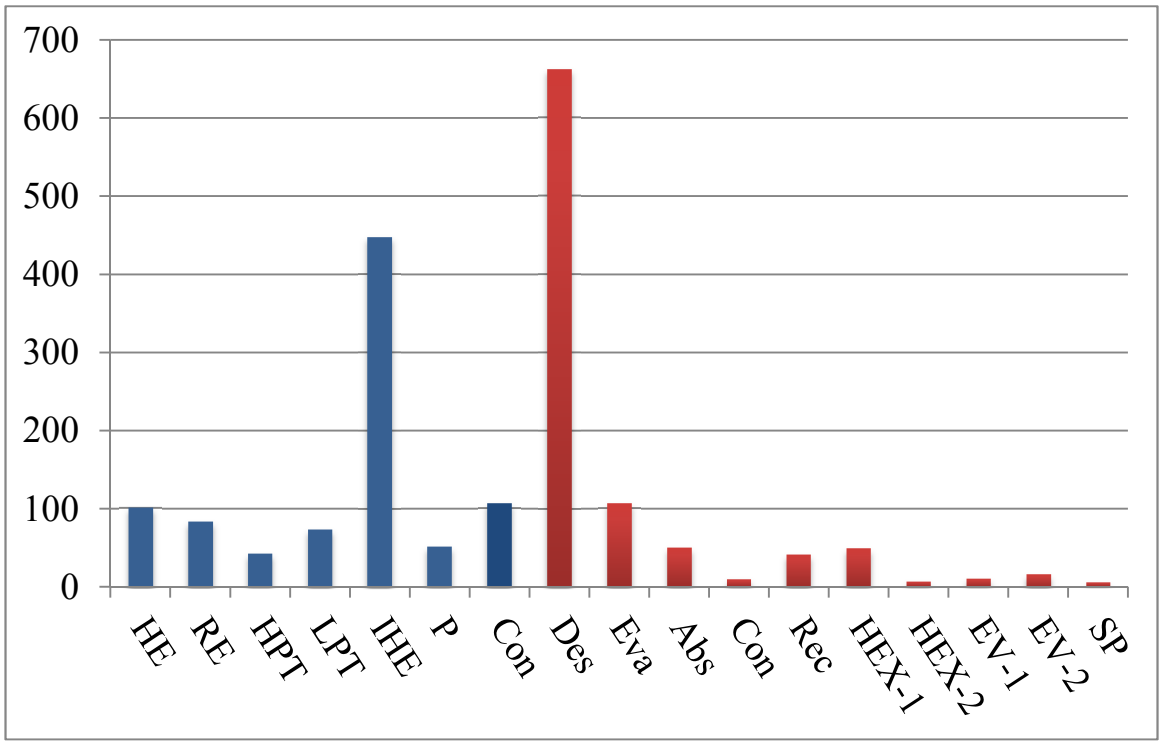

Figure 6.22: Exergy destruction rates pre the different components of S-CO_2 power cycle and ARS.

6. 2 TES System

The energy and exergy analyses of the TES system are carried out based on one cycle operation, including the following three TES operating processes: charging process, storing process and discharging process. The energy and exergy efficiencies evaluated on this are commonly called the round-trip-efficiency. Fig. 6.23 shows the round-trip energy and exergy efficiencies of the TES based on the total temperature drop in the hot TES tank. It can be obtained that the TES achieving a round-trip-energy efficiency above 98% even in the case of 7 degree drop in temperature between the two processes charging and discharging. The heat losses vary from 0 to 8 MW based on the temperature drop during the storing process.

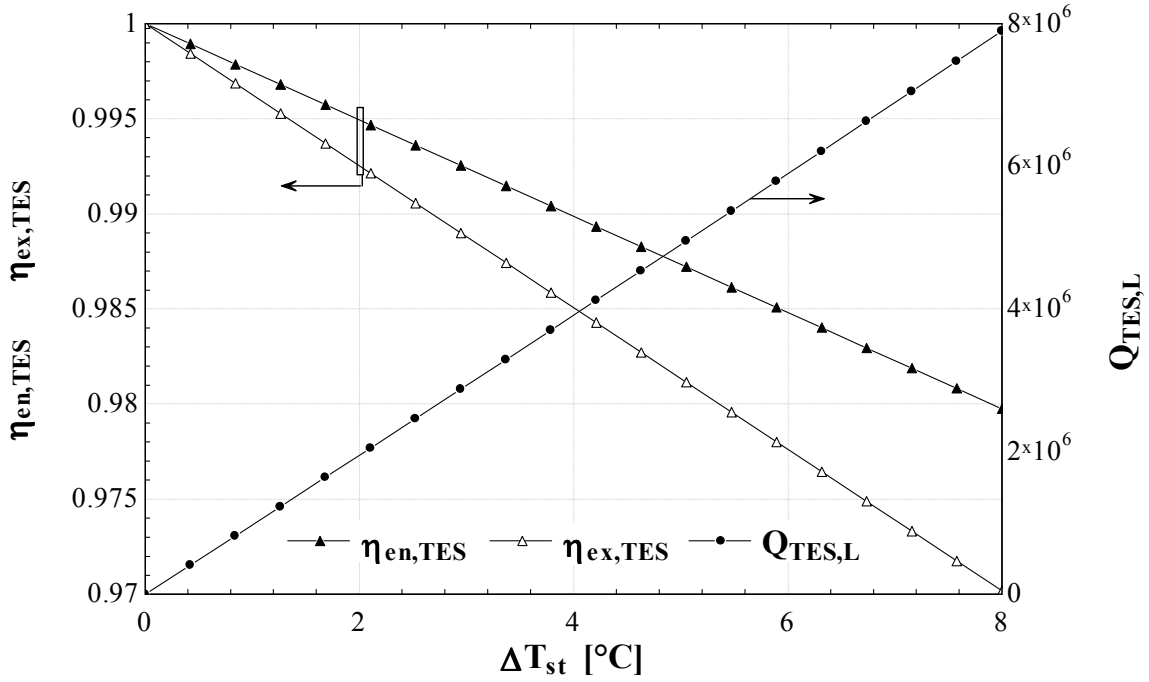

Figure 6.23: The round trip-energy and exergy efficiencies of the TES system as well as the heat losses associated with total temperature drop during the storing period.

The TES volume depends mainly on how many hours of full load operation will be supplied by the TES in absence of solar energy and the thermal energy storing medium. In the current TES system, the storing medium used is Therminol-PV1 which is the same as the HTF. The advantages of this storing technique are discussed in the previous chapters.

Fig. 6.24 illustrates the mass of oil as well as the volume required by each tank of the TES. It can be seen that the mass and volume are increasing linearly with increasing the hours of operation that must be supplied by TES system. However, the base case TES system is designed for 12 hours operation and accordingly the volume required by each tank calculated to be 420.8 (m^3). The dimensions of the two cylindrical TES tanks are assumed to be 7 *m* in diameter and 11 *m* in length.

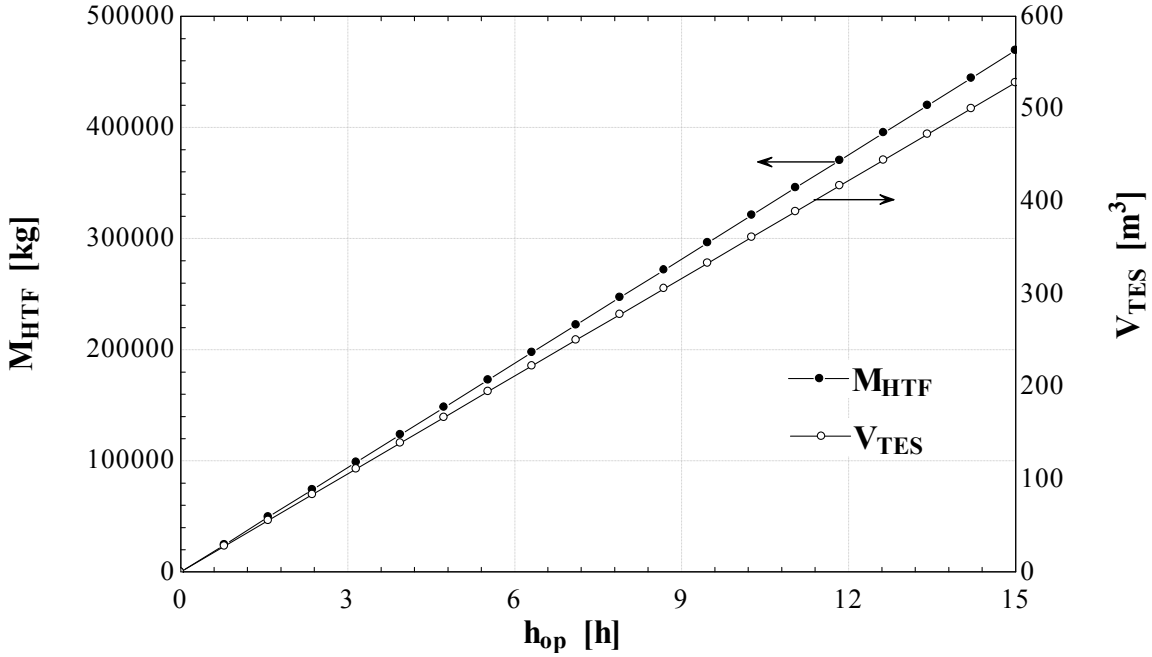

Figure 6.24: The mass of HTF and the volume needed for storage with a range of different operating hours from TES.

6. 3 Reheat S-CO_2 Rankine Power Cycle

The main assumptions made to analyze the S-CO_2 Rankine power cycle are presented in Table 6.4. These assumptions include the HPT inlet temperature and pressure, turbines isentropic efficiencies, pump isentropic efficiencies, heat exchangers effectiveness, pinch temperature, and reheat pressure.

Table 6.4: Main assumption from the S-CO_2 Rankine power cycle.

Main assumptions for S-CO_2	
T_{12} (^{o}C)	384
Turbines isentropic efficiencies (%)	85
Pump isentropic efficiency (%)	70
IHE effectiveness (%)	100
T_{p} (^{o}C)	8
T_{17} (^{o}C)	3
P_{13} (MPa)	$(P_{12} * P_{15})^{1/2}$
P_{12} (MPa)	15

Table 6.5 presents the working fluid's properties at the different state points such as mass flow rate, temperature, pressure, specific exergy, specific enthalpy, specific entropy, and quality. This table is based on the base case assumption presented earlier.

Table 6.5: The state points data for the S-CO_2 Rankine power cycle.

State point	Fluid	$\dot{m}$ (*kg/s*)	T (^{o}C)	P (*MPa*)	ex (*kJ/kg*)	h (*kJ/kg*)	x (-)	s (*kJ/kg-K*)
0	CO_2	-	25	0.1011	0	-0.9365	-	-0.00183
12	CO_2	9.402	382	15	392.9	328.8	1	-0.2136
13	CO_2	9.402	330.1	9	337.8	278.2	1	-0.1987
14	CO_2	9.402	382	9	369.3	338.1	1	-0.1034
15	CO_2	9.402	298.8	3.77	277.9	254.4	1	-0.07728
16	CO_2	9.402	22.52	3.77	192.7	-46.4	1	-0.8007
17	CO_2	9.402	3	3.77	211.8	-299.3	0	-1.713
18	CO_2	9.402	14.52	15	223.7	-282	1	-1.695
19	CO_2	9.402	135.9	15	261.3	18.8	-	-0.8121

In Fig. 6.25 the changes in energy and exergy efficiencies are examined with changing the S-CO_2 condenser temperature (ARS evaporator temperature). The efficiencies are evaluated for the combination of the S-CO_2 power cycle and the cooling system. The energy efficiencies are varied linearly between 10% to 22% for the combined power and cooling system. The exergy efficiencies also varied in the same patterns, with higher figures, between 25% to 60%. A general observation from Fig. 6.25 is that the power cycle is performing better at lower condenser temperatures because of the increase of the work that can be extracted by expanding to a lower pressure. For example, if the ARS have not been used and cooling water was available to achieve the condensation process at 15^{0}C (which is quite difficult for a year round operation) the system will have an energy efficiency of 10% and exergy efficiency of 25%. However, the introduction of the ARS enables achieving lower condensation temperature and stable cooling system around the year and independent of the weather changes.

The performance of the S-CO_2 Rankine power cycle with changing the condensation temperature is illustrated in Fig. 6.26. The energy and exergy efficiencies of the S-CO_2 cycle are varying from 26% to 36% and from 50% to 66%, respectively. Fig. 6.26 shows also the variations in the energy and exergy efficiencies of the overall system.

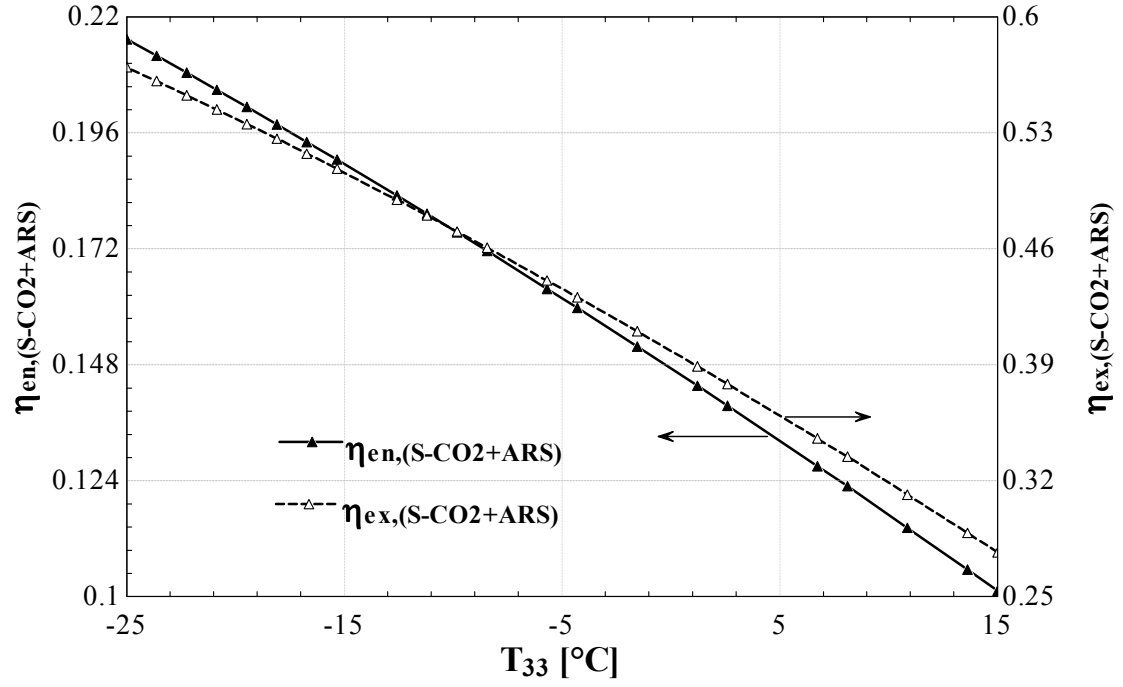

Figure 6.25: The changes in the energy and exergy efficiencies for the combined S-CO_2 Rankine power cycle and the ARS with the change in Condenser/Evaporator temperature.

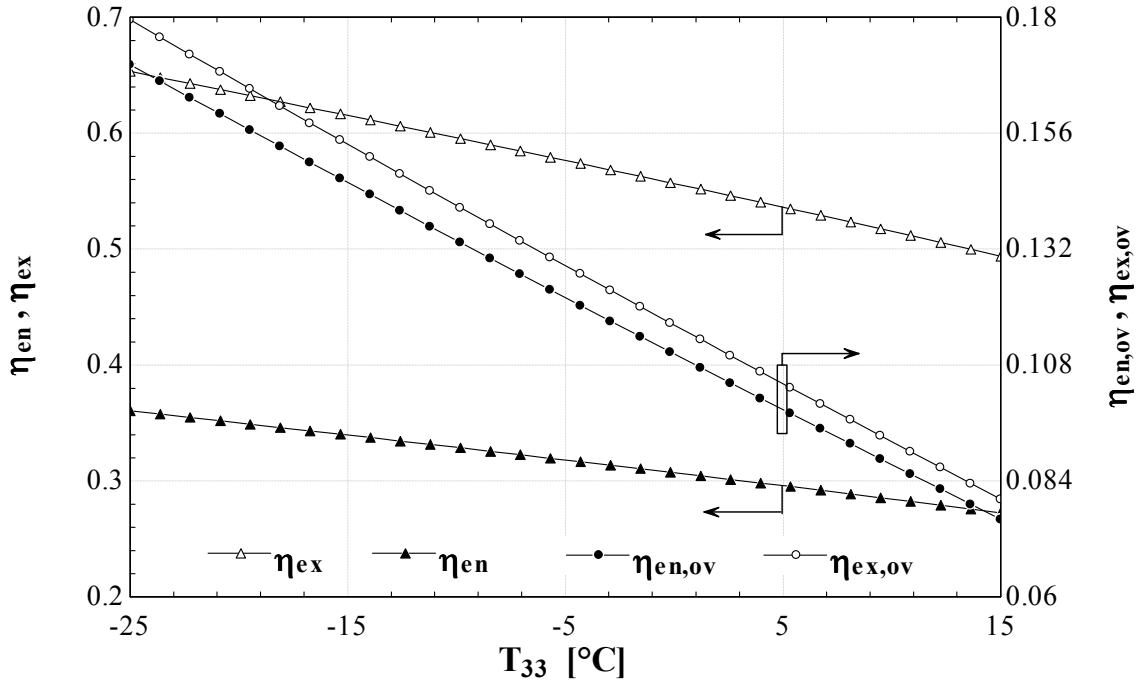

Figure 6.26: The variations in the S-CO_2 Rankine power cycle energy and exergy efficiencies as well as the associate variations in the overall system energy and exergy efficiencies with changing the power cycle condensation temperature.

The effects of varying the maximum cycle pressure of the S-CO_2 Rankine power cycle on the cycle energy and exergy efficiencies are presented in Fig. 6.27. It can be clearly seen that the increase in the cycle pressure will have a positive impact on the cycle performance energy and exergy wise.

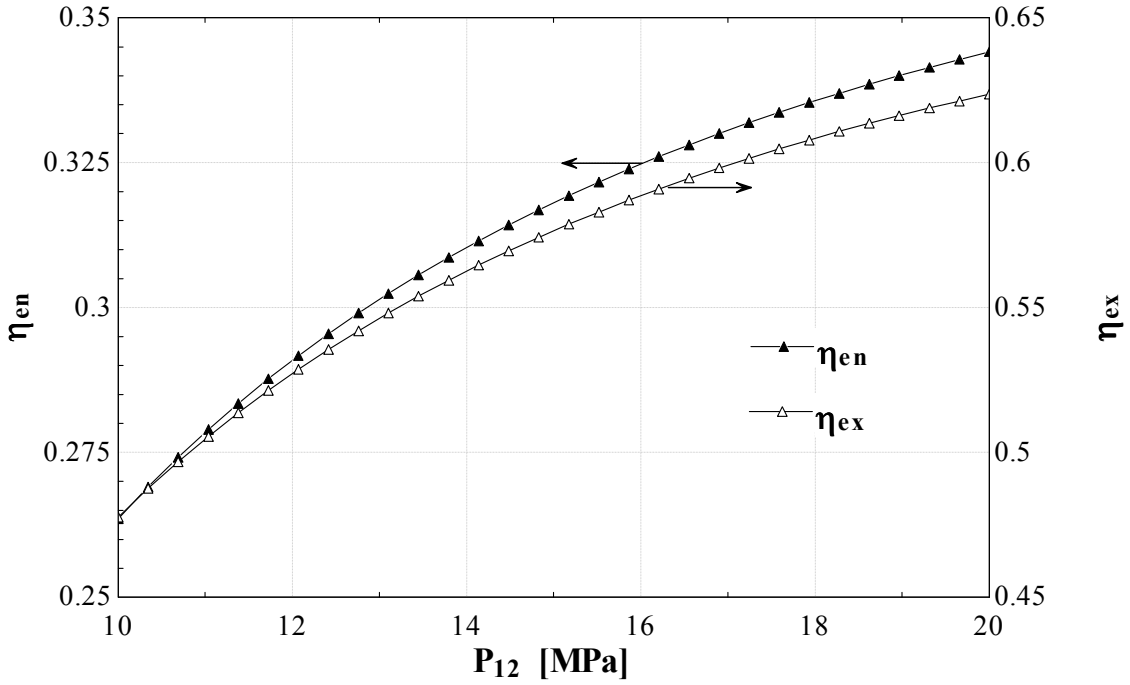

Figure 6.27: The variations in the S-CO_2 Rankine power cycle energy and exergy efficiencies with changing the maximum cycle pressure.

The effects of varying the maximum cycle temperature (source temperature) on the S-CO_2 Rankine cycle energy and exergy efficiencies can be are shown in Fig. 6.28. The figures the high potential of the S-CO_2 Rankine power cycle especially for high temperature application such as solar tower. The cycle is expected to achieve energy and exergy efficiencies of 38.5% and 56.5%, respectively, when turbines inlet temperatures of 560 °C is achieved.

In Fig. 6.29, the shares of the exergy destruction rates per the different components of the cycle are shown. It can be clearly noticed that the maximum exergy destruction occurs in the IHE (52% of the total exergy destroyed within the S-CO_2 Rankine cycle) followed by the heater and reheater.

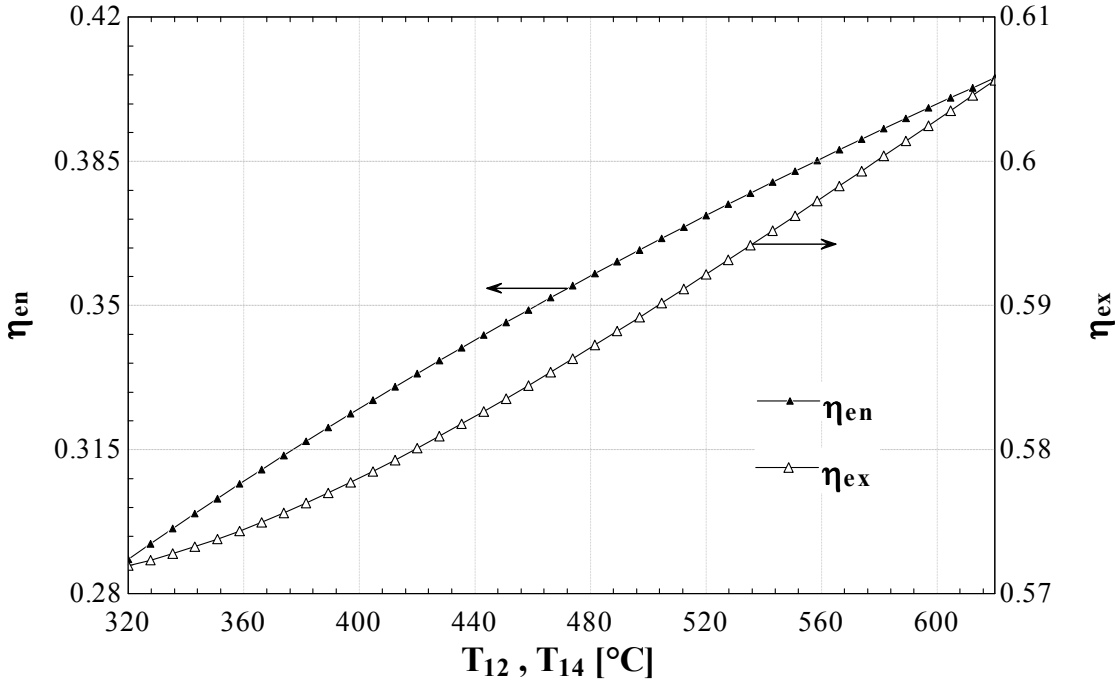

Figure 6.28: The variations in the energy and exergy efficiencies of the S-CO_2 Rankine power cycle with changing the maximum cycle temperatures.

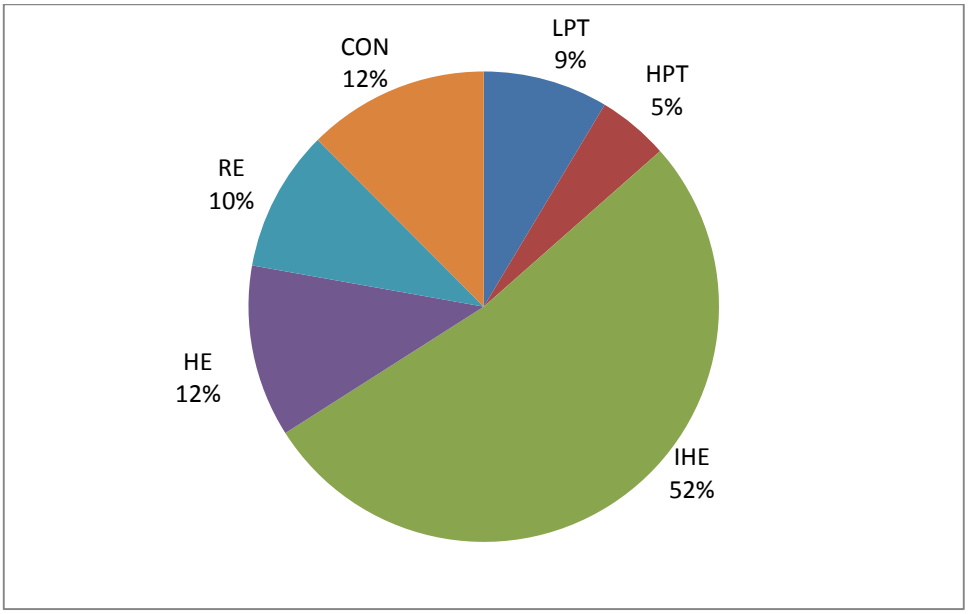

Figure 6.29: The shares of exergy destruction rate per each component of the S-CO_2 Rankine cycle.

6. 4 Absorption Refrigeration System

The energy and exergy analysis of the ARS involves a parametric study which investigates the effect of changing each of the operating parameters on the ARS overall performance. The energy and exergy coefficients of performance (COPs) of the system are evaluated over a wide range of possible operating conditions to optimize the cycle design for energy and exergy performance.

The properties of the ARS at the different state points are presented in Table 6.6. The table illustrates the type of working fluid as each state and other properties such as mass flow rate, temperature, pressure, specific exergy, specific enthalpy, quality, specific entropy, and concentration.

Table 6.6: State points data for the ARS.

State point	Fluid	$\dot{m}$ (*kg/s*)	T (^{o}C)	P (*kPa*)	ex (*kJ/kg*)	h (*kJ/kg*)	x (-)	s (*kJ/kg-K*)	C (-)
21	NH_3/H_2O	12.76	30	312.4	781.4	-104.9	0	0.2966	0.4706
22	NH_3/H_2O	12.76	30.16	1167	782.5	-103.4	-0.01	0.298	0.4706
23	NH_3/H_2O	12.76	77.05	1167	805	135.8	0.02055	1.025	0.4706
24	NH_3/H_2O	10.73	94.64	1167	732.9	201.2	0	1.188	0.3706
25	NH_3/H_2O	10.73	38.12	1167	702.5	-50.59	-0.01	0.4453	0.3706
26	NH_3/H_2O	10.73	38.29	312.4	701.5	-50.59	-0.01	0.4485	0.3706
27	NH_3/H_2O	2.084	75.11	1167	1350	1433	1	4.714	0.9855
28	NH_3/H_2O	0.0555	73	1167	799.5	99.46	0	0.9215	0.4706
29	NH_3	2.029	36	1167	1340	1296	1	4.295	0.999
30	NH_3	2.029	30	1167	1317	141.5	0	0.5003	0.9996
31	NH_3	2.029	19.49	1167	1317	91.07	-0.01	0.3309	0.9996
32	NH_3	2.029	-8.21	312.4	1309	91.07	0.0994	0.3575	0.9996
33	NH_3	2.029	-5	312.4	1168	1263	0.997	4.762	0.9996
34	NH_3	2.029	14.44	312.4	1165	1314	1.001	4.943	0.9996
36	NH_3/H_2O	12.76	36.34	1167	783.2	-75.9	-0.01	0.3878	0.4706

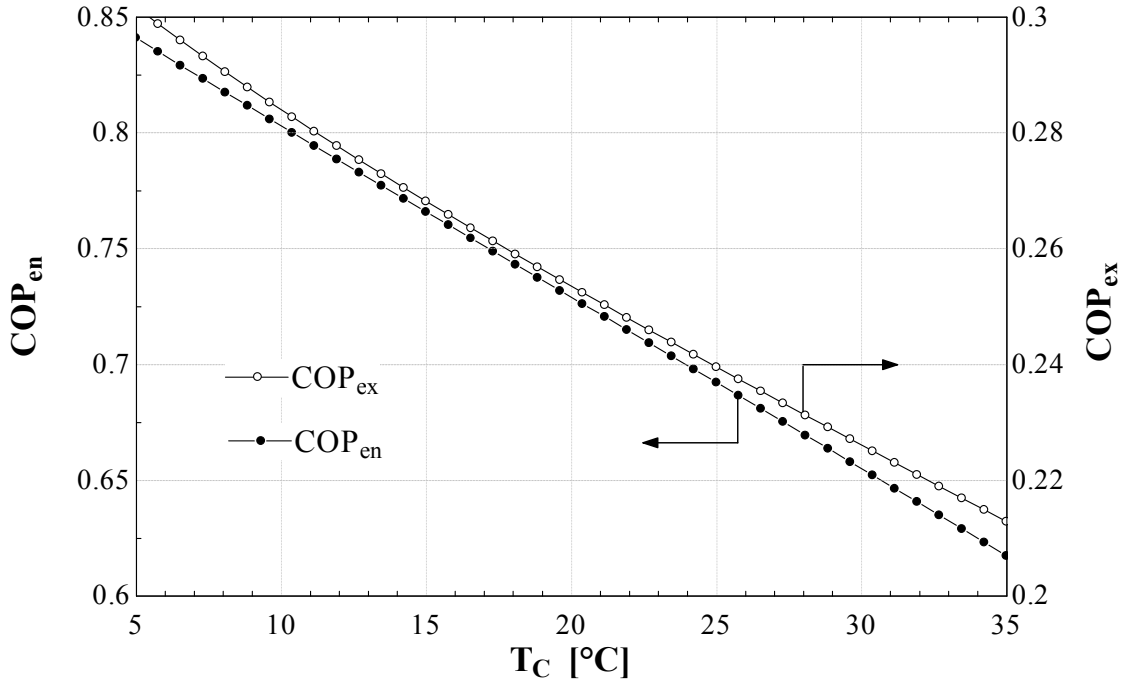

Figure 6.30: The change in the ARS energy and exergy COPs with changing the cooling temperature.

Fig. 6.30 shows the change in the ARS energy and exergy COPs with changing the condenser and the absorber cooling temperatures. It can be noticed that the ARS performance is higher at lower cooling temperatures. The energy COP shows a possible improvement from 0.65 to 0.8 when the cooling temperature decreases from 30 to 10 °C. Over the same temperature range, the exergy COP shows an improvement of about 0.06. However, it might be not practical to design for a cooling temperature below 15 °C, since it would be difficult to achieve, especially in the selected location.

The effects on the ARS performance, of changing the heat source temperature, while maintaining the heat duties constant, are shown in Fig. 6.31. It can be noticed that the energy COP remains constant over the entire range while the exergy COP shows a dramatic change. This is because of the limitation of the energy analysis since it only considers the quantities rather than the quality. However, the exergy analysis clearly shows the preferable operating condition since it considers both energy quantity and energy quality as the second law of thermodynamics implies. Fig. 6.31 represents one of the great advantages of exergy analysis for systems design. The increase in the exergy

COP, with decreasing the heat source temperature as shown in Fig. 6.31, is due to the reduction in the exergy destruction when operating at lower temperatures. Thereby, the exergy COP suggests using a lower temperature energy source to increase the exergy performance of the ARS unit and for best utilization of that energy source.

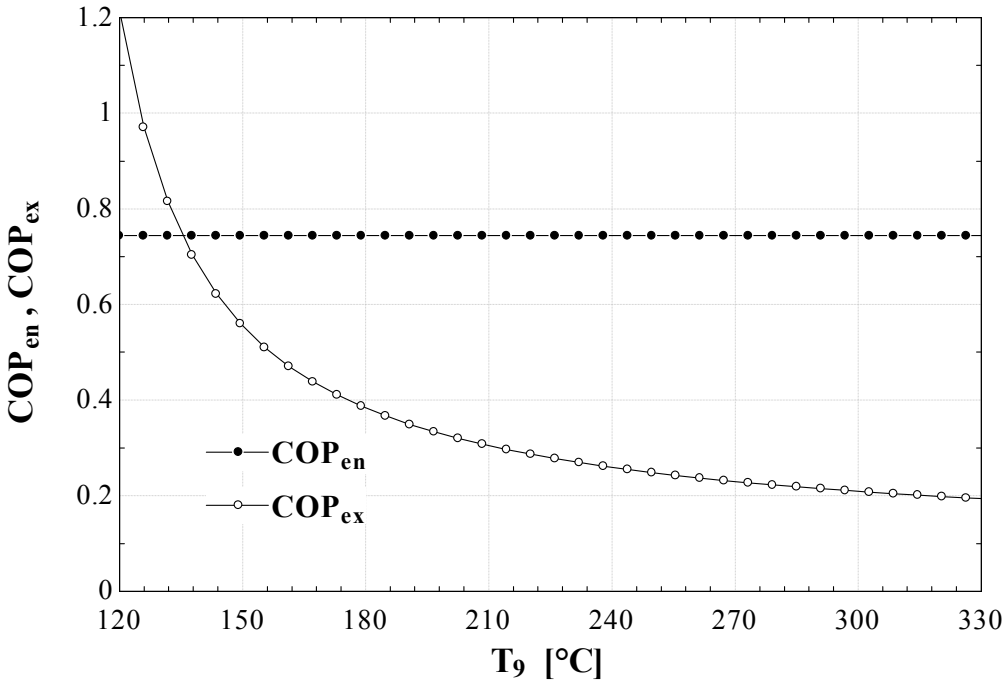

Figure 6.31: The change in the energy and exergy COPs with changing the heat source temperature.

The ARS condenser and absorber can be cooled by connection to a water loop either in parallel or in series. When they are connected in parallel, the water enters the absorber and the condenser at the same temperature, while in series it passes through the absorber and then the condenser. The effect of the cooling temperature change while in parallel is presented in Fig. 6.32.

In Fig. 6.33, the effect of the changing the condenser cooling temperature on the energy and exergy COPs is illustrated. The ARS shows higher performance at lower condenser cooling temperature. From this figure, it can be seen that the reduction in the condenser cooling water temperature from 28 to 18 °C will improve the energy and exergy COP by 0.03 and 0.011, respectively.

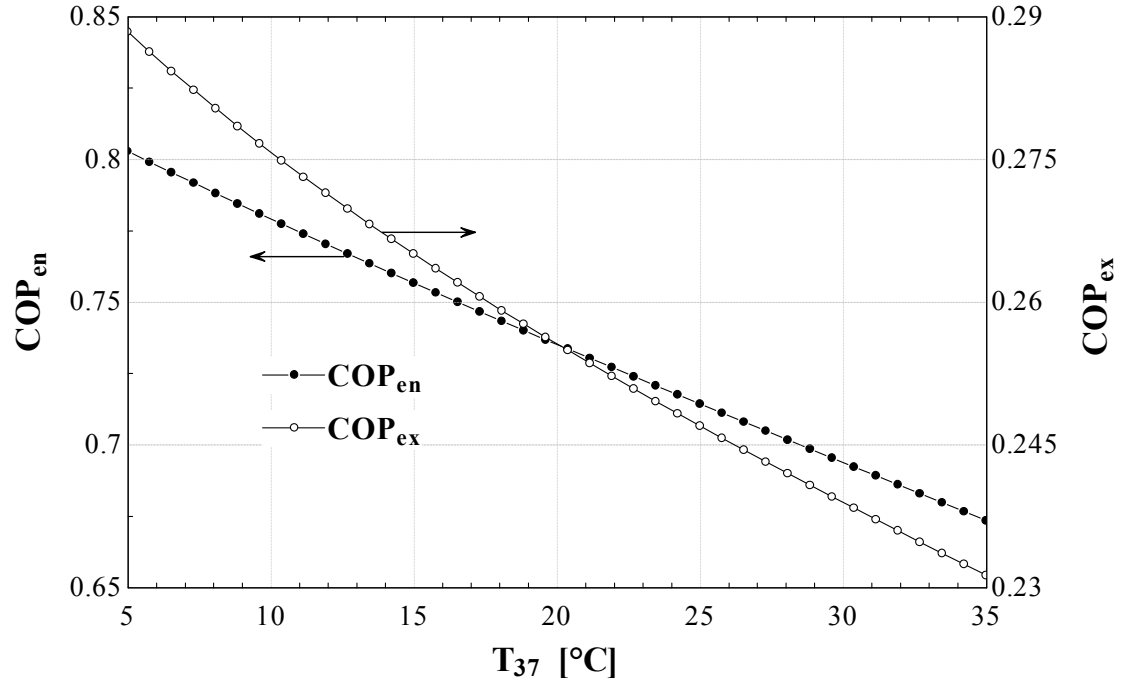

Figure 6.32: The effects of changing the absorber cooling temperature on the energy and exergy COPs.

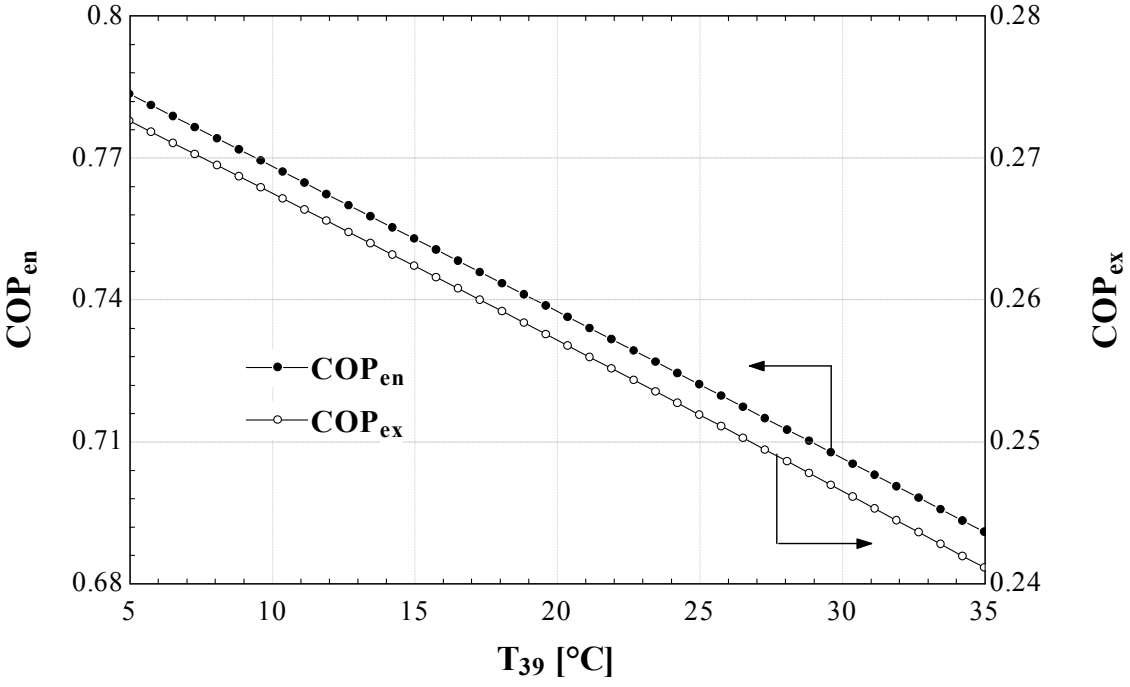

Figure 6.33: The effects of changing the condenser cooling temperature on the energy and exergy COPs.

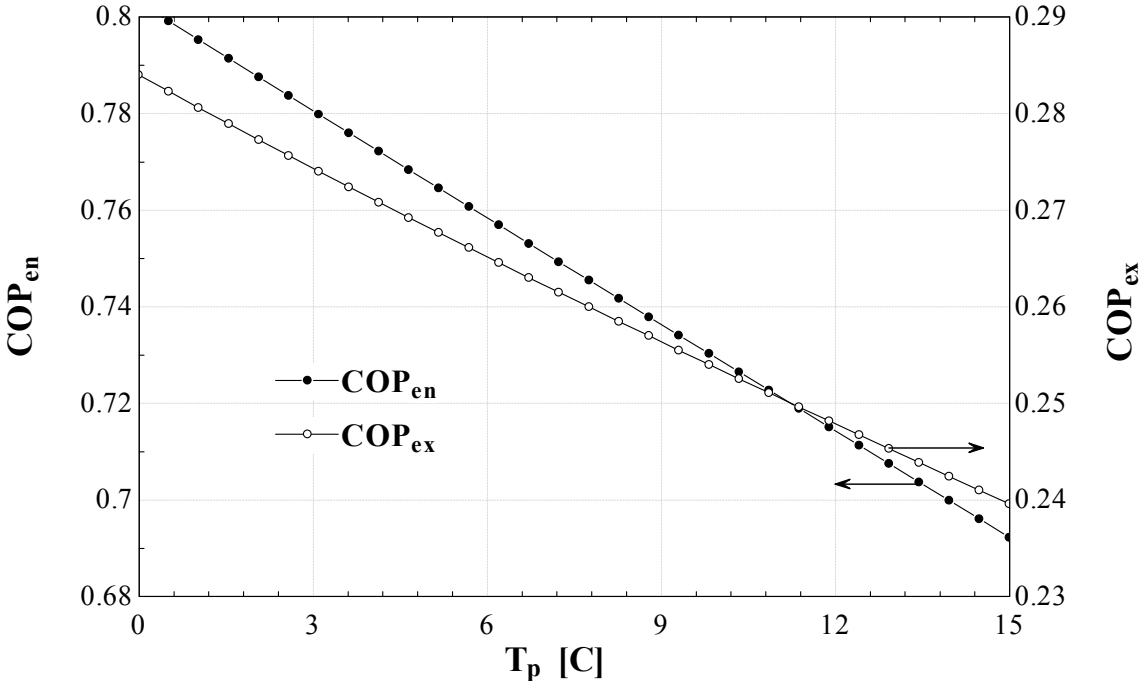

Figure 6.34: The effects of varying the pinch temperature of the energy and exergy COPs.

The effects of changing the assumed pinch point, T_p, for the different heat exchanging elements on the energy and exergy COPs of the ARS are presented in Fig. 6.34. The ARS can achieve as high as 0.76 in energy COP, and 0.265 in exergy COP, by employing heat exchangers with a pinch point temperature of 6 ^{0}. However, with a higher pinch point temperature of 15 ^{0}, the energy and exergy COPs will decrease to about 0.685 and 0.24, respectively.

The effect of using the solution heat exchanger with different effectiveness values on the ARS performance is illustrated in Fig. 6.35. The impact of using the solution heat exchanger on the energy and exergy COPs of the ARS can be clearly noticed by comparing the system performance, with effectiveness of zero, meaning no heat exchanger has been used, to the performance of a reasonable effectiveness. Accordingly, without introducing the solution heat exchanger, the energy and exergy COPs of the ARS are 0.4 and 0.18, respectively. However, if these are compared with the energy and exergy COPs of the same system after using a solution heat exchanger which has an effectiveness of 0.85. The energy and exergy COPs then increase to 0.65 and 0.24,

respectively and the overall improvement in the energy COP is 0.25 and in the exergy COP is 0.06.

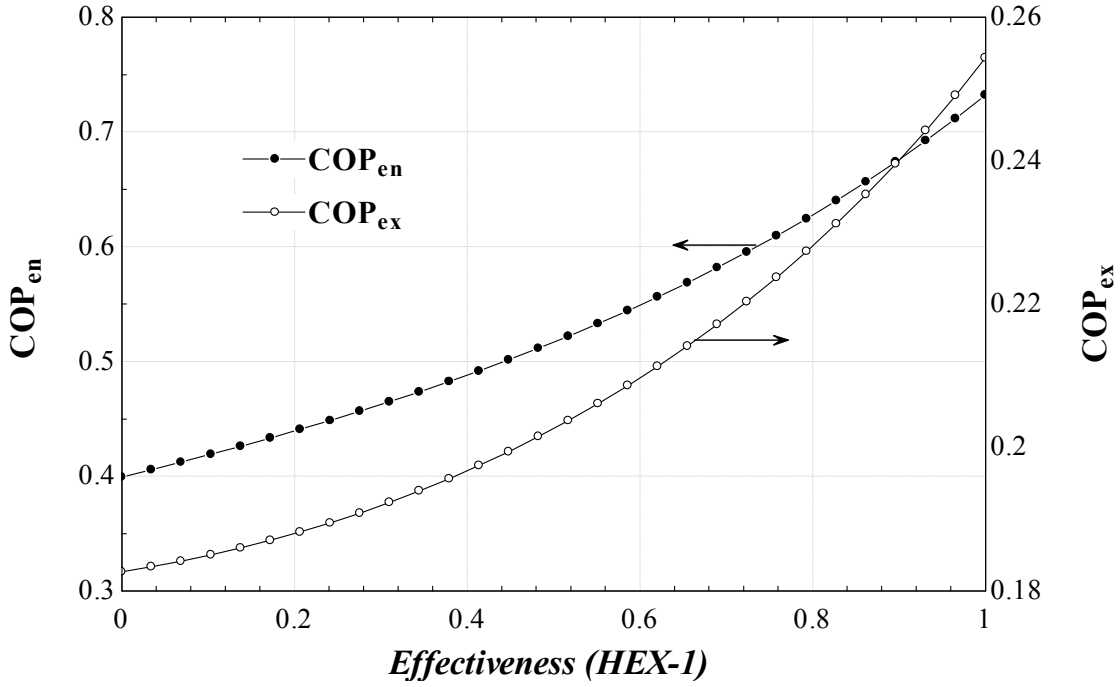

Figure 6.35: The effects of changing the solution heat exchanger (HEX-1) effectiveness on the ARS energy and exergy-based COPs.

The impact of using the second heat exchanger (HEX-2) on the ARS energy and exergy-based COPs is shown in Fig. 6.36. As presented in this figure, the energy and exergy COPs can be improved from about 0.67 to about 0.70 and from 0.23 to 0.246, respectively, by using a heat exchanger to recover heat energy between the two refrigerant streams going and coming from the evaporator. However, more studies involve cost are necessary to clearly see if this performance is justified cost wise.

The distribution of exergy destruction rate ratios to the total exergy rate destroyed within the ARS is shown in Fig. 6.37. The figure shows almost 70% of the exergy destroyed in the ARS is occurred in the desorber. The expected reason behind that is the relatively high temperature that used for operating the ARS while the system can operate at a lower temperature. The remaining share about 30% is distributed between the other ARS components.

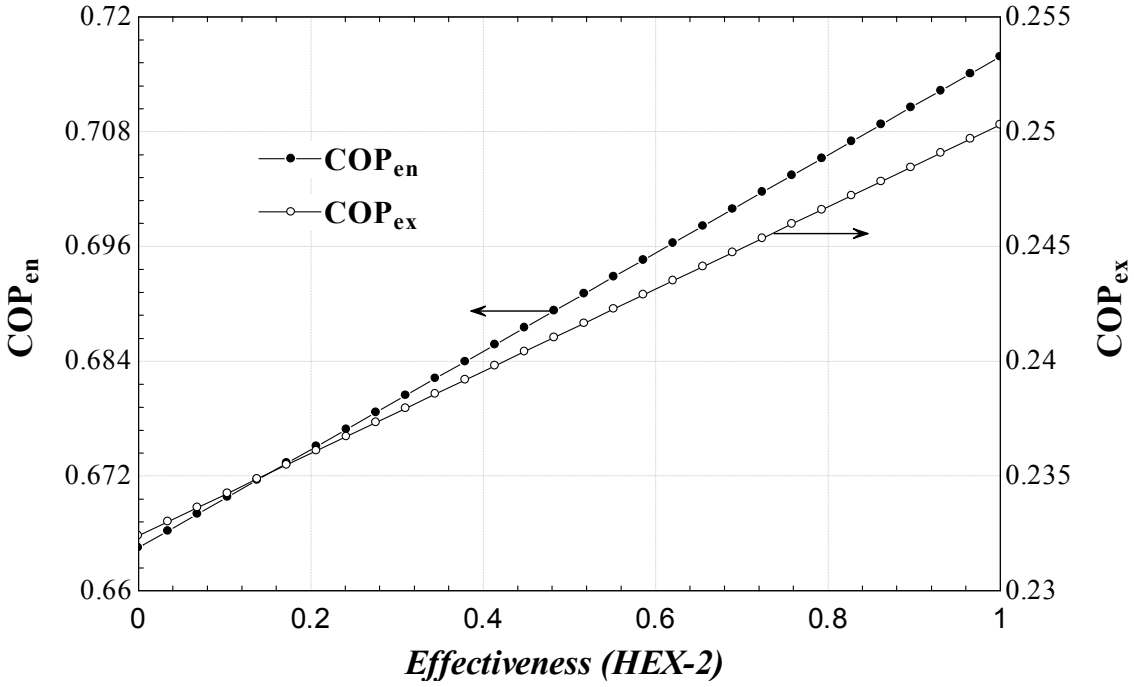

Figure 6.36: The variations in the energy and exergy-based COPs of the ARS with changing the effectiveness of the HEX-2.

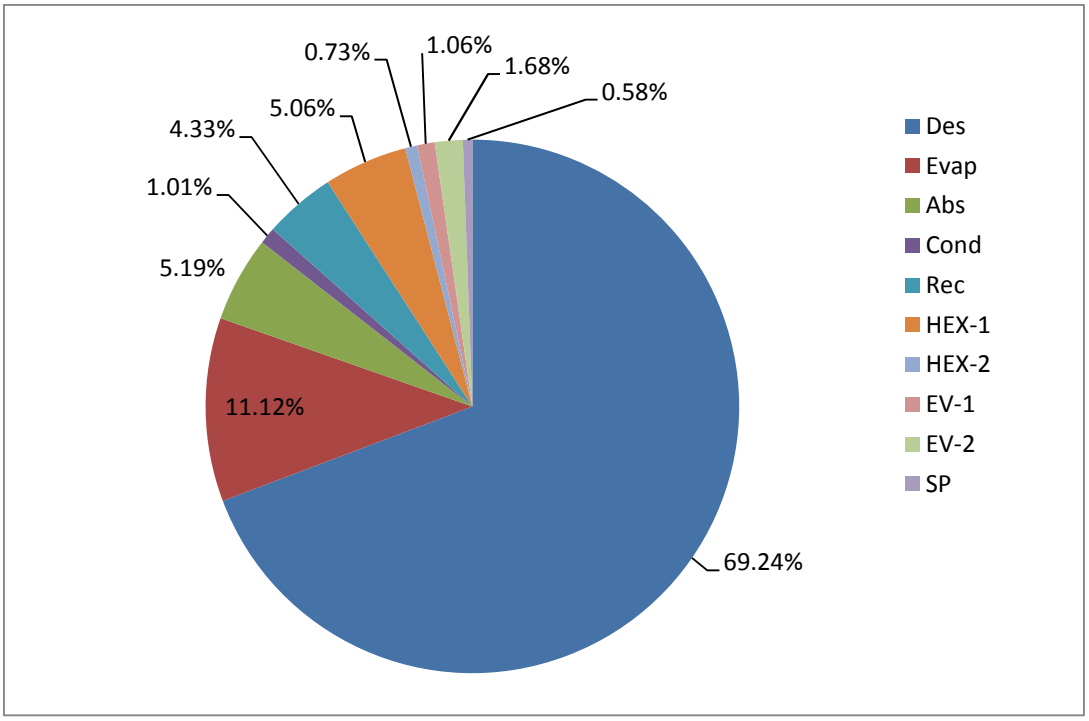

Figure 6.37: Shares of exergy destruction rates within the ARS.

Chapter 7: Conclusions and Recommendations

In this study, a thermodynamic-based design and analysis of a novel solar-based integrated system for power production is conducted. A reheat supercritical carbon dioxide (S-CO_2) Rankine cycle is proposed for power production. This cycle is then integrated with a PTC solar field, a TES system and an ARS. The analysis includes a parametric study for each subsystem and the overall integrated system. The system performance under different operating conditions has been evaluated through the energy and exergy efficiencies as well as the energy and exergy coefficient of performance COP for the absorption system. The heat energy losses and exergy destruction rates are evaluated for the different components.

The effects of the change in some PTC radiation properties and operating conditions on the performance of the PTC solar field are investigated. The PTC properties include, for example, the beam radiation incidence angle, the emittance of the receiver and the emittance of the glass cover. In addition, the operating conditions, such as solar radiation intensity, PTC solar field inlet temperature, wind velocity and ambient temperature, are also studied. The energy losses and exergy destruction rates that are associated with these changes are evaluated. Furthermore, the impact of the change in every parameter on the overall integrated system energy and exergy efficiencies is illustrated. The energy efficiency of the PTC is evaluated to be 66.35% and the exergy efficiency to be 38.51%; this is based on the radiation properties of the Luz systems LS-3 troughs and SCHOTT receivers. The base case analyses of the integrated system are performed for the specific location (Al Madinah) in Saudi Arabia, and the total CSP plant capacity targeted is 1 MW. The total collector area needed is found to be 21850 m^2 based on SM of 2.

The energy and exergy efficiencies of the reheat S-CO_2 Rankine power cycle are examined under the common practical operating conditions of the CSP plants. The exergy destruction rates through the cycle components are evaluated and related to its causes where possible.

7.1 Conclusions

The concluding remarks extracted from this study are summarized by the following points:

- The integration of ARS with the S-CO_2 Rankine power cycle is very promising, particularly for CSP application.
- The reheat Rankine cycle demonstrates good performance with the use S-CO_2 as working fluid.
- The use of ARS as a cooling system can ensure continuous design point performance independent of external water resources temperature or weather changes.
- The S-CO_2 Rankine power cycle is expected to achieve energy and exergy efficiencies of 31.6%, and 57.5%, respectively. Under the same operation conditions, the energy and exergy COPs of the ARS is found to be about 0.7 and 0.27.
- Accordingly, the overall integrated system energy (heat-to-electric) and exergy efficiencies are determined to be 11.73%, and 12.36%, respectively.
- The maximum exergy destruction rate within the overall integrated system occurs in the PTC with about 65% while the ARS and S-CO_2 Rankine power cycle contribute by destroying 18% and 17%, respectively, of the total exergy destruction rate.
- The maximum exergy destruction rate, with respect to the S-CO_2 Rankine power cycle components, is occurred in the IHE. This indicates that more efforts should be directed to the IHE to reduce exergy destruction.
- The maximum exergy destruction rate, with respect to the ARS is occurred within the desorber. However, from the parametric energy and exergy COP studies, it is observed that the change in some operating conditions could have significant improvement in this component exergetic performance, such as reducing the heating source temperature.

7.2 Recommendations

There are several recommendations for future work that can be summarized in the following points:

- An exergoeconomic analysis of the present integrated system should be conducted to study cost matters and exergoeceonomic parameters.
- Such integrated systems should be built and tested for various sectors, including residential applications.
- Other configurations of the S-CO_2 Rankine power cycle integrated with ARS should be investigated for independent cooling system and higher heat-to-electricity conversion efficiency.
- Comprehensive studies on S-CO_2 heat transfer and S-CO_2 heat exchangers especially near critical point are critical for S-CO_2 Rankine cycle improvement.
- The direct S-CO_2 heating through the PTC should be investigated for more efficient and effective operation.

References

Al-Sulaiman, Fahad A. (2014). Exergy analysis of parabolic trough solar collectors integrated with combined steam and organic Rankine cycles. *Energy Conversion and Management, 77*(0), 441-449. doi: http://dx.doi.org/10.1016/j.enconman.2013.10.013

AlZaharani, Abdullah A., Dincer, I., & Naterer, G. F. (2013). Performance evaluation of a geothermal based integrated system for power, hydrogen and heat generation. *International Journal of Hydrogen Energy, 38*(34), 14505-14511. doi: http://dx.doi.org/10.1016/j.ijhydene.2013.09.002

Bao, Junjiang, & Zhao, Li. (2013). A review of working fluid and expander selections for organic Rankine cycle. *Renewable and Sustainable Energy Reviews, 24*, 325-342. doi: 10.1016/j.rser.2013.03.040

Bergman, T. L., & Incropera, Frank P. (2011). *Fundamentals of heat and mass transfer* (7th ed.). Hoboken, NJ: John Wiley.

Chacartegui, R., Muñoz de Escalona, J. M., Sánchez, D., Monje, B., & Sánchez, T. (2011). Alternative cycles based on carbon dioxide for central receiver solar power plants. *Applied Thermal Engineering, 31*(5), 872-879. doi: 10.1016/j.applthermaleng.2010.11.008

Dincer, Ibrahim. (2012). Green methods for hydrogen production. *International Journal of Hydrogen Energy, 37*(2), 1954-1971. doi: 10.1016/j.ijhydene.2011.03.173

Dincer, Ibrahim, & Rosen, Marc. (2011). *Thermal energy storage : systems and applications* (2nd ed.). Chichester, West Sussex ; Hoboken, N.J.: Wiley.

Dostal, Vaclav. (2004). *A supercritical carbon dioxide cycle for next generation nuclear reactors.* (Sc D), Massachusetts Institute of Technology. Retrieved from http://hdl.handle.net/1721.1/17746

Dudley, V. E. (1994). *Test results: SEGS LS-2 solar collector*. Albuquerque, NM: Sandia National Laboratory.

Duffie, John A., & Beckman, William A. (2006). *Solar engineering of thermal processes* (3rd ed.). Hoboken, NJ: Wiley.

FLAGSOL. (2013). Dry Cooling. Retrieved 8/11/2013, 2013, from http://www.flagsol.com/flagsol/english/technology/research-development/dry-cooling/index.html

Forristall, R., & National Renewable Energy Laboratory. (2003). *Heat transfer analysis and modeling of a parabolic trough solar receiver implemented in Engineering Equation Solver Nrel/Tp 550-34169* (pp. 1 online resource (xvii, 145 p.)). Retrieved from http://purl.access.gpo.gov/GPO/LPS50881

Gaul, H., & Rabl, A. (1980). Incidence-Angle Modifier and Average Optical Efficiency of Parabolic Trough Collectors. *Journal of Solar Energy Engineering, 102*(1), 16-21. doi: 10.1115/1.3266115

Gupta, M. K., & Kaushik, S. C. (2010). Exergy analysis and investigation for various feed water heaters of direct steam generation solar–thermal power plant. *Renewable Energy, 35*(6), 1228-1235. doi: http://dx.doi.org/10.1016/j.renene.2009.09.007

Herrmann, Ulf, & Kearney, David W. (2002). Survey of Thermal Energy Storage for Parabolic Trough Power Plants. *Journal of Solar Energy Engineering, 124*(2), 145-152. doi: 10.1115/1.1467601

Iii, International Panel on Climate Change Working Group. (2012). *IPCC special report on renewable energy sources and climate change mitigation* Retrieved from http://myaccess.library.utoronto.ca/login?url=http://site.ebrary.com/lib/utoronto/Top?id=10516563

KACST, Natinal Renerable Energy Laboratory NREL and King Abdulaziz City for Science and Technology. (1999). NASA Remote Sensing Validation Data: Saudi Arabia. Retrieved 15 October 2013 http://rredc.nrel.gov/solar/new_data/Saudi_Arabia/

Kalogirou, Soteris. (2009). *Solar energy engineering processes and systems* (pp. 1 online resource (xv, 760 p.)). Retrieved from http://link.library.utoronto.ca/eir/EIRdetail.cfm?Resources__ID=897344&T=F

Klein, Sanford A. (2002). Engineering Equation Solver (EES) for Microsoft Widows Operating System; Academic Commercial version. Madison: F-Chart Software.

Kuravi, Sarada, Trahan, Jamie, Goswami, D. Yogi, Rahman, Muhammad M., & Stefanakos, Elias K. (2013). Thermal energy storage technologies and systems for concentrating solar power plants. *Progress in Energy and Combustion Science, 39*(4), 285-319. doi: http://dx.doi.org/10.1016/j.pecs.2013.02.001

Lakew, Amlaku Abie, Bolland, Olav, & Ladam, Yves. (2011). Theoretical thermodynamic analysis of Rankine power cycle with thermal driven pump. *Applied Energy, 88*(9), 3005-3011. doi: 10.1016/j.apenergy.2011.03.029

Munson, B. R. ; Young, D. F., Okiishi, T. H. . (1990). *Fundamentals of Fluid Mechanics*. New York, NY: John Wiley and Sons.

Niu, Xiao-Dong, Yamaguchi, Hiroshi, Iwamoto, Yuhiro, & Zhang, Xin-Rong. (2013). Optimal arrangement of the solar collectors of a supercritical CO2-based solar Rankine cycle system. *Applied Thermal Engineering, 50*(1), 505-510. doi: 10.1016/j.applthermaleng.2012.08.004

Niu, Xiao-Dong, Yamaguchi, Hiroshi, Zhang, Xin-Rong, Iwamoto, Yuhiro, & Hashitani, Naoki. (2011). Experimental study of heat transfer characteristics of supercritical CO2 fluid in collectors of solar Rankine cycle system. *Applied Thermal Engineering, 31*(6-7), 1279-1285. doi: 10.1016/j.applthermaleng.2010.12.034

NREL, National Renewable Energy Laboratory. (2010). Parabolic Trough Solar Field Technology. Retrieved Novemeber, 2, 2013, from http://www.nrel.gov/csp/troughnet/solar_field.html

Patnode, Angela M. (2006). *Simulation and performance evaluation of parabolic trough solar power plants*. (Thesis (M S)), University of Wisconsin--Madison, 2006.

Pérez-Pichel, G. D., Linares, J. I., Herranz, L. E., & Moratilla, B. Y. (2012). Thermal analysis of supercritical CO2 power cycles: Assessment of their suitability to the forthcoming sodium fast reactors. *Nuclear Engineering and Design, 250*, 23-34. doi: 10.1016/j.nucengdes.2012.05.011

Petela, R. (1964). Exergy of Heat Radiation. *Journal of Heat Transfer, 86*(2), 187-192. doi: 10.1115/1.3687092

Philibert, Cédric, International Energy Agency., & Organisation for Economic Co-operation and Development. (2011). *Solar energy perspectives*. Paris: OECD/IEA.

Quaschning, Volker. (2003). Solar thermal power plants. *Renewable Energy World*, 109-113. http://www.volker-quaschning.de/articles/fundamentals2/index.php

Reddy, V. Siva, Kaushik, S. C., & Tyagi, S. K. (2012). Exergetic analysis and performance evaluation of parabolic trough concentrating solar thermal power plant (PTCSTPP). *Energy, 39*(1), 258-273. doi: 10.1016/j.energy.2012.01.023

Roesle, Matthew, Coskun, Volkan, & Steinfeld, Aldo. (2011). Numerical Analysis of Heat Loss From a Parabolic Trough Absorber Tube With Active Vacuum System. *Journal of Solar Energy Engineering, 133*(3), 031015. doi: 10.1115/1.4004276

SAM. (2012). System Advisor Model Version 2012.5.11 (SAM 2012.5.11) National Renewable Energy Laboratory. Golden, CO. Retrieved from https://sam.nrel.gov/content/downloads

Sarkar, Jahar. (2009). Second law analysis of supercritical CO2 recompression Brayton cycle. *Energy, 34*(9), 1172-1178. doi: 10.1016/j.energy.2009.04.030

Seidel, William. (2011). *Model development and annual simulation of the Supercritical Carbon Dioxide Brayton cycle for concentrating solar power applications*. (Thesis (M S)), University of Wisconsin--Madison, 2011.

Stoffel, Thomas L., & National Renewable Energy Laboratory. (2010). *Concentrating solar power best practices handbook for the collection and use of solar resource data Nrel/Tp 550-47465* (pp. 1 online resource (xiv, 130 p.)). Retrieved from http://purl.fdlp.gov/GPO/gpo13107

Therminol®.). Therminol VP-1 Vapor, Phase/Liquid Phase, Heat Transfer Fluid. 2013, from http://www.therminol.com/pages/products/vp-1.asp

Wikipedia. (2013). Kramer Junction, California. 2013, from http://en.wikipedia.org/wiki/Kramer_Junction,_California

Zhang, X. R., Yamaguchi, H., Uneno, D., Fujima, K., Enomoto, M., & Sawada, N. (2006). Analysis of a novel solar energy-powered Rankine cycle for combined power and heat generation using supercritical carbon dioxide. *Renewable Energy, 31*(12), 1839-1854. doi: 10.1016/j.renene.2005.09.024

Zhang, Xin-Rong, Yamaguchi, Hiroshi, & Uneno, Daisuke. (2007). Experimental study on the performance of solar Rankine system using supercritical CO2. *Renewable Energy, 32*(15), 2617-2628. doi: 10.1016/j.renene.2007.01.003